

**Study on the effect of speciation on radionuclide mobilization –
C-14 speciation in irradiated Zircaloy-4 cladding and nitrate/
chloride interaction with An(III)/Ln(III)**

Zur Erlangung des akademischen Grades eines

DOKTORS DER NATURWISSENSCHAFTEN

(Dr. rer. nat.)

von der KIT-Fakultät für Chemie und Biowissenschaften
des Karlsruher Instituts für Technologie (KIT)

genehmigte

DISSERTATION

von

Dipl.-Chem. Michel Herm

aus

Heidelberg, Deutschland

KIT-Dekan:	Prof. Dr. W. Klopfer
Referent:	Prof. Dr. H. Geckeis
Korreferent:	Prof. Dr. P. Panak
Tag der mündlichen Prüfung:	18.12.2015

Statement of originality / Erklärung

Hiermit versichere ich, dass ich die vorliegende Arbeit selbstständig angefertigt und keine anderen als die angegebenen Quellen und Hilfsmittel benutzt habe. Darüber hinaus versichere ich, dass alle Stellen der Arbeit, die wörtlich oder inhaltlich aus anderen Quellen übernommen wurden als solche kenntlich gemacht sind und die Regeln zur Sicherung guter wissenschaftlicher Praxis am Karlsruher Institut für Technologie (KIT) in der jeweils gültigen Fassung beachtet wurden. Außerdem versichere ich, dass die Arbeit in gleicher oder ähnlicher Form noch keiner Prüfungsbehörde vorgelegt wurde.

Eggenstein-Leopoldshafen, 27.10.2015

.....

(place and date/Ort und Datum)

.....

(signature/Unterschrift)

Acknowledgements / Danksagung

Die vorliegende Arbeit wurde im Zeitraum von August 2012 bis Dezember 2015 unter der Leitung von Herrn Prof. Dr. Horst Geckeis am Karlsruher Institut für Technologie, Institut für Nukleare Entsorgung angefertigt. Ich danke Herrn Prof. Dr. Horst Geckeis für die interessante Themenstellung, wissenschaftliche Betreuung und fachlichen Diskussionen.

Ganz besonders möchte ich Dr. Marcus Altmaier, Dr. Xavier Gaona, Dr. Ernesto González-Robles und Dr. Volker Metz (alle KIT-INE) für die ausgezeichnete Betreuung und anregenden Diskussionen danken. Durch ihre Unterstützung, Hilfsbereitschaft und zahlreichen Ratschläge haben sie wesentlich zum Gelingen dieser Arbeit beigetragen.

Weiterhin danke ich Elke Bohnert für ihre Hilfsbereitschaft und Unterstützung bei Problemen jeder Art. Dr. David Fellhauer danke ich für seine Unterstützung bei den Pitzer Rechnungen. Bei Dr. Bernhard Kienzler bedanke ich mich für seine oft sehr hilfreichen Ratschläge. Des Weiteren danke ich Nikolaus Müller für seine Hilfsbereitschaft und Unterstützung bei der Einführung in den Umgang mit den Manipulatoren der abgeschirmten Boxenlinie. Dr. Thomas Rabung danke ich für seine Unterstützung bei den Laserfluoreszenzuntersuchungen (alle KIT-INE).

Ich danke Dr. Kathy Dardenne, Dr. Nicolas Finck und Dr. Jörg Rothe (alle KIT-INE) für ihre Unterstützung bei den EXAFS Untersuchungen.

Für ihre Hilfsbereitschaft bei chemischen Analysen danke ich außerdem Melanie Böttle, Markus Fuss, Frank Geyer, Tanja Kisely, Eva Soballa und Cornelia Walschburger (alle KIT-INE).

Ferner danke ich der INE-Werkstatt und dem INE-Infrastrukturteam für ihre Unterstützung bei dem Aufbau und der Inbetriebnahme des Handschuhkastens für die C-14 Abtrennung im Kontrollbereich des KIT-INE.

Des Weiteren möchte ich mich bei Dr. Maarten Becker und Dr. Ron Dagan (beide KIT-INE) für ihre Unterstützung bei den MCNP-X Rechnungen bedanken.

Ich danke außerdem Dr. David Bottomley, Ralf Gretter, Ramil Nasyrow, Dr. Dimitrios Papaioannou und Dr. Detlef Wegen (alle JRC-ITU) für fachliche Diskussionen und ihre Unterstützung bei Untersuchungen am Brennstabsegment N0204.

Zuletzt danke ich meinen Eltern die immer für mich da sind.

Abstract

This Ph.D. thesis addresses some examples for the speciation of actinides and activation products relevant in the context of nuclear waste disposal in the solid, aqueous and gas phases. The final aim of this work is providing scientifically sound and reliable inputs for the source term estimation in repositories for disposal of nuclear waste, and further to derive comprehensive thermodynamic models for the quantitative description of the investigated systems. In particular, the interaction of trivalent actinides and lanthanides with nitrate and chloride in dilute to concentrated saline systems has been studied in combination with the quantification of the inventory of C-14, Fe-55, Sb-125 and Cs-137 in Zircaloy-4 (Zry-4) of a spent UO₂ fuel rod segment. Besides determining the overall inventory, the focus of the latter topic in this Ph.D. work has been given to the assessment of the chemical form of C-14 released from the irradiated Zircaloy-4.

In the context of nuclear waste disposal in deep geological repositories, trivalent actinides and their behavior in dilute to concentrated aqueous solutions as well as the release of long-lived activation products are of particular importance in the long-term safety assessment of these facilities. Access of groundwater into the repository and a potential contact of the intruding water with the emplaced radioactive waste represent a possible migration pathway for radionuclides from the repository to the biosphere. Consequently, a detailed understanding of the processes driving the mobilization/retention of these radionuclides is indispensable. One of the main parameters affecting the transport/retardation mechanisms of these radionuclides is their speciation in the aqueous and gas phases, as well as secondary phase formation and solubility phenomena.

Investigations in concentrated saline systems are of special interest in view of disposal of nuclear waste in rock-salt and certain deep sedimentary formations where elevated ionic strengths are expected. Furthermore, the systematic use of

dilute to concentrated solutions importantly contributes in deriving accurate chemical and thermodynamic models, whilst simultaneously allowing the determination of activity models for the investigated system. Besides the potential contribution of the host-rock to the high salinity of solutions, elevated concentrations of salt/ligands may also arise from groundwater contact with certain waste forms. Hence, solutions with high concentrations of nitrate (≥ 1 M) are expected in repositories containing waste from nuclear fuel reprocessing. Very high nitrate concentrations in combination with hyperalkaline pH conditions prevail in several waste tanks of the Hanford Site (Washington, USA).

The effect of nitrate on the solubility of An(III)/Ln(III) is studied in dilute to concentrated NaCl–NaNO₃, MgCl₂–Mg(NO₃)₂ and CaCl₂–Ca(NO₃)₂ solutions at $2.91 \leq \text{pH}_m \leq 13.2$ and $T = 22 \pm 2^\circ\text{C}$. Batch solubility experiments are conducted with Nd(OH)₃(s) taken as a chemical homologue to trivalent actinide hydroxide, complemented with the use of advance spectroscopic techniques (Cm(III)–TRLFS, Nd–L_{III} EXAFS) and extensive solid phase characterization in what is the first targeted comprehensive investigation of this system. The combination of these techniques shows the impact of nitrate on the solubility of An(III)/Ln(III) due to the formation of the previously unreported aqueous species $\text{Mg}[\text{An}^{\text{III}}/\text{Ln}^{\text{III}}\text{NO}_3\text{OH}]^{3+}$ and $\text{Mg}[\text{An}^{\text{III}}/\text{Ln}^{\text{III}}\text{NO}_3(\text{OH})_2]^{2+}$. Thermodynamic and Pitzer activity models previously derived for An(III) and Ln(III) for chloride systems have been extended in this work to nitrate-bearing systems $\text{Nd}^{3+}/\text{Cm}^{3+}\text{--H}^+\text{--Na}^+\text{--Mg}^{2+}\text{--Ca}^{2+}\text{--OH}^-\text{--Cl}^-\text{--NO}_3^-\text{--H}_2\text{O}$.

In a second section of this Ph.D. thesis, the transformation of Nd(OH)₃(s) into a ternary Nd–OH–Cl(s) solid phase is experimentally assessed in concentrated NaCl, MgCl₂ and CaCl₂ systems as a function of pH, Cl[–] concentration and temperature ($T = 22$ and 80°C). Extensive batch solubility experiments are performed using Nd(OH)₂Cl(s) in NaCl, MgCl₂, CaCl₂ and $7.0 \leq \text{pH}_m \leq 13$, in combination with exhaustive solid phase characterization by XRD and SEM-EDS. The results

confirm the unexpected predominance of $\text{Nd}(\text{OH})_2\text{Cl}(\text{s})$ in concentrated MgCl_2 and CaCl_2 under repository-relevant pH conditions. This solid phase shows a remarkably lower solubility than $\text{Nd}(\text{OH})_3(\text{s})$, typically assumed to control the solubility of An(III)/Ln(III) in the absence of complexing ligands. The combination of the experimental results obtained in this work with the previously reported thermodynamic and Pitzer activity models for An(III)/Ln(III) aqueous species allows the quantification of $\lg^*K_{s,0}^{\circ}\{\text{Nd}(\text{OH})_2\text{Cl}(\text{s})\}$.

The comprehensive work undertaken within this Ph.D. thesis represents a very important step forward in the scientific understanding of An(III)/Ln(III) behavior in dilute to concentrated chloride- and nitrate-bearing systems, and provides a key input for the source term estimation of An(III) under repository-relevant conditions. The chemical, thermodynamic and Pitzer activity models derived for An(III)/Ln(III) in this work establish an optimized scientific tool for the quantitative description of the main processes affecting this relevant redox state under the investigated chemical boundary conditions.

The amount and chemical form of C-14 as well as the inventories of Fe-55, Sb-125 and Cs-137 are determined in irradiated Zircaloy-4 cladding. Experimentally measured radionuclide contents are compared to theoretically predicted inventory of the Zircaloy-4 obtained by means of Monte Carlo N-particle (MCNP-X) calculations. C-14 (pure β^- emitter) is a difficult radionuclide to measure. Therefore, a robust C-14 extraction and analysis system is developed applicable to highly radioactive samples. The method allows simultaneously the separation/quantification of C-14 from other radionuclides present in the activated material in gaseous and aqueous aliquots as well as the determination of the total inorganic and organic/CO C-14 bearing compounds present in the gas and aqueous phase. The work is performed within the FP7-EURATOM-FISSION collaborative project CAST (CArbon-14 Source Term, www.projectcast.eu).

Kurzfassung

Die vorliegende Doktorarbeit behandelt die chemische Speziation einiger endlagerrelevanter Actiniden und Aktivierungsprodukte in der wässrigen, Gas- und Festphase. Die Arbeiten zielen darauf ab, zu einer wissenschaftlich basierten zuverlässigen Einschätzung der Radionuklidchemie unter endlagerrelevanten Bedingungen zu kommen. Hierdurch werden belastbare Ableitungen von Radionuklidquelltermen für Endlager radioaktiver Abfälle und verbesserte Langzeitsicherheitsanalysen ermöglicht. Als zentrales Element der vorliegenden Arbeit werden umfassende chemische und thermodynamische Modelle zur quantitativen Beschreibung der untersuchten Systeme abgeleitet. Insbesondere die Wechselwirkung dreiwertiger Actiniden mit Nitrat und Chlorid in verdünnten bis konzentrierten Salzlösungen sowie das Inventar von C-14, Fe-55, Sb-125 und Cs-137 in Zircaloy-4 eines bestrahlten UO₂ Brennstabsegments wurden untersucht. Besonderer Wert wurde hierbei auf die Untersuchung der chemischen Speziation des in die wässrige und Gasphase freigesetzten C-14 gelegt.

Für die Bewertung der Langzeitsicherheit eines Endlagers für radioaktive Abfälle sind das Verhalten von dreiwertigen Actiniden, einer typischen Oxidationsstufe von verschiedenen Actiniden unter reduzierenden Bedingungen, in verdünnten bis konzentrierten wässrigen Lösungen sowie die Freisetzung langlebiger Aktivierungsprodukte von besonderem Interesse. Wasserzutritt in ein Endlager und der Kontakt der wässrigen Lösung mit den eingelagerten Abfällen stellen ein mögliches Freisetzungsszenario für Radionuklide aus dem Endlager in die Umgebung dar. Folglich ist ein grundlegendes wissenschaftliches Verständnis dieser Radionuklidmobilisierungs- und Rückhalte-mechanismen unverzichtbar. Transport und Rückhaltung von Radionukliden hängen vor allem von ihrer chemischen Form, der sogenannten Speziation, in der wässrigen und Gasphase sowie der Bildung von Sekundärphasen und Löslichkeitsprozessen ab.

Salinare Systeme sind von besonderem Interesse im Hinblick auf Endlagerung radioaktiver Abfälle in Steinsalz und bestimmten tiefen Sedimentformationen mit Porenwässern erhöhter Ionenstärke. Die Abfallmatrix bestimmter Abfälle enthält außerdem Bestandteile, die zusätzlich zu einer erhöhten Salz bzw. Ligandenkonzentration im Falle einer Auslaugung beitragen können. So sind z.B. erhöhte Nitratkonzentrationen (≥ 1 M) in Endlagern zu erwarten, die Abfälle aus der Wiederaufarbeitung enthalten. Auch in bestimmten Lagerbehältern für flüssige radioaktive Abfälle (sogenannte Untergrundtanks) der Hanford Site (Washington, USA) sind sehr hohe Nitratkonzentrationen und hyperalkalische pH Bedingungen vorhanden.

Der Einfluss von Nitrat auf die Löslichkeit von An(III)/Ln(III) wird im Rahmen dieser Arbeit in verdünnten bis konzentrierten NaCl–NaNO₃, MgCl₂–Mg(NO₃)₂ und CaCl₂–Ca(NO₃)₂ Lösungen im pH-Bereich $2.91 \leq \text{pH}_m \leq 13.2$ und $T = 22 \pm 2^\circ\text{C}$ systematisch untersucht. Umfassende Löslichkeitsexperimente mit Nd(OH)₃(s) werden ergänzt durch spektroskopische Methoden (Cm(III)–TRLFS, Nd–L_{III} EXAFS) und umfangreicher Festphasencharakterisierung. Hierdurch steht erstmalig eine umfassende experimentelle Beschreibung dieses relevanten Systems zur Verfügung. Die Kombination der angewendeten Methoden zeigt den eindeutigen Einfluss von Nitrat auf die Löslichkeit von An(III)/Ln(III) durch die Bildung von Mg[An^{III}/Ln^{III}NO₃OH]³⁺ und Mg[An^{III}/Ln^{III}NO₃(OH)₂]²⁺ Spezies. Die bestehende thermodynamische Datenbasis und das Pitzer Aktivitätsmodell für An(III)/Ln(III) wurden im Rahmen dieser Arbeit erstmalig auf hochsalinare nitrathaltige Systeme erweitert wodurch die Beschreibung des Systems Nd³⁺/Cm³⁺–H⁺–Na⁺–Mg²⁺–Ca²⁺–OH[–]–Cl[–]–NO₃[–]–H₂O ermöglicht wird.

Weiterhin wird in dieser Doktorarbeit die Umwandlung von Nd(OH)₃(s) in eine ternäre Nd–OH–Cl(s) Festphase erstmalig im Kontext der aquatischen Actinidenchemie und systematischen Löslichkeitsuntersuchungen behandelt. Die Umwandlung wird experimentell in konzentrierten NaCl, MgCl₂ und CaCl₂

Lösungen als Funktion des pH, der Cl^- Konzentration und der Temperatur untersucht ($T = 22$ und 80°C). Umfangreiche Löslichkeitsexperimente werden mit $\text{Nd}(\text{OH})_2\text{Cl}(\text{s})$ in NaCl , MgCl_2 und CaCl_2 bei $7.0 \leq \text{pH}_m \leq 13$ durchgeführt und durch umfassende Festphasencharakterisierung ergänzt. Die Ergebnisse zeigen das Vorhandensein von $\text{Nd}(\text{OH})_2\text{Cl}(\text{s})$ in konzentrierten MgCl_2 und CaCl_2 Lösungen unter endlagerrelevanten pH Bedingungen. Ferner zeigt $\text{Nd}(\text{OH})_2\text{Cl}(\text{s})$ eine signifikant verminderte Löslichkeit im Vergleich zu $\text{Nd}(\text{OH})_3(\text{s})$, welches bislang in Langzeitsicherheitsanalysen typischerweise als die löslichkeitskontrollierende Festphase für $\text{An}(\text{III})/\text{Ln}(\text{III})$ in Abwesenheit komplexierender Liganden angenommen wird. Die experimentell erhaltenen Ergebnisse erlauben die Bestimmung von $\lg^*K_{s,0}^{\circ}\{\text{Nd}(\text{OH})_2\text{Cl}(\text{s})\}$ unter Verwendung des bestehenden Thermodynamik und Pitzer Aktivitätsmodells für dreiwertige Actiniden/Lanthaniden.

Im zweiten Teil der Arbeit werden das Inventar und die chemische Form von C-14 sowie das Inventar von Fe-55, Sb-125 und Cs-137 in bestrahltem hochradioaktiven Zircaloy-4 Hüllrohrmaterial untersucht. Dabei werden experimentell gemessene Radionuklidinventare mit berechneten Radionuklidinventaren des Zircaloy-4 aus Aktivierungsrechnungen mittels Monte Carlo N-particle (MCNP-X) Modellierung verglichen. Da C-14 ein reiner β^- Strahler ist, muss es, um belastbare Zerfallsmessungen zu ermöglichen, aufwendig von anderen Radionukliden aus einem stark radioaktiven Gemisch abgetrennt werden. Hierzu wird eine robuste C-14 Extraktions- und Analysemethode entwickelt, welche insbesondere auch auf hochradioaktive Proben anwendbar ist. Ferner erlaubt die Methode die gleichzeitige Separation/Mengenbestimmung von C-14 von anderen Radionukliden in wässrigen und gasförmigen Teilproben sowie die getrennte Bestimmung des anorganischen gebundenen C-14 und des organisch inklusive des an CO gebundenen C-14 in der Flüssig- und Gasphase. Die Arbeiten stellen einen Beitrag zum FP7-EURATOM-

FISSION Verbundprojekt CAST (CARbon-14 Source Term, www.projectcast.eu)
dar.

Table of contents

1	Introduction	- 1 -
1.1	Background of the work	- 1 -
1.2	Aims of the present work	- 5 -
2	Actinide geochemistry	- 7 -
2.1	Aquatic chemistry of actinides	- 8 -
2.1.1	Oxidation states of actinides in aqueous solutions	- 8 -
2.2	Actinide solid phases and solubility phenomena	- 11 -
2.2.1	Solubility and hydrolysis of An(III)/Ln(III)	- 14 -
2.3	Actinide complexation reactions	- 16 -
2.4	Activity models and thermodynamic databases	- 17 -
2.4.1	SIT model	- 18 -
2.4.2	Pitzer model	- 20 -
2.4.3	Weak complexes within an ion-interaction approach.....	- 24 -
2.4.4	Thermodynamic databases.....	- 25 -
3	Carbon-14.....	- 27 -
3.1	C-14 production in Zircaloy-4 in light water nuclear power reactors -	27 -
3.2	C-14 in Zircaloy-4 in the context of deep geological nuclear waste repositories	- 32 -
4	Materials and Methods.....	- 33 -
4.1	Chemicals and radionuclides used in the present work.....	- 33 -
4.1.1	Chemicals	- 33 -
4.1.2	Cm(III) for TRLFS measurements	- 35 -
4.1.3	C-14 standard material for recovery tests	- 35 -
4.1.4	Other radionuclides used in this work	- 35 -
4.2	Materials synthesized for studies with Nd(III).....	- 36 -

4.2.1	Preparation of Nd(OH) ₃ (s) and magnesium oxychloride phases at room temperature.....	36 -
4.2.2	Preparation of Nd(OH) ₂ Cl(s) phases at $T = 22$ and 80°C	37 -
4.2.3	Preparation of neodymium batch solubility experiments.....	38 -
4.2.3.1	Preparation of batch solubility experiments in Na–Mg–Ca–Cl–NO ₃ solutions with Nd(OH) ₃ (s).....	39 -
4.2.3.2	Preparation of batch solubility experiments in concentrated NaCl, MgCl ₂ and CaCl ₂ solutions with Nd(OH) ₂ Cl(s)	40 -
4.3	Analysis methods applied to studies with Nd(III)	42 -
4.3.1	pH measurements	42 -
4.3.1.1	General definition of pH.....	42 -
4.3.1.2	pH measurements using glass electrodes.....	44 -
4.3.1.3	pH measurements in saline solutions.....	45 -
4.3.1.4	pH measurements and A-values determined in this work	46 -
4.3.2	Determination of total neodymium(III), concentration in solution using inductively coupled plasma mass spectrometry (ICP-MS).....	47 -
4.4	Zircaloy-4 sample origin and treatment.....	48 -
4.4.1	Origin and irradiation characteristics of the Zircaloy-4 cladding ..	48 -
4.4.2	Preparation of irradiated Zircaloy-4 plenum cladding specimens for the dissolution experiments.....	51 -
4.5	Analysis methods applied to studies with C-14 bearing samples	53 -
4.5.1	Liquid scintillation counting (LSC) for determining the carbon-14 and iron-55 concentration in solution	53 -
4.5.2	γ -spectroscopy for determining the antimony-125 and cesium-137 concentration in solution	56 -
4.5.3	Gas mass spectrometry (gas-MS).....	57 -
4.6	Dissolution of irradiated Zircaloy-4 specimen	58 -
4.6.1	Sample digestion in a glass reactor	59 -

4.6.2	Sample digestion in an autoclave	- 61 -
4.6.3	Carbon-14 extraction and separation technique	- 63 -
4.6.3.1	Experimental set-up for sample digestion and C-14 extraction in a glass reactor	- 63 -
4.6.3.2	Experimental set-up and C-14 extraction from aqueous and gaseous samples derived from dissolution experiments with Zircaloy-4 performed in an autoclave	- 67 -
4.7	Activation calculation and model for the prediction of the radionuclide inventory of the irradiated Zircaloy-4	- 70 -
4.8	Spectroscopic techniques and solid phase characterization	- 73 -
4.8.1	Cm(III)–TRLFS	- 73 -
4.8.1.1	Experimental set-up of the laser system used in this work ..	- 74 -
4.8.1.2	Data evaluation.....	- 75 -
4.8.1.3	Preparation of Cm(III) time-resolved laser fluorescence spectroscopy (TRLFS) samples	- 75 -
4.8.2	X-ray absorption spectroscopy (XAS).....	- 76 -
4.8.2.1	XAFS measurements.....	- 77 -
4.8.2.2	EXAFS data evaluation.....	- 77 -
4.8.2.3	Sample preparation for XAS	- 78 -
4.8.3	X-ray diffraction (XRD).....	- 78 -
4.8.4	Scanning electron microscopy – energy dispersive X-ray spectroscopy (SEM-EDS).....	- 79 -
5	Results and Discussion.....	- 81 -
5.1	Solubility and spectroscopic study of trivalent actinides and lanthanides in dilute to concentrated Na–Mg–Ca–Cl–NO ₃ mixtures.....	- 81 -
5.1.1	Solubility of Nd(OH) ₃ (s) in dilute to concentrated NaCl–NaNO ₃ , MgCl ₂ –Mg(NO ₃) ₂ and CaCl ₂ –Ca(NO ₃) ₂ mixtures	- 83 -

5.1.2 Solid phase characterization in NaCl–NaNO ₃ , MgCl ₂ –Mg(NO ₃) ₂ and CaCl ₂ –Ca(NO ₃) ₂ mixtures.....	- 89 -
5.1.3 Cm(III)–TRLFS studies in NaCl–NaNO ₃ , MgCl ₂ –Mg(NO ₃) ₂ and CaCl ₂ –Ca(NO ₃) ₂ mixtures.....	- 90 -
5.1.4 Nd–L _{III} EXAFS investigations in MgCl ₂ –Mg(NO ₃) ₂ mixtures.....	- 94 -
5.1.5 Chemical, thermodynamic and activity models	- 96 -
5.1.6 Conclusions regarding the effect of nitrate on the solubility of An ^{III} /Ln ^{III}	
- 101 -	
5.2 Mixed Nd(III)–OH–Cl(s) phases in concentrated NaCl, MgCl ₂ and CaCl ₂ brines: Formation, stability and solubility	- 102 -
5.2.1 Formation and stability of Nd–OH–Cl(s) phases in NaCl, MgCl ₂ and CaCl ₂ solutions.....	- 103 -
5.2.2 Solubility of Nd(OH) ₂ Cl(s) in concentrated NaCl, MgCl ₂ and CaCl ₂ solutions	- 106 -
5.2.3 “Mixing” experiments in NaCl, MgCl ₂ and CaCl ₂ solutions.....	- 110 -
5.2.4 Solid phase characterization in NaCl, MgCl ₂ and CaCl ₂	- 112 -
5.2.4.1 Solid phases recovered from solubility experiments with Nd(OH) ₂ Cl(s).....	- 112 -
5.2.4.2 Solid phases recovered from “mixing” experiments with Nd(OH) ₃ (s) and Nd(OH) ₂ Cl(s)	- 115 -
5.2.5 Chemical and thermodynamic models	- 117 -
5.2.5.1 Determination of $\lg^*K_{s,0}^{\circ}\{\text{Nd(OH)}_2\text{Cl(s)}\}$ from solubility experiments.....	- 117 -
5.2.5.2 Inputs from “mixing” experiments	- 119 -
5.2.5.3 Understanding the transformation of Nd(OH) ₃ (s) into Nd(OH) ₂ Cl(s).....	- 120 -
5.2.6 Conclusions regarding mixed Nd–OH–Cl(s) phases	- 122 -

5.3	Determination of C-14 and other activation/fission products in Zircaloy-4 cladding from an irradiated UO ₂ fuel rod segment	- 123 -
5.3.1	Chemical yield of the separation technique.....	- 124 -
5.3.2	Optical examination of the Zircaloy-4 and precipitations on the inner cladding surface	- 126 -
5.3.3	Improvement of the digestion experiments	- 127 -
5.3.4	Improvement of the separation technique.....	- 129 -
5.3.5	Results of experimental inventory analysis of irradiated Zircaloy-4 and chemical form of C-14 released from the studied cladding.....	- 130 -
5.3.6	Conclusions regarding the inventory and chemical form of C-14 in Zircaloy-4	- 135 -
6	Summary and Conclusions.....	- 139 -
	Appendix	- 143 -
	References	- 153 -

List of figures

Figure 2.1: Oxidation states of actinides in aqueous solution.	- 10 -
Figure 4.1: Images of the autoclave and PTFE liner used for the hydrothermal preparation of $\text{Nd}(\text{OH})_2\text{Cl}(\text{s})$ at 80°C	- 38 -
Figure 4.2: A_m values experimentally determined for different NaCl – NaNO_3 , MgCl_2 – $\text{Mg}(\text{NO}_3)_2$ and CaCl_2 – $\text{Ca}(\text{NO}_3)_2$ mixtures as a function of the nitrate concentration.	- 47 -
Figure 4.3: Pictures and dimension of the irradiated plenum Zircaloy-4.	- 50 -
Figure 4.4: Images of the preparation of Zircaloy-4 subsamples.	- 52 -
Figure 4.5: Quench correction curve for C-14 sample geometry and the energy window used for data evaluation.	- 55 -
Figure 4.6: Pictures of GAM400 quadrupole gas-MS and the batch inlet system for connecting the gas collecting cylinder to the instrument.	- 58 -
Figure 4.7: Images of the C-14 extraction and analysis system and the glass reactor.	- 60 -
Figure 4.8: Images of the autoclave and gas collecting cylinder.	- 62 -
Figure 4.9: Experimental design for C-14 extraction from Zircaloy-4 digestion experiments in glass reactor or digestion liquor obtained from autoclave experiments.	- 65 -
Figure 4.10: Customized washing bottle and customized dropping funnel. ...	- 65 -
Figure 4.11: Scheme of C-14 extraction procedure for C-14 bearing compounds released during digestion experiments with Zircaloy-4 specimens in a glass reactor.	- 67 -
Figure 4.12: Experimental design for C-14 extraction of gaseous aliquots obtained from dissolution experiments with Zircaloy-4 specimens in an autoclave.	- 68 -
Figure 4.13: Double-ended gas collecting cylinder for gaseous samples derived from digestion experiments with Zircaloy-4 performed in an autoclave.	- 68 -

Figure 4.14: Scheme of C-14 extraction procedure from gaseous and aqueous samples derived from dissolution experiments with Zircaloy-4 specimens using an autoclave.	- 70 -
Figure 4.15: Model and dimensions of the Zircaloy-4 plenum including stainless steel spring used for calculation.	- 72 -
Figure 4.16: Simple term scheme of Cm(III) and its spectroscopic characteristics.	- 74 -
Figure 4.17: Zircaloy-4 oxide layer and ZrO ₂ fragment prepared for SEM-EDS.	- 80 -
Figure 5.1: Solubility of Nd(OH) ₃ (s) in 0.1–6.02 m NaCl–NaNO ₃ solutions.	- 84 -
Figure 5.2: Solubility of Nd(OH) ₃ (s) in 2.80 m MgCl ₂ –Mg(NO ₃) ₂ with 1.13 m, 2.29 m and 5.82 m NO ₃ ⁻ in comparison with 4.05 m MgCl ₂ –Mg(NO ₃) ₂ with 1.16 m, 2.33 m and 5.82 m NO ₃ ⁻ . The solubility data of Nd(OH) ₃ (s) in 4.02 m CaCl ₂ –Ca(NO ₃) ₂ with 5.75 m NO ₃ ⁻ are also included in the figure.	- 87 -
Figure 5.3: Solubility of Nd(OH) ₃ (s) in 4.05 m MgCl ₂ –Mg(NO ₃) ₂ solution at pH _m = 8.80 with increasing nitrate concentration.	- 88 -
Figure 5.4: XRD patterns of Nd(III) solid phases recovered from batch solubility experiments in MgCl ₂ –Mg(NO ₃) ₂ systems.	- 90 -
Figure 5.5: Selection of experimental Cm(III)–TRLFS spectra over the entire investigated pH range in 5.61 m NaCl, 6.02 m NaNO ₃ , 4.05 m MgCl ₂ , 4.05 m MgCl ₂ –Mg(NO ₃) ₂ mixture with <i>m</i> _{NO₃⁻} = 5.81 m and 4.02 m CaCl ₂ –Ca(NO ₃) ₂ mixture with <i>m</i> _{NO₃⁻} = 5.75 m.	- 93 -
Figure 5.6: Experimental and fitted <i>k</i> ² -weighted Nd–L _{III} Fourier transform EXAFS spectrum of neodymium in 4.05 m MgCl ₂ –Mg(NO ₃) ₂ solution with 5.81 m NO ₃ ⁻ . -	95 -
Figure 5.7: XRD patterns of Nd(OH) ₃ (s) starting material and solid phases recovered from experiments in 5.15 m MgCl ₂ at <i>T</i> = 22°C, <i>T</i> = 80°C as well as solid	

phases recovered from experiments in 3.91 m CaCl₂ and 5.61 m NaCl at $T = 80^{\circ}\text{C}$, respectively..... - 105 -

Figure 5.8: Experimentally determined solubility of Nd(III) in 5.61 m NaCl using Nd(OH)₂Cl(s) as starting material. - 108 -

Figure 5.9: Experimentally determined solubility of Nd(III) in 2.67/2.68 m MgCl₂/CaCl₂, 3.87/3.91 m MgCl₂/CaCl₂ and 5.15 m MgCl₂ using Nd(OH)₂Cl(s) as starting material. - 109 -

Figure 5.10: XRD patterns of Nd(III) solid phases recovered from batch solubility experiments after > 225 days in comparison with the initial Nd(OH)₂Cl(s) material synthesized at $T = 22^{\circ}\text{C}$ - 114 -

Figure 5.11: SEM images of solid phases recovered from batch solubility experiments using Nd(OH)₂Cl(s) as starting material in 5.61 m NaCl at $\text{pH}_m = 10$ and in 5.15 m MgCl₂ at $\text{pH}_m = 8.5$ - 115 -

Figure 5.12: XRD patterns of Nd(III) solid phases recovered from “mixing” experiments performed with Nd(OH)₃(s) and Nd(OH)₂Cl(s). - 116 -

Figure 5.13: Solubility of Nd(OH)₂Cl(s) and Nd(OH)₃(s) in 2.67/2.68 m MgCl₂/CaCl₂ and 3.87/3.91 m MgCl₂/CaCl₂ as calculated with the Pitzer models reported for Nd(OH)₃(s) and Nd(OH)₂Cl(s) in [NECK *et al.*, 2009] and in the present work, respectively. - 121 -

Figure 5.14: Black/blueish precipitates seen on the inner surface of the irradiated Zircaloy-4 cladding. - 127 -

Figure 5.15: Exemplary SEM image and chemical analysis of the irradiated ZrO₂. - 128 -

Figure 5.16: LSC spectra obtained from alkaline washing bottle #7 of the C-14 extraction and analysis system. - 130 -

Figure A.1: Solubility of Nd(OH)₃(s) in 2.80 m MgCl₂–Mg(NO₃)₂ with 0.22 m and 0.56 m NO₃⁻ in comparison with 4.05 m MgCl₂–Mg(NO₃)₂ with 0.24 m and 0.58 m

NO_3^- . Together with solubility of $\text{Nd}(\text{OH})_3(\text{s})$ in 0.25 m $\text{MgCl}_2\text{-Mg}(\text{NO}_3)_2$ with 0.2 m NO_3^- and 1.04 m $\text{MgCl}_2\text{-Mg}(\text{NO}_3)_2$ with 2.14 m NO_3^- - 148 -

Figure B.1: Cm(III)–TRLFS spectra over the entire investigated pH range obtained in 4.05 m $\text{MgCl}_2\text{-Mg}(\text{NO}_3)_2$ mixture with $m_{\text{NO}_3^-} = 0.58$ m, 4.05 m $\text{MgCl}_2\text{-Mg}(\text{NO}_3)_2$ mixture with $m_{\text{NO}_3^-} = 2.33$ m, 4.05 m $\text{Mg}(\text{NO}_3)_2$ with $m_{\text{NO}_3^-} = 8.04$ m and 0.25 m $\text{MgCl}_2\text{-Mg}(\text{NO}_3)_2$ mixture with $m_{\text{NO}_3^-} = 0.20$ m. - 149 -

Figure C.1: Correlation of SIT ion interaction parameters reported for +1 to +4 monomeric cations with chloride and nitrate. - 150 -

List of tables

Table 4.1: Chemicals used in the present work.	- 34 -
Table 4.2: Summary of the matrix solutions used in the Nd(OH) ₃ (s) batch solubility experiments.....	- 41 -
Table 4.3: Summary of the matrix solutions and investigated pH _m in the Nd(III) batch solubility experiments with Nd(OH) ₂ Cl(s).	- 42 -
Table 4.4: Equations empirically determined in this work for the calculation of A _m values in NaCl–NaNO ₃ , MgCl ₂ –Mg(NO ₃) ₂ and CaCl ₂ –Ca(NO ₃) ₂ mixtures.	- 46 -
-	
Table 4.5: Characteristics and irradiation data of the UO ₂ fuel rod segment. .	- 49 -
Table 4.6: Mass and dose rate of the irradiated Zircaloy-4 specimens.	- 52 -
Table 4.7: Sample preparation for LSC measurements.	- 55 -
Table 4.8: Nominal composition of Zircaloy-4 and values used for calculation.	- 72 -
Table 4.9: Summary of the samples prepared for the Cm(III)–TRLFS measurements.	- 76 -
Table 5.1: Structural parameters obtained from EXAFS data evaluation.	- 95 -
Table 5.2: Equilibrium constants (<i>I</i> = 0, 25°C) for the solid hydroxides and aqueous complexes of Am(III)/Cm(III) and Nd(III).	- 99 -
Table 5.3: Ion interaction (Pitzer) coefficients for M(III) species (M = Am, Cm, Pu and Nd) in chloride/nitrate media at 25°C.....	- 100 -
Table 5.4: Summary of the transformation experiments conducted in NaCl, MgCl ₂ and CaCl ₂ systems at <i>T</i> = 22 and 80°C.....	- 106 -
Table 5.5: Experimentally determined pH _{m,mix} values in the “mixing” experiments.	- 111 -
Table 5.6: Results of recovery tests performed with C-14 labelled compounds.	- 126 -

Table 5.7: Results from LSC and γ -measurements obtained from the six Zircaloy-4 specimens.	132 -
Table 5.8: Mean values of the experimentally determined inventories of C-14, Fe-55, Cs-137 and Sb-125 in comparison with results from the activation calculations performed in this study and experimentally measured C-14 contents in a spent PWR Zircaloy-4 specimen with a similar burn-up.	133 -
Table 5.9: Partitioning of C-14 between total inorganic/organic fractions for each of the six samples.	134 -
Table 5.10: Distribution of inorganic and organic C-14 bearing compounds in the gaseous and aqueous phase obtained from dissolution experiments performed in an autoclave.	134 -
Table A.1: Experimental solubility data of $\text{Nd}(\text{OH})_3(\text{s})$ in NaCl – NaNO_3 mixtures.	143 -
Table A.2: Experimental solubility data of $\text{Nd}(\text{OH})_3(\text{s})$ in MgCl_2 – $\text{Mg}(\text{NO}_3)_2$ mixtures.	145 -
Table A.3: Experimental solubility data of $\text{Nd}(\text{OH})_3(\text{s})$ in CaCl_2 – $\text{Ca}(\text{NO}_3)_2$ mixtures.	147 -
Table D.1: Experimental solubility data of $\text{Nd}(\text{OH})_2\text{Cl}(\text{s})$ in NaCl solutions.	151 -
Table D.2: Experimental solubility data of $\text{Nd}(\text{OH})_2\text{Cl}(\text{s})$ in MgCl_2 solutions.	151 -
Table D.3: Experimental solubility data of $\text{Nd}(\text{OH})_2\text{Cl}(\text{s})$ in CaCl_2 solutions.	152 -
Table D.4: Experimental solubility data of “mixing” experiments performed with $\text{Nd}(\text{OH})_3(\text{s})$ and $\text{Nd}(\text{OH})_2\text{Cl}(\text{s})$ in various background electrolytes.	152 -

List of abbreviations

(am)	amorphous solid
(aq)	undissociated, uncharged aqueous species
(cr)	crystalline solid
(g)	gaseous
(hyd)	hydrated solid
(s)	solid
A.R.	analytical reagent
ACS	American Chemical Society
AMP	ammonium molybdophosphate
An	actinides
ANKA	Angströmquelle Karlsruhe
BWR	boiling water reactor
CHES	2-(Cyclohexylamino)ethane-sulfonic acid
cpm	counts per minute
DX	duplex
EDS	energy dispersive X-ray spectroscopy
EDTA	ethylenediaminetetraacetic acid
ELS	extra low Sn
EXAFS	extended X-ray absorption fine structure spectroscopy
GE	glass electrode
HDPE	high-density polyethylene
HEPES	2-[4-(2-Hydroxyethyl)-1-piperazine]ethanesulfonic acid
ICCD	intensified charge-coupled device
ICP-MS	inductively coupled plasma mass spectrometry
ID	inner diameter
INE	Institute for Nuclear Waste Disposal

ISA	isosaccharinic acid
ITU	Institute for Transuranium Elements
IUPAC	International Union of Pure and Applied Chemistry
JCPDS	Joint Committee on Powder Diffraction Standards
JRC	Joint Research Centre
kD	kilo Dalton
KIT	Karlsruhe Institute of Technology
KKG	Kernkraftwerk Gösgen
KPS	potassium peroxydisulfate
KWU	Kraftwerk Union AG
LDPE	low-density polyethylene
Ln	lanthanides
LSC	liquid scintillation counting
MCNP	Monte Carlo N-Particle
MOX	mixed oxide fuel
NEA	Nuclear Energy Agency
OD	outer diameter
OECD	Organization for Economic Co-operation and Development
PP	polypropylene
PTFE	polytetrafluoroethylene
PWR	pressurized water reactor
REF	reference electrode
RN	radionuclides
SEM	scanning electron microscope
SIT	specific ion interaction theory
SNF	spent nuclear fuel
SQP(E)	spectral quench parameter of the external standard
TDB	thermodynamic database

THEREDA	Thermodynamic Reference Database
TRIS	tris(hydroxymethyl)aminomethane
TRIS·HCl	tris(hydroxymethyl)aminomethane hydrochloride
TRLFS	time-resolved laser fluorescence spectroscopy
WIPP	Waste Isolation Pilot Plant
XAFS	X-ray absorption fine structure
XANES	X-ray absorption near edge structure spectroscopy
XAS	X-ray absorption spectroscopy
XRD	X-ray diffraction
Zry-2	Zircaloy-2
Zry-4	Zircaloy-4

List of symbols

Θ	angle of incidence
λ	wavelength
γ_i	activity coefficient of species i
a_i	chemical activity of species i
c_i	molar concentration of species i
E_j	liquid junction potential
F	Faraday constant
I	ionic strength
m_i	molal concentration of species i
R	universal gas constant
T	temperature
p	pressure

1 Introduction

1.1 Background of the work

Nuclear power generation, production/dismantling of nuclear weapons as well as the use of radioactive materials in medicine, research and industry have produced large amounts of radioactive waste since the second half of the 20th century. Depending on the source, this waste can comprise actinides (e.g. U, Np, Pu, Am), fission products (e.g. Tc-99, I-129, Cs-135) and/or activation products (e.g. C-14, Cl-36, Co-60) as well as inactive waste components (e.g. metals, cellulose, cleaning agents, nitrate, etc.). Due to the long half-life and high radiotoxicity of some of these radionuclides, a reliable and safe approach for the management of these radioactive wastes is indispensable.

Deep geological repositories (300–1000m below ground level) are internationally considered as the safest and most effective option for the final disposal of radioactive waste and its isolation from the biosphere. A multi-barrier concept is usually considered in the design of these repositories to prevent the mobilization of radionuclides. Generally this multi-barrier system includes the waste form itself, iron/steel canister (canister with a Cu-liner considered also in some disposal concepts), buffer/backfill material (e.g. bentonite), and ultimately the host rock itself. The latter is known as geological barrier, whereas the rest are considered as

geo-technical or technical barriers. Three main geological formations are internationally considered for the construction of those repositories, e.g. crystalline rock, clay rock and rock salt.

Final disposal in crystalline rock (granite, granodiorite or metamorphic bedrocks) has been decided in Finland and Sweden, and is currently under consideration in Argentina, Canada, China, Czech Republic, Germany, India, Japan, Russia, South Korea and Spain e.g. [METZ *et al.*, 2012]. Crystalline formations are mechanically stable and show a low mineral solubility as well as a high heat resistance. However, crystalline rock formations are fractured to some extent, and therefore provide natural migration pathways for the access of groundwater and release of contaminated solutions and gases into the biosphere.

Final disposal of radioactive waste in plastic clay rocks is under investigation in Belgium, whereas indurated clay rocks are being investigated in France and Switzerland and are considered in Argentina, Germany and Spain. Clay/clay rock shows a very high sorption capacity and very low solubility and permeability. However, due to the high plasticity and very low excavation stability, advanced engineering efforts are needed for mining in clay rock. Furthermore the heat resistance and heat conductivity of clay rock is low.

The final disposal in rock salt is considered and/or already in operation in Germany (Morsleben) and USA (Waste Isolation Pilot Plant, WIPP, New Mexico). Rock salt exhibits many advantages such as high heat resistance and heat conductivity as well as impermeability. It further shows favorable properties such as self-sealing (convergence) due to its very high plasticity. Providing a complete sealing of the shaft, a repository in rock salt is expected to be dry, mainly because of the very limited brine reservoirs and the lack of connections to groundwater outside the salt complex. However, due to the very high solubility of salt, the consideration of water intrusion scenarios is especially important in the safety assessment of this type of

repositories. One of the main limitations of this disposal concept is the very low retention of radionuclides due to the limited sorption capacity of salt.

In the long-term safety assessment of deep geological repositories for nuclear waste disposal, a sound understanding of migration pathways of radionuclides from the repository to the biosphere is required. A relevant scenario accounted for is the access of formation water in the repository and consequent contact of the intruding water with the emplaced radioactive waste.

The geochemical milieu of a deep geological repository for nuclear waste is very complex. At a depth of several hundreds of meters, relevant argillaceous and granitic type formation waters are usually Na^+/Cl^- type solutions, characterized by anaerobic conditions and a pH in the range of 7 to almost 9 [METZ *et al.*, 2012]. Sedimentary and crystalline rock type formation waters are normally characterized by low ionic strength, although formation waters with elevated ionic strength are also found in sedimentary bedrocks in the Canadian Shield [FRAPE AND FRITZ, 1984] and Cretaceous argillites in Northern Germany [BREWITZ, 1980], among other examples. Fluid inclusions and brine pockets in rock salt formations are characterized by high ionic strength ($I_m > 5 \text{ m}$) dominated by high concentrations of mainly Na^+ , Mg^{2+} , K^+ and Cl^- .

The use of cement is also foreseen for the stabilization of certain waste types and construction purposes. Cement and cementitious materials buffer the porewater pH in the alkaline to hyperalkaline range, whilst retaining relatively high Ca concentrations ($\approx 0.02 \text{ M}$ at $\text{pH} = 12.5$). Corrosion of cementitious waste forms in MgCl_2 dominated brines may lead to high CaCl_2 concentrations ($\geq 2 \text{ M}$) and highly alkaline pH_m (≈ 12) conditions [BUBE *et al.*, 2013]. The interaction of actinides with salt brines leads to unique geochemical boundary conditions affecting significantly actinide solubility and speciation [ALTMAIER *et al.*, 2013].

Strongly reducing conditions will develop after the closure of deep geological repositories due to the corrosion of iron/steel containers and structural components,

Introduction

producing dissolved Fe(II) species, Fe(II)/Fe(III) solid phases and hydrogen. In these reducing geochemical conditions, actinides are expected to prevail in tri- and tetravalent redox states under near-neutral to alkaline pH-conditions: U(IV), Np(IV), Pu(III/IV), Am(III), among others.

The anoxic corrosion of the container/waste matrix may result in the release of radionuclides into the aqueous and/or gaseous phase. The further transport/retention of the released radionuclides strongly depends on the aqueous/gaseous speciation. Gaseous species (e.g. some forms of C-14) and anionic aqueous species (e.g. Se^{2-} , Γ) are normally considered highly mobile due to the usually very limited retention via sorption processes. Although An(III) and An(IV) are generally prone to stronger sorption and lower solubility, their mobility is also strongly dependent on their aqueous speciation. The complexation of actinides with strong ligands (e.g. carbonate, ethylenediaminetetraacetic acid (EDTA), isosaccharinic acid (ISA)) or weaker ligands present in high concentrations (e.g. nitrate, chloride) can importantly alter their mobilization/retention properties and thus requires attention. High concentrations of nitrate ($\geq 1 \text{ M}$) are expected in wastes from nuclear fuel reprocessing, although other sources/processes can be also responsible for elevated nitrate concentration/inventory in repositories for waste disposal [PAIVA AND MALIK, 2004; CRAWFORD *et al.*, 2006]. In the WIPP, a deep underground salt mine for transuranic waste disposal, the initial quantity of nitrate in waste is calculated to be $2.74 \times 10^7 \text{ mol}$ [KICKER AND HERRICK, 2013]. Very high nitrate concentrations in combination with hyperalkaline pH conditions also exists in several waste tanks of the Hanford Site (Washington, USA) [PHILIP HILL, 2011]. Slow nitrate reduction kinetics expected at 25°C and moderate H_2 partial pressure [TRUCHE *et al.*, 2013] may affect the aqueous speciation of radionuclides and thus impact their mobilization into the biosphere.

1.2 Aims of the present work

The main goal of the present Ph.D. thesis is the study of the speciation of actinides and activation products relevant in the context of nuclear waste disposal. This involves a thorough understanding of the interaction of trivalent actinides/lanthanides with nitrate and chloride in dilute to concentrated saline systems, with the aim of deriving comprehensive thermodynamic models and providing robust inputs for source term estimations. Furthermore, the present work aims at an accurate determination of the inventory of various radionuclides present in irradiated Zircaloy-4, with further focus on the chemical form of C-14 released from the Zr-alloy. The three main objectives of this work can be summarized as:

- The complexation of Nd(III) and Cm(III) considered as chemical analogues for Pu(III) and Am(III) with nitrate is studied in dilute to concentrated NaCl–NaNO₃, MgCl₂–Mg(NO₃)₂ and CaCl₂–Ca(NO₃)₂ mixtures with varying pH and nitrate concentrations. Comprehensive solubility studies are performed with Nd(III) and complemented by extensive spectroscopic studies (Cm(III)–TRLFS, Nd–L_{III} EXAFS) giving insight on the aqueous speciation of An(III)/Ln(III) in presence of nitrate. Further comprehensive thermodynamic and activity models are derived for the system Nd³⁺/Cm³⁺–H⁺–Mg²⁺–OH[–]–Cl[–]–NO₃[–]–H₂O at 25°C. This part of the present Ph.D. thesis was published in the IUPAC journal *Pure and Applied Chemistry* [HERM *et al.*, 2015].
- The formation and stability of Nd(III)–OH–Cl(s) phases is investigated as a function of pH and temperature in dilute to concentrated NaCl, MgCl₂ and CaCl₂ solutions. The solubility of the solid phase Nd(OH)₂Cl(s) synthesized in this work is studied in concentrated salt systems in combination with a comprehensive solid phase characterization using XRD and SEM-EDS. The

final goal is the determination of the chemical and thermodynamic models of these systems, with focus on the transformation of $\text{An}^{\text{III}}/\text{Ln}^{\text{III}}(\text{OH})_3(\text{s})$ into $\text{An}^{\text{III}}/\text{Ln}^{\text{III}}(\text{OH})_2\text{Cl}(\text{s})$ and the possible implications of this process on the retention of An(III) in the context of nuclear waste disposal.

- The inventory of C-14, Fe-55, Sb-125 and Cs-137 in Zircaloy-4 cladding of a spent UO_2 fuel rod segment is determined by a series of digestion experiments, and compared with theoretically predicted inventories. Special focus is also given to the chemical form of C-14 released from Zircaloy-4 in gaseous and aqueous samples. The speciation of the long-lived activation product C-14 is crucial for its mobilization/retention after release. For this purpose, a C-14 extraction and analysis method is developed, applicable to highly radioactive samples. This method allows simultaneously to determine the inventory of C-14 and the chemical form (dissolved/gaseous inorganic/organic compounds) released from the studied material.

2 Actinide geochemistry

Chemical elements following actinium in the periodic table of elements are denoted as actinides and are characterized by the successive occupation of the 5f orbitals (thorium ($Z = 90$) to lawrencium ($Z = 103$)). Actinides are radioactive and have no stable isotopes. In nature, only thorium and uranium occur in significant amounts. Protactinium occurs naturally only in trace amounts in uranium ores due to radioactive decay of U-238 and U-235. All actinide elements following uranium are denoted as transuranium elements, do not occur naturally and are only produced by nuclear reactions.

The most abundant actinide is thorium with about 8.1 ppm in the Earth's crust. The principal source of Th is monazite ((Ce, La, Nd, Th)[PO₄]) [KALTSOYANNIS AND SCOTT, 1999]. The heaviest naturally occurring actinide, uranium, has an abundance of about 2.4 ppm in the Earth's crust and is found in oxide minerals such as pitchblende (uraninite, UO₂) or carnotite (K₂(UO₂)₂(VO₄)₂·3H₂O) [KALTSOYANNIS AND SCOTT, 1999].

The transuranium elements neptunium to fermium are formed by neutron capture reactions (quickly) followed by the emission of a β^- particle. Very high neutron flux densities are necessary to produce transuranium elements up to fermium. Such high neutron flux densities are found e.g. in high flux reactors or thermonuclear explosions. For actinides beyond Fm-257, neutron capture cannot be used anymore since the next isotope (Fm-258) undergoes spontaneous fission. Therefore the bombardment of an actinide target (e.g. Es-253, Am-243 or mixed isotopes of Cf)

by very light nuclei (e.g. He-4, N-15, B-10, O-18) must be used [KALTSOYANNIS AND SCOTT, 1999].

2.1 Aquatic chemistry of actinides

Actinides are toxic and radiotoxic metals of special interest in the context of nuclear waste disposal. Particularly, the prediction and understanding of their fate in environmental systems is indispensable, even at trace concentration levels. In respect of safety analysis of deep geological nuclear waste repositories, the intrusion of aqueous solutions has to be taken into account in several scenarios of the long-term evolution of these facilities. In this framework, a sound understanding of the aquatic chemistry of actinides is necessary as a potentially relevant pathway for their migration/mobilization into the biosphere.

The aquatic chemistry of actinides is primarily characterized by redox processes, solubility/sorption phenomena and complexation reactions. In addition to these fundamental processes, the description of the chemistry of actinides in solution requires also the assessment of other factors such as ionic strength, temperature, kinetics or microbial activity.

2.1.1 Oxidation states of actinides in aqueous solutions

In contrast to lanthanides [DURRANT AND DURRANT, 1970; KATZ *et al.*, 1986], actinides exhibit a much greater range of oxidation states in solution, especially for

the early actinides (see Figure 2.1). The later actinides favor the trivalent oxidation state like the lanthanides [KIM, 1986, 1993], except nobelium which is preferably found in its divalent oxidation state.

The greater range of oxidation states shown by the early actinides in comparison with the lanthanides is due to the poor shielding of the 5f orbitals by the filled 6s and 6p shells, in contrast to the more efficient shielding of the 4f orbitals provided by the 5s and 5p shells in case of the lanthanides [COTTON, 2006]. Consequently, the 5f orbitals show a greater extension than the 4f orbitals, and their less tightly bound electrons are readily available for bonding [KALTSOYANNIS AND SCOTT, 1999; COTTON, 2006]. Furthermore, the energy gap between the $5f^n 7s^2$ and $5f^{n-1} 6d 7s^2$ configurations is smaller than for the corresponding lanthanides [COTTON, 2006]. As a result of the near-degeneracy of the 5f, 6d and 7s electrons, even more outer-shell electrons can be involved in the complex formation and a wider range of oxidation states is observed [COTTON, 2006].

However, with increasing atomic number Z and the associated contraction of the 5f orbitals, the energies of the latter drop rapidly and the energy gap between the 5f, 6d and 7s shells increases. For this reason, the chemistry of the later actinides resembles that of the lanthanides [KALTSOYANNIS AND SCOTT, 1999; COTTON, 2006].

Note that the lanthanide and actinide contraction (reduction of metal and An^{3+}/Ln^{3+} radii with increasing Z) arises from the poor ability of f electrons to screen the other valence electrons from the nuclear charge [KALTSOYANNIS AND SCOTT, 1999].

Among An(III), the use of Cm(III) is often favored instead of Am(III) or Pu(III) due to its advantageous spectroscopic properties, which allow to study its aqueous speciation at trace concentration levels ($\leq 10^{-8}$ M) using time-resolved laser fluorescence spectroscopy. Although with more complex electronic transitions than Cm(III), Eu(III) is one of the lanthanides with most favorable spectroscopic properties and is very often used in TRLFS studies. The concept of analogy is widely accepted for estimating activity coefficients and complex formation constants for aqueous species of actinides and lanthanides with the same redox state. However the analogy concept is not suitable for deriving thermodynamic data of solid phases, as small changes in the ionic radius can lead to remarkable changes in the stability of a solid and its solubility product [NECK *et al.*, 1998].

2.2 Actinide solid phases and solubility phenomena

The aqueous chemistry of actinides in the absence of other complexing ligands is dominated by hydrolysis and the formation/precipitation of actinide oxy-hydroxides. The solubility of actinides is defined by the thermodynamic stability of the solubility controlling solid phases present [POINSSOT AND GECKEIS, 2012].

Except thorium and uranium, actinides do not occur naturally and therefore no minerals exist. Thus, synthetic solid phases must be used in studies aiming at the characterization and thermodynamic description of actinide solid phases controlling actinide solubility in aqueous solutions. Actinide oxide or oxy-hydroxide solid phases are usually considered as most relevant solid phases under geochemical conditions. Due to the formation of anionic hydrolysis species, An(V) and An(VI) form also very stable ternary solid phases M–An(V/VI)–OH (M: alkali and alkali-

earth metals) that prevail under alkaline to hyperalkaline pH-conditions [TANANAIEV, 1991a, b; ALTMAIER *et al.*, 2003a; ALMOND *et al.*, 2007; FELLHAUER, 2013; GAONA *et al.*, 2013].

The solubility of actinides is further influenced by the crystallinity of the solid phase, which has a direct impact on the solubility product in accordance with the Schindler equation [SCHINDLER, 1967]. Hence, more amorphous solid phases have greater solubility and vice versa. Amorphous solid phases are preferably expected to form in the solubilization/precipitation phenomena eventually taking place in the context of deep underground repositories for the disposal of radioactive waste. On the other hand, ageing effects and temperature can contribute to an increase of particle size and hence to a decrease of the solubility in the long-term.

Dissolution of actinide oxy-hydroxides is defined by the corresponding solubility product and equilibria with hydrolysis species. These can be formulated either as a function of OH^- or $\text{H}^+/\text{H}_2\text{O}$, which are related by the ionization product of water, K_w :



with the corresponding conditional equilibrium constant at a given I , T and p denoted by the symbol “’”:

$$\lg K'_w = \lg [\text{H}^+] + \lg [\text{OH}^-] \quad (2.3)$$

and the extrapolation to the standard state as denoted by the symbol “°” ($I = 0$, $T = 25^\circ\text{C}$, $p = 1 \text{ bar}$):

$$\begin{aligned} \lg K^\circ_w &= \lg (\text{H}^+) + \lg (\text{OH}^-) - \lg a_w \\ &= \lg K'_w + \lg \gamma_{\text{H}^+} + \lg \gamma_{\text{OH}^-} - \lg a_w \end{aligned} \quad (2.4)$$

where $[\text{X}]$ denotes concentration, (X) activity and γ_{X} corresponds to the activity coefficient of the aqueous species X ; a_w is the activity of water.

The solubility equilibrium of actinide solid phases can be formulated as:



with the corresponding conditional solubility constants (2.6), where the symbol “*” denotes equilibrium constants that involve a deprotonation reaction of the ligand [GUILLAUMONT *et al.*, 2003]:

$$\lg *K'_{s,0} = \lg [\text{An}^{n+}] - n \lg [\text{H}^+] \quad (2.6)$$

and:

$$\begin{aligned} \lg *K^{\circ}_{s,0} &= \lg (\text{An}^{n+}) - n \lg (\text{H}^+) + n \lg a_w \\ &= \lg *K'_{s,0} + \lg \gamma_{\text{An}^{n+}} - n \lg \gamma_{\text{H}^+} + n \lg a_w \end{aligned} \quad (2.7)$$

The hydrolysis of actinides can also be expressed as:



with:

$$\lg * \beta'_{(1,n)} = \lg [\text{An(OH)}_n^{(z-n)}] + n \lg [\text{H}^+] - \lg [\text{An}^{z+}] \quad (2.9)$$

and accordingly:

$$\lg * \beta^{\circ}_{(1,n)} = \lg * \beta'_{(1,n)} + \lg \gamma_{\text{An(OH)}_n^{(z-n)}} + n \lg \gamma_{\text{H}^+} - \lg \gamma_{\text{An}^{z+}} - n \lg a_w \quad (2.10)$$

Experimental studies at $I \neq 0$ allow the quantification of conditional solubility constants at given ionic strength conditions. Equilibrium constants in the standard state ($I = 0$) are then obtained by the extrapolation of the experimentally determined conditional solubility constants using a given activity model (e.g. SIT, Pitzer, see section 2.4). The extrapolation also yields ion interaction parameters according with the ion activity model used.

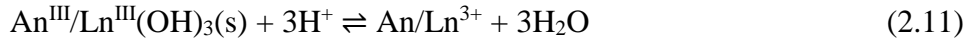
2.2.1 Solubility and hydrolysis of An(III)/Ln(III)

Trivalent actinides and lanthanides form relatively strong hydrolysis species in the neutral to hyperalkaline pH-range. Americium and curium are representative of actinides solely occurring in trivalent oxidation state under the E_h -pH conditions relevant for deep geological repositories for nuclear waste. Although uranium, neptunium and plutonium also occur in +III oxidation state under strongly reducing conditions, the stability fields of U(III) and Np(III) are outside of the E_h -pH conditions relevant for deep geological repositories for nuclear waste. On the contrary, Pu(III) becomes relevant under near-neutral to weakly alkaline pH conditions. Due to their redox stability, most of the experimental studies focusing on trivalent actinides/lanthanides are performed using Am(III), Cm(III) and their lanthanide surrogates Nd(III) or Eu(III).

The current Nuclear Energy Agency – thermodynamic database (NEA-TDB) selection includes three hydrolysis species of Am(III) and one of Pu(III), based on comprehensive solubility, spectroscopic and solvent extraction studies [FUGER *et al.*, 2001; GUILLAUMONT *et al.*, 2003]. After the release of the last NEA-TDB update book, Neck and co-workers studied the solubility and speciation of Nd(III) and Cm(III) in dilute to concentrated NaCl, MgCl₂ and CaCl₂ solutions under repository relevant pH conditions and derived complete and self-consistent chemical, thermodynamic and activity models for the system Na⁺–Mg²⁺–Ca²⁺–H⁺–An(III)/Ln(III)–Cl[–]–OH[–]–H₂O [NECK *et al.*, 2009]. Furthermore, previously obtained solubility data of Am(OH)₃(s) under hyperalkaline conditions were re-evaluated and the aqueous species Am(OH)₄[–] was proposed and the corresponding thermodynamic data derived [VITORGE AND TRAN-THE, 1991; NECK *et al.*, 2009]. Only limited solubility and hydrolysis studies of Pu(III) are available due to the high redox sensitivity of plutonium [FELMY *et al.*, 1989; FUGER *et al.*, 2001]. Recently, Fellhauer evaluated the redox behavior of Pu(IV)/Pu(III) under near-

neutral pH conditions, and provided further insights on the solubility of Pu(III) under very reducing conditions [FELLHAUER, 2013].

$\text{An}^{\text{III}}/\text{Ln}^{\text{III}}(\text{OH})_3(\text{s})$ are the solid phases assumed to control the solubility of An(III)/Ln(III) under repository-relevant pH conditions and absence of complexing ligands. The solubility product of these solid phases can generally be expressed as:



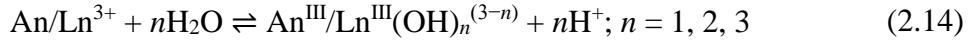
with:

$$\lg *K'_{s,0} = \lg [\text{An}/\text{Ln}^{3+}] - 3 \lg [\text{H}^+] \quad (2.12)$$

and:

$$\lg *K^{\circ}_{s,0} = \lg *K'_{s,0} + \lg \gamma_{\text{An}/\text{Ln}^{3+}} - 3 \lg \gamma_{\text{H}^+} + 3 \lg a_w \quad (2.13)$$

Analog to the solubility product, the formation constants of hydrolysis species of trivalent actinides/lanthanides can be formulated as:



with:

$$\lg \beta'_n = \lg [\text{An}^{\text{III}}/\text{Ln}^{\text{III}}(\text{OH})_n^{(3-n)}] + n \lg [\text{H}^+] - \lg [\text{An}/\text{Ln}^{3+}] \quad (2.15)$$

and accordingly:

$$\lg \beta^{\circ}_n = \lg \beta'_n + \lg \gamma_{\text{An}^{\text{III}}/\text{Ln}^{\text{III}}(\text{OH})_n^{(3-n)}} + n \lg \gamma_{\text{H}^+} - \lg \gamma_{\text{An}/\text{Ln}^{3+}} - n \lg a_w \quad (2.16)$$

2.3 Actinide complexation reactions

A number of inorganic ligands can be expected in the context of a deep geological repository, either as a component of natural groundwater, leached from the geotechnical barriers, or from the waste itself: hydroxide, carbonate, sulfate, phosphate, chloride, fluoride, nitrate and silicate, among others. The formation of complexes with these inorganic ligands can impact the behavior of actinides and promote its mobilization into the biosphere. Because of the strong Lewis acid character of the actinides, the strength of the complexes forming follows the trend defined by the Lewis basicity of the ligand [SILVA AND NITSCHKE, 1995]:



The strength of the complexation of a given ligand with actinides in different oxidation states was already discussed in section 2.1.1 (see equation (2.1)) and is driven by the effective charge of the actinide moiety (+IV > +VI > +III > +V). The complexation of actinides with ligands other than OH⁻ (the hydrolysis of trivalent actinides is discussed in section 2.2.1) can be described as:



with:

$$\lg \beta_{a,0,b}^\circ = \lg [\text{An}_a\text{L}_b] - a \lg [\text{An}^{x+}] - b \lg [\text{L}^{y-}] \quad (2.19)$$

and accordingly:

$$\lg \beta_{a,0,b}^\circ = \lg \beta_{a,0,b}^\circ + \lg \gamma_{\text{An}_a\text{L}_b} - a \lg \gamma_{\text{An}^{x+}} - b \lg \gamma_{\text{L}^{y-}} \quad (2.20)$$

Most of the complexation studies available in the literature describe the formation of binary M–L complexes. Although statistically less likely, the formation of ternary complexes can importantly alter the chemical behavior of a given element, and thus deserves dedicated attention. A number of recent studies have shown the formation of hitherto unknown ternary Ca–An/Ln–OH complexes in alkaline CaCl₂ brines accompanied with an increase in An/Ln(III, IV) solubility [ALTMAYER *et al.*, 2008; RABUNG *et al.*, 2008; NECK *et al.*, 2009; FELLHAUER *et al.*, 2010; FELLHAUER, 2013]. These species do not form in dilute systems, but become predominant in concentrated salt solutions. The stabilization of highly charged moieties by counterions of the matrix solution is also a known mechanism potentially leading to the formation of ternary species. Hence, the predominance of very stable moiety UO₂(CO₃)₃⁴⁻ in carbonated systems with near-neutral pH leads to the formation of very stable ternary Ca/Mg–U(VI)–CO₃ complexes in the presence of Ca or Mg ions in the millimolar range [BERNHARD *et al.*, 1996; KALMYKOV AND CHOPPIN, 2000; BERNHARD *et al.*, 2001; LEE AND YUN, 2013; ENDRIZZI AND RAO, 2014]. The formation of these species is especially relevant, because they can importantly affect the redox equilibrium U(VI)/U(IV).

2.4 Activity models and thermodynamic databases

In aqueous solutions with $I > 0$, the activity of ionic and neutral species is influenced by the interaction with other ions present in solution. Thermodynamic data are based on the activities of aqueous species, and thus the use of approaches allowing the calculation of activity coefficients and accordingly providing the link between concentrations and activities is mandatory for an adequate thermodynamic

description of a given system. The specific ion interaction theory (SIT) and the Pitzer equations [CIAVATTA, 1980; PITZER, 1991] represent the most relevant and accurate activity models used for the description of systems at $I \geq 0.1$ M. In these conditions, the application of simpler approaches such as (extended) Debye-Hückel or Davis can potentially lead to largely erroneous interpretations.

2.4.1 SIT model

SIT represents an improvement of the extended Debye-Hückel equation for the calculation of activity coefficients. The latter equation accounts only for electrostatic, non-specific long-range interactions of oppositely charged ions in dilute solutions ($I \leq 0.1$ M). However, at higher concentrations, short-range, non-electrostatic interactions have to be taken into account. SIT defines an additional term to describe those interactions between two species, the so-called specific ion interaction coefficient [CIAVATTA, 1980; GRENTHE *et al.*, 2013]. These parameters are empirical and have to be experimentally determined. In SIT the activity coefficient γ_i of an aqueous species i is given by the term:

$$\lg \gamma_i = -z_i^2 D + \sum_k \varepsilon_{ik} m_k \quad (2.21)$$

where z_i is the charge of the ion i , m_k is the molality of the counter ion k and ε_{ik} is the specific ion interaction coefficient between the ions i and k . D is the Debye-Hückel term given by:

$$D = \frac{A\sqrt{I_m}}{1 + Ba_i\sqrt{I_m}} \quad (2.22)$$

where I_m is the molal ionic strength:

$$I_m = \frac{1}{2} \sum_i m_i z_i^2 \quad (2.23)$$

A and B are temperature and pressure dependent constants whereas a_i is an ion size parameter for the hydrated ion i . The Debye-Hückel limiting slope A has a value of $0.509 \pm 0.001 \text{ kg}^{1/2} \cdot \text{mol}^{-1/2}$ at 25°C and 1 bar. Ba_i has a value of $1.5 \text{ kg}^{1/2} \cdot \text{mol}^{-1/2}$ at 25°C and 1 bar as proposed by Scatchard [SCATCHARD, 1976; GUILLAUMONT *et al.*, 2003]. However, Ba_i is an empirical parameter and is correlated to ε_{ik} [GUILLAUMONT *et al.*, 2003]. Since the concentration of ions in the ionic medium is typically much larger than the ion concentration of the reacting species, the summation in equation (2.21) can be simplified to equation (2.24) at 25°C and 1 bar [GUILLAUMONT *et al.*, 2003]:

$$\lg \gamma_M = -z_M^2 \frac{0.509\sqrt{I_m}}{1 + 1.5\sqrt{I_m}} + \varepsilon_{MX} m_X \quad (2.24)$$

SIT ion interaction coefficients are set to zero for ions of same charge, since ε describes short-range interactions and usually ions of same charge are far away from each other. The same generally applies to neutral species, although some exceptions are acknowledged for those systems that cannot be properly explained without $\varepsilon(\text{MX}^0, j)$ [GRENTHÉ *et al.*, 2013]. The SIT model is normally considered valid up to $I_m \leq 3.5 \text{ m}$ [GRENTHÉ *et al.*, 2013], although recent studies have shown that SIT can be applied successfully to MgCl_2 and CaCl_2 systems with $I_m \leq 13.5 \text{ m}$ [NECK *et al.*, 2009; FELLHAUER *et al.*, 2010].

2.4.2 Pitzer model

The Pitzer formulism is considered to be the most accurate method for high ionic strengths [HARVIE *et al.*, 1984; CLEGG AND WHITFIELD, 1991]. In contrast to SIT, the Pitzer approach is capable to describe accurately activity coefficients over a large scale of molalities [GRENTHÉ *et al.*, 1992; ROSENBERG *et al.*, 2011], including also the system of oceanic salts [HARVIE *et al.*, 1984]. This is achieved with the use of a large number of parameters, which can only be derived from very large experimental data sets. The latter requirement represents one of the main drawbacks of this approach.

The Pitzer ion interaction model includes the Debye-Hückel term, but considers also semi-empirical binary and triple ion interactions accounted for by specific interaction coefficients. Binary parameters ($\beta^{(0)}_{ij}$, $\beta^{(1)}_{ij}$, $\beta^{(2)}_{ij}$, C^{ϕ}_{ij}) are used to describe the interaction between cations *i* and anions *j*. Mixing parameters θ_{ij} or θ_{ji} (parameters of the function Φ_{ij}) and ψ_{ij} or ψ_{ji} account for interactions with further cations *i'* or anions *j'* in multicomponent (e.g. ternary) systems. The Pitzer approach is based on a virial expansion of the excess Gibbs energy:

$$\begin{aligned} \frac{G^{ex}}{W_w RT} &= f(I) + \sum_i \sum_j m_i m_j \lambda_{ij}(I) + \sum_i \sum_j \sum_k m_i m_j m_k \mu_{ijk} + \dots \end{aligned} \quad (2.25)$$

where W_w is the number of kilograms of water and m_i, m_j, \dots are the molalities of all dissolved species. $f(I)$ includes the Debye-Hückel limiting law and depends only on the ionic strength. $\lambda_{ij}(I)$ and μ_{ijk} are the second and third virial coefficients and represent short-range interactions between the dissolved species.

Activity coefficients of cation M and anion X for mixed electrolytes can be calculated according with equations (2.26) and (2.27), respectively:

$$\begin{aligned}
 \ln \gamma_M &= \\
 &= z_M^2 F + \sum_a m_a (2B_{Ma} + ZC_{Ma}) + \sum_c m_c \left(2\Phi_{Mc} + \sum_a m_a \psi_{Mca} \right) \\
 &+ \sum_{a < a'} \sum_{a'} m_a m_{a'} \psi_{Maa'} + z_M \sum_c \sum_a m_c m_a C_{ca} + 2 \sum_n m_n \lambda_{nM} \\
 &+ \dots
 \end{aligned} \tag{2.26}$$

$$\begin{aligned}
 \ln \gamma_X &= \\
 &= z_X^2 F + \sum_c m_c (2B_{cX} + ZC_{cX}) + \sum_a m_a \left(2\Phi_{Xa} + \sum_c m_c \psi_{cXa} \right) \\
 &+ \sum_{c < c'} \sum_{c'} m_c m_{c'} \psi_{Xcc'} + |z_M| \sum_c \sum_a m_c m_a C_{ca} + 2 \sum_n m_n \lambda_{nX} \\
 &+ \dots
 \end{aligned} \tag{2.27}$$

with $B_{ij} = B_{ji}$, $C_{ij} = C_{ji}$ and $B_{ii} = C_{ii} = 0$, and with:

$$Z = \sum_i m_i |z_i| \tag{2.28}$$

Among others, F includes the Debye-Hückel term:

$$\begin{aligned}
 F &= \\
 &= -A_\phi \left[\frac{I^{1/2}}{(1 + bI^{1/2})} + \frac{2}{b} \ln(1 + bI^{1/2}) \right] + \sum_c \sum_a m_c m_a B'_{ca} \\
 &+ \sum_{c < c'} \sum_{c'} m_c m_{c'} \Phi'_{cc'} + \sum_{a < a'} \sum_{a'} m_a m_{a'} \Phi'_{aa'}
 \end{aligned} \tag{2.29}$$

where A_ϕ is the Debye-Hückel constant for the osmotic coefficients and b is a universal parameter ($1.2 \text{ kg}^{1/2} \cdot \text{mol}^{-1/2}$). The formulism of the terms used in Pitzer equations is provided in the following:

$$B_{MX}^{\phi} = \beta_{MX}^{(0)} + \beta_{MX}^{(1)}e^{-\alpha_1 I^{1/2}} + \beta_{MX}^{(2)}e^{-\alpha_2 I^{1/2}} \quad (2.30)$$

$$B_{MX} = \beta_{MX}^{(0)} + \beta_{MX}^{(1)}g(\alpha_1 I^{1/2}) + \beta_{MX}^{(2)}g(\alpha_2 I^{1/2}) \quad (2.31)$$

$$B'_{MX} = \frac{[\beta_{MX}^{(1)}g'(\alpha_1 I^{1/2}) + \beta_{MX}^{(2)}g'(\alpha_2 I^{1/2})]}{I} \quad (2.32)$$

with:

$$g(x) = \frac{2[1 - (1+x)e^{-x}]}{x^2} \quad (2.33)$$

$$g'(x) = -\frac{2\left[1 - \left(1+x + \frac{x^2}{2}\right)e^{-x}\right]}{x^2} \quad (2.34)$$

and:

$$C_{MX} = \frac{C^{\phi}}{2|z_M z_X|^{1/2}} \quad (2.35)$$

where α_1 and α_2 are universal empirical constants. Main repulsive forces between similar ions are represented by $\beta^{(0)}_{ij}$, whereas $\beta^{(1)}_{ij}$ describes the attraction between oppositely charged ions. $\beta^{(2)}_{ij}$ corrects the deviations caused by electrostatic ion-pair formation and is considered for 2-2 or higher valence electrolytes only. The term C_{ij} is only relevant at high ionic strength. The contribution of the mixing parameters is very small except for the mixing of species with different charge. The complete expressions for the second virial coefficient for mixed solutions Φ_{ij} are:

$$\Phi_{ij} = \theta_{ij} + {}^E\theta_{ij}(I) \quad (2.36)$$

$$\Phi'_{ij} = {}^E\theta'_{ij}(I) \quad (2.37)$$

$$\Phi_{ij}^{\phi} = \theta_{ij} + {}^E\theta_{ij}(I) + I{}^E\theta'_{ij}(I) \quad (2.38)$$

where ${}^E\theta(I)$ and ${}^E\theta'(I)$ account for electrostatic unsymmetrical mixing effects depending on the charged species, ionic strength and solvent properties. The expressions for ions M and N of the same charge are:

$${}^E\theta_{MN} = \frac{z_M z_N}{4I} \left[J(X_{MN}) - \frac{1}{2}J(X_{MM}) - \frac{1}{2}J(X_{NN}) \right] \quad (2.39)$$

$$\begin{aligned} {}^E\theta'_{MN} &= \\ &= -\frac{{}^E\theta_{MN}}{I} + \frac{z_M z_N}{8I^2} \left[X_{MN}J'(X_{MN}) - \frac{1}{2}X_{MM}J'(X_{MM}) - \frac{1}{2}X_{NN}J'(X_{NN}) \right] \end{aligned} \quad (2.40)$$

if $z_M = z_N$ then ${}^E\theta_{MN}(I) = {}^E\theta'_{MN}(I) = 0$. J and J' can be calculated using two Chebyshev polynomial approximations, one for $x \leq 1$ and one for $x \geq 1$ [PITZER, 1991].

Interaction between ions and neutral species are defined with λ_{ni} or λ_{nj} . Hence, the activity coefficients of a neutral species is given by:

$$\ln \gamma_N = 2 \left(\sum_c m_c \lambda_{Nc} + \sum_a m_a \lambda_{Na} + \sum_n m_n \lambda_{Nm} \right) \quad (2.41)$$

For a comprehensive thermodynamic modelling of concentrated aqueous systems and besides the activity of dissolved species, the activity of water a_w in the respective electrolyte has to be taken into account. The activity of water can be calculated from the experimentally determined osmotic coefficient ϕ according with:

$$\ln a_w = -\frac{\phi \sum_i m_i}{\Omega} \quad (2.42)$$

where Ω represents the moles per kilogram of water (55.55) and m_i is the molal concentration of all aqueous species. The osmotic coefficient can be further calculated using the following (Pitzer) equation:

$$\begin{aligned} (\phi - 1) = & \\ = & \left(\frac{2}{\sum_i m_i} \right) \left[\frac{-A_\phi I^{3/2}}{(1 + bI^{1/2})} + \sum_c \sum_a m_c m_a (B_{ca}^\phi + ZC_{ca}) \right. \\ & + \sum_{c < c'} \sum_{c'} m_c m_{c'} \left(\Phi_{cc'}^\phi + \sum_a m_a \psi_{cc'a} \right) \\ & + \sum_{a < a'} \sum_{a'} m_a m_{a'} \left(\Phi_{aa'}^\phi + \sum_c m_c \psi_{caa'} \right) + \sum_n \sum_c m_n m_c \lambda_{nc} \\ & \left. + \sum_n \sum_a m_n m_a \lambda_{na} + \sum_{n < n'} \sum_{n'} m_n m_{n'} \lambda_{nn'} + \frac{1}{2} \sum_n m_n^2 \lambda_{nn} \right] \end{aligned} \quad (2.43)$$

2.4.3 Weak complexes within an ion-interaction approach

The modelling of aqueous systems where weak complexes are formed is very challenging. Hence, the distinction between complex formation and variations in the activity coefficients is often unclear or even arbitrary [GRENTHÉ *et al.*, 2013].

Usually, large changes of the ionic medium are necessary to study weak complex formation, which additionally cause changes of the activity coefficients of the species involved. Note that the NEA-TDB guidelines for the extrapolation to zero

ionic strength discourages the replacement of more than 10% of the background electrolyte by the ligand when assessing the formation of weak complexes [GRENTHÉ *et al.*, 2013]. This limitation, though, can be overcome provided that a spectroscopic proof of the proposed complex is available. In this context, the use of advanced spectroscopic techniques helping in the identification of new aqueous species can provide key inputs in the definition of correct chemical models for complex systems. The availability of correct chemical models is in general very important in solution chemistry, but becomes especially relevant in the description of sorption phenomena, which are very sensitive to the charge of the species sorbing to a given surface.

Among the conventional ligands expected in the context of a repository for nuclear waste disposal, chloride and nitrate are especially prone to the formation of weak complexes with actinides due to their weak Lewis basicity. Stronger ligands such as sulfate can also lead to the formation of weak complexes with An(V) because of the lower effective charge of the AnO_2^+ moiety.

2.4.4 Thermodynamic databases

Thermodynamic databases are extensive, traceable and self-consistent compilations of thermodynamic data, which provide a key input in geochemical calculations and thus represents a fundamental milestone in the safety assessment of repositories for nuclear waste disposal.

The NEA chemical thermodynamic series ([SILVA *et al.*, 1995; FUGER *et al.*, 2001; GUILLAUMONT *et al.*, 2003; RAND *et al.*, 2008], among others) provide the most comprehensive and critically reviewed compilation of thermodynamic data for actinides, fission products and other relevant elements in the framework of nuclear waste disposal. SIT is the activity model chosen in the NEA-TDB for ion activity

corrections. The NEA-TDB is characterized by very strict criteria and guidelines for the selection of thermodynamic data. This strategy results in a sound and very reliable database, which, however, does not usually cover all sub-systems of a given radionuclide due to the restricted number of aqueous species and solid compounds selected. To tackle these limitations, broader databases with less restrictive guidelines for data selection are developed in the context of national programs e.g. PSI-NAGRA TDB [HUMMEL *et al.*, 2002; THOENEN *et al.*, 2014], ThermoChimie [GIFFAUT *et al.*, 2014], Thermodynamic Reference Database (THEREDA) [MOOG *et al.*, 2015].

Among these, only THEREDA database takes advantage of the Pitzer model for ion activity corrections, and thus covers also geochemical calculations in the context of very saline systems such as those expected in rock-salt repositories and deep sedimentary formations with saline porewater.

3 Carbon-14

Carbon-14 is a radioactive nuclide with a half-life of about 5'730 years. Natural C-14 is continuously formed in the upper atmosphere by activation of N-14 (about 80% of air) by cosmic neutrons (~1'500 TBq/year on Earth, [POINSSOT AND GECKEIS, 2012]). Apart from that C-14 was also released from nuclear tests.

Moreover, C-14 is produced by neutron activation of precursor isotopes present in structural metal parts, Zircaloy cladding and nuclear fuel in nuclear reactors. In addition, spent ion exchange resins used for the purification of reactor water also contain C-14, among other radionuclides. Obviously, these materials need to be disposed of in a repository for nuclear waste.

3.1 C-14 production in Zircaloy-4 in light water nuclear power reactors

UO₂ or MOX (mixed oxide) fuel pellets used in water moderated power reactors are usually inserted into fuel rods and sealed air-tight. In addition, the tubes are pressurized with helium to improve the conduction of heat from the fuel to the cladding. The fuel rods are bundled to fuel assemblies (e.g. 15×15, 17×17 lattice). These fuel assemblies are then used to build up the reactor core. The cladding tube of fuel rods are made of Zircaloy, a zirconium based alloy. In addition to its low

neutron absorption, Zircaloy shows good mechanical properties and resistance to corrosion under reactor operation conditions [NEEB, 1997]. However, the corrosion of Zircaloy during reactor operation forms a zirconium oxide layer (ZrO_2 , zirconia) on the external surface of the cladding according to equation (3.1) [GRAS, 2014]. The thickness of the ZrO_2 layer along the fuel rod depends on the thermal history of the rod, but usually remains below 100 μm for light water nuclear power reactors [GRAS, 2014].



Zircaloy-4 is used in pressurized water reactors (PWR) whereas Zircaloy-2 (Zry-2) is used in boiling water reactors (BWR). In contrast to Zircaloy-2, Zircaloy-4 does not contain nickel to reduce the absorption of hydrogen, which is more likely to occur in PWRs than in BWRs [BAILLY *et al.*, 1999].

The principle source of C-14 in Zircaloy is the activation of nitrogen-14 ($^{14}N(n,p)^{14}C$), carbon-13 ($^{13}C(n,\gamma)^{14}C$) and oxygen-17 ($^{17}O(n,\alpha)^{14}C$) by neutrons during reactor operation (equations (3.2) to (3.4)). N-14 is the main naturally occurring nitrogen isotope (99.63%), whereas C-13 (1.1%) and O-17 (0.038%) are low abundance naturally occurring carbon and oxygen isotopes, respectively [MAGILL *et al.*, 2006]. A very small amount of C-14 is also formed by ternary fission in the nuclear fuel.



Nitrogen and carbon are present as impurities in nuclear fuel, Zircaloy cladding and other reactor core structures. However, N-14 is the main source of C-14 due to its

isotopic abundance and large thermal neutron capture cross-section (1.821 barn, [MAGILL *et al.*, 2006]). The content of N-14 in Zircaloy-4 is typically less than 80 ppm [NEEB, 1997; BAILLY *et al.*, 1999; RUDLING *et al.*, 2007].

Only limited studies of C-14 quantification and/or speciation in irradiated Zircaloy are available. Bleier and co-workers [BLEIER *et al.*, 1984; BLEIER *et al.*, 1987; BLEIER *et al.*, 1988; NEEB, 1997] determined the inventory of C-14 in Zircaloy-2 cladding specimens (estimated N-14 impurity: 35 ppm) of a BWR UO₂ fuel rod with an average burn-up of 22.4 GWd/t_{HM} and Zircaloy-4 cladding specimens (estimated N-14 impurity: 40 ppm) of a PWR MOX fuel rod with an average burn-up of 35.7 GWd/t_{HM} using fusion with KHSO₄. The C-14 inventory was determined to 2.6×10^4 Bq/(g Zry-2) and to 1.9×10^4 Bq/(g Zry-4), respectively and compared to calculations of the C-14 inventory as a function of local burn-up of the fuel rod. Further, the axial distribution of C-14 in the studied Zircaloy-2 cladding was almost homogeneous and small deviations were in agreement with the local burn-up of the investigated BWR fuel rod [BLEIER *et al.*, 1984; BLEIER *et al.*, 1987; NEEB, 1997]. The chemical form of C-14 in the Zircaloy-2 cladding could not be determined from the experiments performed by the authors [BLEIER *et al.*, 1984; BLEIER *et al.*, 1987; NEEB, 1997].

Following the inventory analysis [BLEIER *et al.*, 1984; BLEIER *et al.*, 1987; BLEIER *et al.*, 1988; NEEB, 1997], Bleier et al. investigated the chemical form of C-14 after leaching of Zircaloy cladding material from spent PWR and BWR fuel rods for three months at 200°C in saturated NaCl solution and presence of F⁻; they presented their results in a report of a project funded by German Federal Ministry for Research and Technology (BMFT) [Bleier *et al.*, 1988]. About 50% of C-14 inventory in Zircaloy-4 and about 90% of C-14 inventory present in Zircaloy-2 is released during the leaching experiments. More than 95% of the released C-14 was found in the organic/CO fraction, whereas only less than 5% of C-14 was found in the inorganic fraction; the vast majority of C-14 was found in the gas phase of the

leaching experiments [BLEIER *et al.*, 1988]. In digestion experiments performed with Zircaloy specimens in dilute hydrofluoric acid at room temperature about 95% of the C-14 inventory of Zircaloy-4 was released into the gas phase in contrast to about 92% of the C-14 inventory of Zircaloy-2 [BLEIER *et al.*, 1988]. Moreover, > 99% of the released C-14 was found in the organic/CO fraction whereas < 1% of C-14 was found in the inorganic fraction [BLEIER *et al.*, 1988]. However, the authors only determined the chemical form of C-14 released during leaching from Zircaloy-2 and Zircaloy-4 specimens directly or after acidification (using concentrated HCl) of the leachant into the gas phase, same is true for the digestion in HF. [BLEIER *et al.*, 1988] did not analyze the chemical form of C-14 in the aqueous phase of the leaching and digestion experiments (e.g. dissolved hydrocarbons).

[YAMAGUCHI *et al.*, 1999; TANABE *et al.*, 2007; TAKAHASHI *et al.*, 2013] studied the inventory of C-14 in irradiated Zircaloy specimens and in the Zircaloy oxide layer separately from an irradiated PWR fuel rod (average burn-up: 47.9 GWd/t_{HM}) and a BWR fuel rod (average burn-up: 39.4 GWd/t_{HM}) using digestion in HNO₃/HF. They reported inventories of about 3.2×10⁴ Bq/(g Zry-4) for the PWR fuel rod (N-14 impurity: 47 ppm) and 1.9×10⁴ Bq/(g Zry-2) (N-14 impurity: 34 ppm) for the BWR fuel rod and further compared the experimental inventory with calculations. Moreover, the authors reported inventories of the oxide layer of about 4.4×10⁴ Bq/(g Zry-4) for the PWR fuel rod and 3.3×10⁴ Bq/(g Zry-2) in case of the BWR fuel rod. The inventories in the oxide layer was by a factor 1.5 to 1.7 higher than in the Zircaloy metal in both cases. Activation calculations performed with 40 ppm N-14 content assumed in the oxide layer and taking into account the ¹⁷O(n,α)¹⁴C reaction were consistent with the C-14 inventories found in the oxide layer [SAKURAGI *et al.*, 2013]. In addition, leaching tests up to 5.5 months using “cement equilibrium simulated groundwater” (pH 12.5, E_h -200 mV) showed that about 80%–100% of the C-14 leached from the Zircaloy specimens into the aqueous

phase was organic. However, no gaseous C-14 bearing compounds were detected [YAMAGUCHI *et al.*, 1999].

Nitrogen and carbon are possibly present in Zircaloy before irradiation as interstitial solid solutions, nitrides of the alloying metals (e.g. ZrN, Fe₂N), carbon as metal carbides (e.g. ZrC, Fe₃C) and/or may be present as metal carbonitrides (e.g. Zr_xC_yN_z) [GRAS, 2014; SWANTON *et al.*, 2014].

Gras and Swanton *et al.* argued that C-14 after activation of Zircaloy would be present as interstitial C-14 from interstitial nitrogen and/or as carbides/carbonitrides if the nitrogen is originally present as nitride [GRAS, 2014; SWANTON *et al.*, 2014]. However, the chemical form of C-14 produced by activation in Zircaloy is far from clear and radiocarbon and non-radioactive carbon could have different chemical environments [GRAS, 2014; SWANTON *et al.*, 2014]. C-14 in the Zircaloy oxide layer is possibly present as solid solution [GRAS, 2014]. Further [SMITH AND BALDWIN, 1993] observed in thermal C-14 release experiments from spent PWR Zircaloy claddings that C-14 is not only present occluded within the ZrO₂ but also present in the crud layer (oxides deposited from the coolant during reactor operation) which is readily available for release [SMITH AND BALDWIN, 1993; NEEB, 1997; GRAS, 2014].

3.2 C-14 in Zircaloy-4 in the context of deep geological nuclear waste repositories

A number of countries, among those Finland, Germany, Sweden and Switzerland have decided to directly dispose irradiated UO₂ and MOX fuels, denoted as spent nuclear fuel (SNF). C-14 is a key radionuclide in safety assessments of such geological disposal facilities for SNF due to its long half-life and assumed mobility. Following scenario is taken into consideration for a long-term safety analysis: upon contact with groundwater, corrosion of Zircaloy cladding possibly lead to the formation of volatile and/or dissolved C-14 bearing compounds such as gaseous or dissolved hydrocarbons (e.g. methane, alcohols, aldehydes or carboxylic acids). These compounds reveal a high mobility either in the gaseous or in the aqueous phase and, once released, are possibly transported into the biosphere, where C-14 may be metabolized by any kind of organism. On the other hand, volatile/dissolved inorganic C-14 bearing compounds such as CO₂, carbonates or bicarbonates are affected by sorption and precipitation mechanisms in the near field of a repository and, therefore, their release into the biosphere is significantly retarded.

4 Materials and Methods

4.1 Chemicals and radionuclides used in the present work

4.1.1 Chemicals

All solutions were prepared with ultrapure water, purified with a MilliQ[®] Advantage A10 water purification system (Merck Millipore, 18.2 M Ω ·cm, $T = 22 \pm 2^\circ\text{C}$, pore size 0.22 μm and < 4 ppb TOC) and purged several hours with argon before use to remove traces of O₂ and CO₂.

Table 4.1 lists all chemicals used in this work. The chemicals were used in the experiments without further purification.

Materials and Methods

Table 4.1: Chemicals used in the present work.

name	grade	chemical formula	molar weight [g/mol]	company
1 wt.% platinum on alumina pellets (3.2 mm)		Pt/Al ₂ O ₃		Sigma-Aldrich
brucite	Ultra	Mg(OH) ₂ (cr)	58.3	Fluka
calcium chloride dihydrate	ACS	CaCl ₂ ·2H ₂ O	147.0	Merck
calcium nitrate tetrahydrate	ACS	Ca(NO ₃) ₂ ·4H ₂ O	236.2	Merck
CHES	A.R.	C ₈ H ₁₇ NO ₃ S	207.3	Sigma-Aldrich
copper oxide wire (0.65 mm × 6 mm)	ACS	CuO/Cu ₂ O		Merck
ethanol (absolute)	ACS	CH ₃ CH ₂ OH	46.1	VWR Chemicals
HEPES	A.R.	C ₈ H ₁₈ N ₂ O ₄ S	238.3	Sigma-Aldrich
hydrochloric acid		HCl		Merck Titrisol [®]
hydrofluoric acid (40%)	suprapur [®]	HF		Merck
KPS		K ₂ S ₂ O ₈	270.3	Merck Emsure [®]
magnesium chloride hexahydrate	ACS	MgCl ₂ ·6H ₂ O	203.3	Merck
magnesium nitrate hexahydrate	ACS	Mg(NO ₃) ₂ ·6H ₂ O	256.4	Merck
neodymium(III) oxide	A.R.	Nd ₂ O ₃ (cr)	336.5	Merck
nitric acid (65%)	suprapur [®]	HNO ₃		Merck
nitrogen	99.99%	N ₂ (g)		Alphagaz [™] 2, Air Liquide
10% methane/ 90% argon mixture	99.99%	CH ₄ (g)/Ar(g)		Air Liquide
portlandite	ACS	Ca(OH) ₂ (cr)	74.1	Merck
silver nitrate	A.R.	AgNO ₃	169.9	VWR Chemicals
sodium chloride	ACS	NaCl	58.4	Merck
sodium hydroxide (1 molar)		NaOH		Merck Titrisol [®]
sodium hydroxide (2 molar)		NaOH		Merck Titripur [®]
sodium nitrate	ACS	NaNO ₃	84.9	Merck
sulfuric acid (95–97%)		H ₂ SO ₄	98.1	Merck Emsure [®]
TRIS	A.R.	C ₄ H ₁₁ NO ₃	121.1	Sigma-Aldrich
TRIS·HCl	A.R.	C ₄ H ₁₁ NO ₃ ·HCl	157.6	Sigma-Aldrich
AMP	A.R.	(NH ₄)PMO ₁₂ O ₄₀	1876.4	Bio-Rad Laboratories

4.1.2 Cm(III) for TRLFS measurements

A 2×10^{-5} M Cm(III) stock solution in 0.1M HClO₄ was used for TRLFS experiments. The isotopic composition of curium was 89.7% Cm-248, 9.4% Cm-246, 0.4% Cm-243, 0.3% Cm-244, 0.1% Cm-245 and 0.1% Cm-247.

4.1.3 C-14 standard material for recovery tests

Carbon-14 labeled inorganic and organic reference material were used for testing the recovery of the carbon-14 extraction and analysis system, Carbon-14 doped sodium carbonate (Na₂¹⁴CO₃) in water was obtained by Eckert & Ziegler Strahlen- und Medizintechnik AG (39.6kBq/mL, 1.07 μCi/mL), [1,2-¹⁴C]-acetic acid (sodium salt, ¹⁴CH₃¹⁴CO₂Na) in ethanol was purchased from PerkinElmer (3.7MBq/mL, 0.1 mCi/mL) and [¹⁴C]-formic acid (sodium salt, ¹⁴CHO₂Na) in ethanol/water (7:3) was obtained from Hartmann Analytic (3.7MBq/mL, 0.1 mCi/mL).

4.1.4 Other radionuclides used in this work

Other radionuclide standard materials used in this work includes tritium (H-3, T), chlorine-36 and iodine-129. H-3, Cl-36 and I-129 may hinder the recovery process of C-14 and/or leads to cross-contamination during the recovery of C-14 in the extraction and analysis system. Therefore, recovery tests were conducted with standards of H-3, Cl-36 and I-129. Tritium (chemical form: ¹H-³H-O, HTO,

49.24 kBq/mL, 1.33 μ Ci/mL) was obtained by Amersham plc. Chlorine-36 (Na^{36}Cl in H_2O , 369.1 kBq/mL, 9.98 μ Ci/mL) and iodine-129 (Na^{129}I in 0.1 M NaOH, 194.7 kBq/mL, 5.26 μ Ci/mL) were purchased from Eckert & Ziegler Strahlen- und Medizintechnik AG.

4.2 Materials synthesized for studies with Nd(III)

4.2.1 Preparation of $\text{Nd}(\text{OH})_3(\text{s})$ and magnesium oxychloride phases at room temperature

Lanthanide and actinide oxides ($\text{M}_2\text{O}_3(\text{cr})$) are usually not stable in aqueous solutions and transform into the respective hydroxides [SILVA *et al.*, 1995; DIAKONOV *et al.*, 1998a; DIAKONOV *et al.*, 1998b]. $\text{Nd}(\text{OH})_3(\text{s})$ was prepared by hydration of crystalline $\text{Nd}_2\text{O}_3(\text{cr})$ in pure water under argon atmosphere and room temperature as described in [NECK *et al.*, 2009]. The oxide was stored under water for about three months. Then, the complete solid phase transformation was confirmed by XRD (PDF 70-0215) [BEALL *et al.*, 1976; NECK *et al.*, 2009].

Mg-oxychloride ($\text{Mg}_2(\text{OH})_3\text{Cl}\cdot 4\text{H}_2\text{O}(\text{cr})$) was synthesized at room temperature by transformation of brucite in concentrated MgCl_2 solutions (≥ 2.5 M) and argon atmosphere as described in [ALTMAYER *et al.*, 2003b].

4.2.2 Preparation of $\text{Nd}(\text{OH})_2\text{Cl}(\text{s})$ phases at $T = 22$ and 80°C

About 600 mg of $\text{Nd}(\text{OH})_3(\text{s})$ synthesized as described in section 4.2.1 was stored in 30 mL 5.15 m MgCl_2 under argon atmosphere and $T = 22 \pm 2^\circ\text{C}$. The solution was buffered with TRIS (0.01 M) and the pH_m was adjusted to about 8.0 using HCl. The solid phase was stored in the concentrated magnesium chloride solution for 42 days. The complete transformation of the initial $\text{Nd}(\text{OH})_3(\text{s})$ into $\text{Nd}(\text{OH})_2\text{Cl}(\text{s})$ was confirmed by X-ray diffraction (XRD) (PDF 72-1812) [BUKIN, 1972].

Moreover, the transformation of $\text{Nd}(\text{OH})_3(\text{s})$ into $\text{Nd}(\text{OH})_2\text{Cl}(\text{s})$ was also assessed at $T = 80 \pm 3^\circ\text{C}$ and $8.7 \leq \text{pH}_m \leq 9.6$ in 5.61 m NaCl, 0.25, 1.03, 2.67, 3.87 and 5.15 m MgCl_2 , as well as 3.91 m CaCl_2 . Seven autoclaves ($V = 50\text{mL}$) equipped with polytetrafluoroethylene (PTFE) liner (see Figure 4.1) were prepared with about 20 mg $\text{Nd}(\text{OH})_3(\text{s})$ and 30 mL of background electrolyte (pH-unbuffered) under argon atmosphere. The autoclaves were sealed air tight (with a torque of 25 Nm) and placed in an oven (in presence of air) for 40 days at $T = 80 \pm 3^\circ\text{C}$. Solid phases recovered from the autoclaves were characterized by XRD and scanning electron microscope – energy dispersive X-ray spectroscopy (SEM-EDS).



Figure 4.1: Images of the autoclave and PTFE liner used for the hydrothermal preparation of $\text{Nd}(\text{OH})_2\text{Cl}(\text{s})$ at 80°C . The picture on the left shows the autoclave itself whereas the picture on the right shows the PTFE liner used in the autoclave.

4.2.3 Preparation of neodymium batch solubility experiments

All samples were prepared and stored in argon glove boxes under exclusion of oxygen ($\text{O}_2 < 5 \text{ ppm}$, $T = 22 \pm 2^\circ\text{C}$) and CO_2 . All solutions were prepared volumetrically and the resulting molar concentrations were converted into the molal scale with density values calculated using Pitzer equations with data reported elsewhere [HARVIE *et al.*, 1984; PITZER, 1991]. Batch solubility experiments of $\text{Nd}(\text{III})$ were performed in Polyvials[®] (HDPE, Zinsser Analytic) from undersaturation conditions with $\text{Nd}(\text{OH})_3(\text{s})$ or $\text{Nd}(\text{OH})_2\text{Cl}(\text{s})$ as solid phase.

The pH in the samples was adjusted by the addition of organic buffers ($150 \mu\text{L}$ 1.0M HEPES ($7.0 \leq \text{pH} \leq 7.9$), TRIS ($8.0 \leq \text{pH} \leq 8.5$) or CHES ($8.6 \leq \text{pH} \leq 10.0$))

to reach a final buffer concentration of 10mM in the samples), brucite/Mg-oxychloride, portlandite, HCl and NaOH. The absence of any impact of these organic buffers on An^{III}/Ln^{III} speciation was confirmed in a previous study [WEISER *et al.*, 2011]. The precipitation of brucite/Mg-oxychloride constrains the pH_m within a range of 8.6 and 9.1 depending upon $MgCl_2$ concentration [ALTMAYER *et al.*, 2003b] and/or nitrate concentration [p.w.]. In the calcium system, portlandite/ $Ca_2Cl_2(OH)_2 \cdot H_2O$ paragenesis buffers the pH_m to ~ 12 depending on the $CaCl_2$ concentration. The pH_m controlled by these solid phases is denoted as “ pH_{max} ” for $MgCl_2$, $MgCl_2$ – $Mg(NO_3)_2$, $CaCl_2$ and $CaCl_2$ – $Ca(NO_3)_2$ systems in the following. The pH and $m_{Nd(III)}$ were systematically monitored up to 398 days and the Nd(III) concentration in aqueous solution was determined as described in section 4.3.2. Solid phase characterization was performed as described in section 4.8. Although equilibria were typically obtained within a few days, solid phase characterization was performed after > 79 days.

4.2.3.1 Preparation of batch solubility experiments in Na–Mg–Ca–Cl–NO₃ solutions with Nd(OH)₃(s)

Five series of solubility experiments were prepared with different total salt concentrations of NaCl–NaNO₃ (0.1–6.02 m) and $MgCl_2$ – $Mg(NO_3)_2$ (0.25–5.24 m) mixtures, whereas only two series were prepared in the case of $CaCl_2$ – $Ca(NO_3)_2$ (2.85 and 4.02 m) mixtures (Table 4.2). A total of 199 independent samples were prepared for this study. Na^+ , Mg^{2+} and Ca^{2+} concentrations were fixed within series of constant ionic strength and the concentrations of Cl^- and NO_3^- were varied according to a fixed pattern (Table 4.2). Nitrate concentrations ranged between 0 and 8.0 m per batch solubility experiment. The solubility of nitrate in the series 5.24 m $MgCl_2$ – $Mg(NO_3)_2$ was limited to $m_{NO_3^-} \leq 2.32$ m. For each ionic strength

and $\text{Cl}^-/\text{NO}_3^-$ mixture, a set of (at least) three independent samples was prepared within $7.5 \leq \text{pH}_m \leq 13.2$, with 15 mL background electrolyte and 6–12 mg $\text{Nd}(\text{OH})_3(\text{s})$.

4.2.3.2 Preparation of batch solubility experiments in concentrated NaCl, MgCl₂ and CaCl₂ solutions with Nd(OH)₂Cl(s)

Batch solubility experiments with $\text{Nd}(\text{OH})_2\text{Cl}(\text{s})$ were performed in NaCl (5.61 m), MgCl_2 (2.11, 2.67, 3.87 and 5.15 m) and CaCl_2 (2.68 and 3.91 m) background electrolytes (see Table 4.3). For each ionic strength and salt type, a set of four to six independent samples was prepared within $7.0 \leq \text{pH}_m \leq 13.0$, with 15 mL background electrolyte and 10–15 mg $\text{Nd}(\text{OH})_2\text{Cl}(\text{s})$ which was synthesized at room temperature (see also section 4.2.2). Before use, the solid phase was washed two times with MilliQ[®] water to remove the background electrolyte (5.15 m MgCl_2). Additional experiments containing both $\text{Nd}(\text{OH})_3(\text{s})$ and $\text{Nd}(\text{OH})_2\text{Cl}(\text{s})$ were performed under pH-unbuffered conditions with analogous background electrolytes and salt concentrations. About 10 to 15 mg of $\text{Nd}(\text{OH})_3(\text{s})$ and $\text{Nd}(\text{OH})_2\text{Cl}(\text{s})$ (obtained from room temperature preparation, washed twice with MilliQ[®] water) were suspended into 15 mL background electrolyte. These experiments are denoted as “mixing” experiments in the following.

Table 4.2: Summary of the matrix solutions used in the Nd(OH)₃(s) batch solubility experiments. At least three independent samples prepared for each mixed system within $7.5 \leq \text{pH}_m \leq 13.2$ (Na⁺), $7.5 \leq \text{pH}_m \leq 9.0$ (Mg²⁺) and $7.5 \leq \text{pH}_m \leq 12.0$ (Ca²⁺).

$m_{\text{Na}^+}^{\text{a)}$	$m_{\text{NaCl}} / m_{\text{NaNO}_3} \text{ or } m_{\text{MCl}_2} / m_{\text{M(NO}_3)_2} \text{ with M = Mg}^{2+} \text{ or Ca}^{2+}$					
0.10	0.10/0.00	0.00/0.10				
0.51	0.51/0.00	0.40/0.10	0.30/0.20	0.00/0.51		
1.02	1.02/0.00	0.92/0.10	0.82/0.20	0.51/0.51	0.00/1.03	
2.64	2.64/0.00	2.57/0.11	2.47/0.21	2.16/0.54	1.63/1.09	0.00/2.72
5.61	5.61/0.00	5.61/0.11	5.50/0.23	5.17/0.57	4.61/1.15	3.48/2.32 2.90/2.90 1.75/4.08 0.00/6.02
$m_{\text{Mg}^{2+}}^{\text{a)}$						
0.25	0.25/0.00	0.20/0.05	0.15/0.10			
1.04	1.04/0.00	0.99/0.05	0.94/0.10	0.79/0.26	0.53/0.53	0.00/1.07
2.80^{b)}	2.80/0.00	2.75/0.06	2.70/0.11	2.54/0.28	2.27/0.57	1.72/1.14
4.05^{b)}	4.05/0.00	4.00/0.06	3.94/0.12	3.77/0.29	3.49/0.58	2.91/1.16
5.24^{c)}	5.24/0.00	5.19/0.06	5.13/0.12	4.95/0.29	4.65/0.58	4.05/1.16
$m_{\text{Ca}^{2+}}^{\text{a)}$						
2.85	2.85/0.00		2.74/0.11	2.57/0.29	2.30/0.57	1.73/1.16
4.02						1.15/2.87
$m_{\text{NO}_3^-}^{\text{a)}$	0.00	0.10	0.20	0.51	1.03	2.14 2.72 4.08 5.74 8.04

^{a)} Axis labels refer to the lowest salt/nitrate concentration within a series/group and deviations are due to density changes of the matrix solutions.

^{b)} Additional pH_{max} series buffered with brucite instead of Mg-oxychloride.

^{c)} Samples with $m_{\text{NO}_3^-} > 2.32\text{m}$ were found to be sparingly soluble.

Table 4.3: Summary of the matrix solutions and investigated pH_m in the Nd(III) batch solubility experiments with $Nd(OH)_2Cl(s)$.

sample system*	investigated pH_m						
NaCl							
5.61	7.0	7.5	8.0		9.0	10.0	12.0
MgCl₂							
2.11	7.0	7.5	8.0	8.5			
2.67	7.0	7.5	8.0	8.5	pH_{max}		
3.87	7.0	7.5	8.0	8.5	pH_{max}		
5.15	7.0	7.5	8.0	8.5	pH_{max}		
CaCl₂							
2.68	7.0	7.5		8.5			
3.91	7.0	7.5		8.5	9.5	11.0	pH_{max}

* m_{NaCl} or m_{MCl_2} with $M = Mg^{2+}$ or Ca^{2+}

4.3 Analysis methods applied to studies with Nd(III)

4.3.1 pH measurements

4.3.1.1 General definition of pH

A thermodynamically sound definition of the pH was provided by [SORENSEN AND LINDERSTROM-LANG, 1924; BATES, 1948; BUCK *et al.*, 2002] as the negative logarithm of the H^+ ion activity a_{H^+} :

$$\text{pH} = -\log a_{\text{H}^+} = -\log^{\text{m}} \gamma_{\text{H}^+} - \log m_{\text{H}^+} = -\log^{\text{c}} \gamma_{\text{H}^+} - \log c_{\text{H}^+} \quad (4.1)$$

where m_{H^+} and c_{H^+} are the molal and molar H^+ concentrations, respectively, and $^{\text{m}}\gamma_{\text{H}^+}$ and $^{\text{c}}\gamma_{\text{H}^+}$ are the single-ion activity coefficients of H^+ . Since the activity coefficients cannot be experimentally determined a widely accepted pH scale was introduced [BUCK *et al.*, 2002]. The primary method allows to measure the pH in dilute systems ($I \leq 0.1 \text{ M}$) as closely as possible to the thermodynamic definition of the pH. Dilute standard buffers of known pH are used for calibration of an electrochemical cell with H^+ sensitive electrode, known as Harned cell:



The potential difference E is given by the Nernst equation:

$$E = E_0 - (R \cdot T \cdot \ln 10) / F \cdot \lg (a_{\text{H}^+} \cdot m_{\text{Cl}^-} \cdot \gamma_{\text{Cl}^-}) \quad (4.3)$$

and with the standard potential E_0 of the $\text{Ag} | \text{AgCl}$ electrode. E_0 is measured as function of m_{Cl^-} and the quantity $a_{\text{H}^+} \cdot \gamma_{\text{Cl}^-}$ (called acidity function pa) is found by extrapolation to zero chloride molality (pa_0).

$$\text{pa} = -\lg (a_{\text{H}^+} \cdot \gamma_{\text{Cl}^-}) \rightarrow \text{pa}_0 = -\lg (a_{\text{H}^+} \cdot \gamma_{\text{Cl}^-})_{m_{\text{Cl}^-} \rightarrow 0} \quad (4.4)$$

γ_{Cl^-} is then obtained by the Bates-Guggenheim convention based on the Debye-Hückel theory. At low ionic strength ($I < 0.1 \text{ m}$) the ion size parameter of the Debye-Hückel theory is set equal to 1.5:

$$\text{pH} = \text{pa}_0 + \gamma_{\text{Cl}^-} \quad (4.5)$$

4.3.1.2 pH measurements using glass electrodes

For determining the pH of a given solution, electrochemical cells consisting of a glass electrode (GE) sensitive to H^+ ions and a reference electrode (REF) with junction are normally used. The combination of both electrodes in a single (glass) body is commonly named as pH-electrode. The potential between the two electrodes (GE and REF) is measured by a pH-meter (voltmeter) connected to the pH-electrode and can be expressed by:

$$E = E^\circ(\text{REF}) - E^\circ(\text{GE}) + E_{AS} - [(R \cdot T \cdot \ln 10) / F] \cdot \lg a_{H^+} + E_j \quad (4.6)$$

$E^\circ(\text{REF})$ and $E^\circ(\text{GE})$ are the temperature dependent potentials of the reference and the glass electrode, respectively. E_{AS} is the asymmetry potential of the glass electrode (GE) and E_j is the liquid junction potential at the interface between the reference electrolyte and the respective sample solution. The term $(R \cdot T \cdot \ln 10) / F$ in equation (4.6) is the Nernst factor and has a value of 59.16 mV at $T = 25^\circ\text{C}$. The unknown pH of a sample solution, $\text{pH}(\text{X})$, can be determined as the difference between the potential $E(\text{X})$ of the unknown sample solution and the adjusted standard pH buffer potential $E(\text{S})$ in mV [BUTLER AND COGLEY, 1998]:

$$\text{pH}(\text{X}) = \text{pH}(\text{S}) + [E(\text{S}) - E(\text{X})] \cdot [F / (R \cdot T \cdot \ln 10)] + [E_j(\text{X}) - E_j(\text{S})] \cdot [F / (R \cdot T \cdot \ln 10)] \quad (4.7)$$

with

$$E(\text{S}) = E(\text{REF}) - E(\text{GE}) - E_{AS} + [(R \cdot T \cdot \ln 10) / F] \cdot \lg a_{H^+}(\text{S}) + E_j(\text{S}) \quad (4.8)$$

and

$$E(\text{X}) = E(\text{REF}) - E(\text{GE}) - E_{AS} + [(R \cdot T \cdot \ln 10) / F] \cdot \lg a_{H^+}(\text{X}) + E_j(\text{X}) \quad (4.9)$$

During calibration of pH, the terms E_{AS} , $E(\text{REF})$ and $E(\text{GE})$ cancel out as they remain the same in the calibration and the measurements of sample solutions.

Therefore, $\text{pH}(X)$ can be determined if the difference in the liquid junction potentials $E_j(X)$ and $E_j(S)$ is negligible. This is true for buffer and unknown sample solutions of low and similar ionic strengths ($I \leq 0.1$ m). For samples with elevated ionic strength, a modified approach needs to be considered [BUTLER AND COGLEY, 1998] since the standard method is no longer valid.

4.3.1.3 pH measurements in saline solutions

At elevated ionic strength ($I > 0.1$ m) the activity coefficient of H^+ as well as the liquid junction potential are significantly affected by ion interaction processes and conventional pH measurements only valid for dilute solutions, and can no longer be used. For pH measurements at elevated ionic strength the proton concentration rather than the proton activity is used [KNAUSS *et al.*, 1990]:

$$\text{pH}_m = -\lg m_{\text{H}^+} \text{ and } \text{pH}_c = -\lg c_{\text{H}^+} \quad (4.10)$$

pH_m and pH_c are the negative logarithm of the molal and molar proton concentration, respectively. They are obtained from the experimentally measured pH_{exp} using empirical correction factors (A-values), which include a contribution ΔE_j entailing the difference in liquid junction potential E_j between dilute pH buffer solutions for calibration and samples with high background electrolyte concentration and the single-ion activity coefficient of H^+ :

$$\text{pH}_m = \text{pH}_{\text{exp}} + A_m \text{ and } \text{pH}_c = \text{pH}_{\text{exp}} + A_c \quad (4.11)$$

A-values for a specific system (salt type and concentration) are experimentally assessed by measuring a set of reference sample solutions with known H^+ concentrations.

4.3.1.4 pH measurements and A_m -values determined in this work

The molal H^+ concentration was determined with combination pH-electrodes (type Orion Ross, Thermo Scientific). Empirical A_m values for NaCl, $MgCl_2$ and $CaCl_2$ systems were previously reported elsewhere [ALTMAYER *et al.*, 2003b; ALTMAYER *et al.*, 2008]. A_m values of pure nitrate systems and nitrate-chloride mixtures were experimentally determined in the present work with standard solutions containing 2×10^{-2} – 6.25×10^{-4} M HCl in 0.1–6.02 m NaCl– $NaNO_3$, 0.25–5.24 m $MgCl_2$ – $Mg(NO_3)_2$ and 2.91/4.02 m $CaCl_2$ – $Ca(NO_3)_2$ mixtures.

A_m values determined for NaCl– $NaNO_3$, $MgCl_2$ – $Mg(NO_3)_2$ and $CaCl_2$ – $Ca(NO_3)_2$ solutions are provided in Table 4.4 and Figure 4.2, together with A_m values available for NaCl, $MgCl_2$ and $CaCl_2$ systems as reported in the literature [ALTMAYER *et al.*, 2003b]. A_m values for the different Cl^- – NO_3^- mixtures considered in this work were calculated based on the linear correlation with total NO_3^- concentration (Table 4.4).

Table 4.4: Equations empirically determined in this work for the calculation of A_m values in NaCl– $NaNO_3$, $MgCl_2$ – $Mg(NO_3)_2$ and $CaCl_2$ – $Ca(NO_3)_2$ mixtures.

System	Equation	System	Equation
m_{Na^+}		$m_{Mg^{2+}}$	
0.10	$A_m = +0.0994 \cdot m_{NO_3^-} - 0.0800$	0.25	$A_m = -0.0181 \cdot m_{NO_3^-} + 0.0276$
0.51	$A_m = -0.0590 \cdot m_{NO_3^-} - 0.0100$	1.04	$A_m = -0.0272 \cdot m_{NO_3^-} + 0.3975$
1.02	$A_m = -0.0484 \cdot m_{NO_3^-} + 0.0800$	2.80	$A_m = -0.0528 \cdot m_{NO_3^-} + 1.2722$
2.64	$A_m = -0.0406 \cdot m_{NO_3^-} + 0.3616$	4.05	$A_m = -0.0548 \cdot m_{NO_3^-} + 1.9306$
5.61	$A_m = -0.0572 \cdot m_{NO_3^-} + 0.9057$	5.24	$A_m = -0.1302 \cdot m_{NO_3^-} + 2.7424$
$m_{Ca^{2+}}$			
2.85	$A_m = -0.0514 \cdot m_{NO_3^-} + 1.1095$		
4.02	$A_m = -0.0708 \cdot m_{NO_3^-} + 1.7029$		

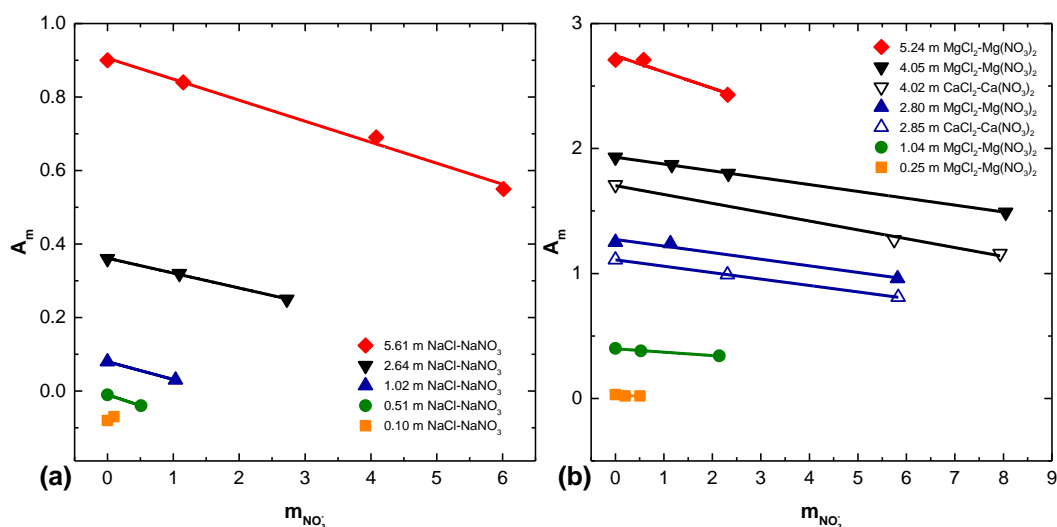


Figure 4.2: A_m values experimentally determined for different (a) NaCl–NaNO₃, (b) MgCl₂–Mg(NO₃)₂ (closed symbols) and CaCl₂–Ca(NO₃)₂ (open symbols) mixtures as a function of the nitrate concentration. A_m values for $m_{\text{NO}_3} = 0$ are included in the figures as reported elsewhere [ALTMAYER *et al.*, 2003b]. Due to solubility limitations, nitrate concentration in the 5.24 m MgCl₂–Mg(NO₃)₂ series was kept ≤ 2.32 m.

4.3.2 Determination of total neodymium(III), concentration in solution using inductively coupled plasma mass spectrometry (ICP-MS)

Nd(III) concentration in aqueous solutions was determined by ICP-MS (X-Series II, Thermo Scientific) after 10kD (~1.5 nm) ultra-filtration (Pall Life Sciences).

Before the measurements, a dilution of the ultra-filtrated samples to a volume of 5 mL/sample was necessary. Samples were diluted with 2% HNO₃ to reduce the salt concentration of the background electrolyte (≤ 0.01 M) and to keep the neodymium concentration in the optimum range for the measurements (1–10 ppb). Dilution ratios were typically between 1:10 and 1:100'000.

Detection limit for Nd(III) is usually in the range of 10^{-9} – 10^{-10} M depending on background electrolyte concentration in the sample and required dilution steps. The analytical uncertainties of the ICP-MS analyses are 5–10%. The outcome of the solubility measurements was compared with previous solubility experiments with Nd(OH)₃(s) in pure (nitrate-free) NaCl, MgCl₂ and CaCl₂ solutions [NECK *et al.*, 2009].

4.4 Zircaloy-4 sample origin and treatment

4.4.1 Origin and irradiation characteristics of the Zircaloy-4 cladding

The studied Zircaloy-4 cladding was sampled from fuel rod segment N0204 of the fuel rod SBS1108, which was irradiated during four cycles in the PWR Gösgen (KKG, Switzerland). The fuel rod was finally discharged from the nuclear reactor in May 1989 and experienced an average burn-up of 50.4 GWd/t_{HM}. The fuel of segment N0204 and adjacent segments were made by Kraftwerk Union AG (KWU, today Areva). The UO₂ fuel pellets were manufactured using the NIKUSI short-term fast sintering process [STRATTON *et al.*, 1991]. Except two UO₂(nat.) pellets, all fuel pellets of segment N0204 were initially enriched with 3.8 wt.% of U-235. In the plenum of the fuel rod segment a stainless steel spring was inserted. Relevant characteristic parameters of the irradiated material are given in Table 4.5 as well as photos in Figure 4.3.

Actinides, fission and activation products build up during reactor operation in the Zircaloy cladding, nuclear fuel and other metal structural parts of the reactor core.

The radionuclide inventory of these materials depends on the reactor type, the chemical composition of the material, the (vertical) position of the material in the nuclear reactor and irradiation characteristics e.g. neutron flux, final burn-up, linear power rate, number of cycles and irradiation time. A detailed knowledge of the studied material as well as the adjacent material (chemical composition, position in the reactor) and its irradiation history is indispensable for accurate radionuclide inventory calculations (see section 4.7).

Table 4.5: Characteristics and irradiation data of the UO₂ fuel rod segment [Metz *et al.*, 2014].

Reactor	type: PWR fuel type: UO ₂ thermal power: 3002 MW
Zircaloy specimen data	material: Zircaloy-4 (Zry-4) rod diameter: 10.75 mm wall thickness: 0.725 mm length: 75.3 mm
Plenum spring data	material: X7CrNiAl17-7 (1.4568) weight: 10.4 g
UO₂ fuel pellet	initial enrichment: 3.8% of U-235 pellet diameter: 9.3 mm pellet height: 11 mm pellet density: 10.41 g·cm ⁻³
Irradiation data	average burn-up: 50.4 GWd/t _{HM} number of cycles: 4 average linear power rate: 260 W/cm maximal linear power rate: 340 W/cm date of discharge: 27 May 1989 irradiation duration: 1226 days



Figure 4.3: Pictures and dimension of the irradiated plenum Zircaloy-4. The upper two pictures show the whole irradiated Zircaloy-4 plenum specimen. The lower left picture shows the bottom half of the specimen, where the plenum was cut from the fuel rod segment whereas the lower right picture shows the massive Zircaloy-4 end cap of the plenum specimen.

In total 177 fuel assemblies, each with a 15×15 lattice, form the reactor core of PWR Gösgen. 205 of the 225 positions of the lattice geometry are occupied with fuel rods, the 20 remaining guide tubes are available for absorber rods (AgInCd) [KERNKRAFTWERK-GÖSGEN, 2010]. Fuel rod SBS1108 was inserted in the central region of the 15×15 fuel assembly.

The N0204 segment was stored gas tight until 2012. The segment was characterized, gas sampling (puncturing), cutting and sampling of fuel pellets, plenum cladding and the stainless steel spring was conducted. Results of the non-destructive characterization (ZrO_2 thickness determination, γ -scan along the fuel rod segment) and gas sampling are provided in reports of JRC-ITU and KIT-INE [GONZALEZ-ROBLES *et al.*, 2012; WEGEN *et al.*, 2012c; WEGEN *et al.*, 2012b, a], respectively.

4.4.2 Preparation of irradiated Zircaloy-4 plenum cladding specimens for the dissolution experiments

Preparation of Zircaloy-4 samples from the irradiated plenum tube was conducted in the KIT-INE shielded box-line by remote handling. Six subsamples were dry cut using a low speed saw (Isomet 11-1180, Buehler Ltd.) equipped with a diamond saw blade due to the high dose rate of the 75.3 mm in length plenum Zircaloy-4 cladding of ≤ 20 mSv/h. The cutting was very slow (30–40 minutes per sample) to prevent overheating of the specimens. The mass and dose rate of each specimen was measured using an analytical balance (MS304S, Mettler-Toledo International Inc.) and a dose rate meter (6150AD6, automess – Automation und Messtechnik GmbH). Details of the samples are given in Table 4.6 and photos of the sample preparation are shown in Figure 4.4. After the preparation of the samples, the surface of the Zircaloy specimens was analysed by means of an optical microscope (DigiMicro 2.0, Drahtlose Nachrichtentechnik, dnt) available inside the shielded box.

Due to the relative low dose rate (≤ 280 μ Sv/h) of each sample and in accordance with the German Radiation Protection Ordinance [BGBL, 2005] and the technical advisory board of KIT-INE, the samples were removed from the shielded box and dissolution experiments including the samples were conducted in a specifically manufactured glove box.

Materials and Methods

Table 4.6: Mass and dose rate of the irradiated Zircaloy-4 specimens.

sample	#1	#2	#3	#4	#5	#6
mass [mg]	184.4 ± 0.2	130.1 ± 0.2	119.7 ± 0.2	177.5 ± 0.2	189.0 ± 0.2	183.3 ± 0.2
dose rate [$\mu\text{Sv/h}$]	≤ 270	≤ 150	≤ 170	≤ 260	≤ 280	≤ 220

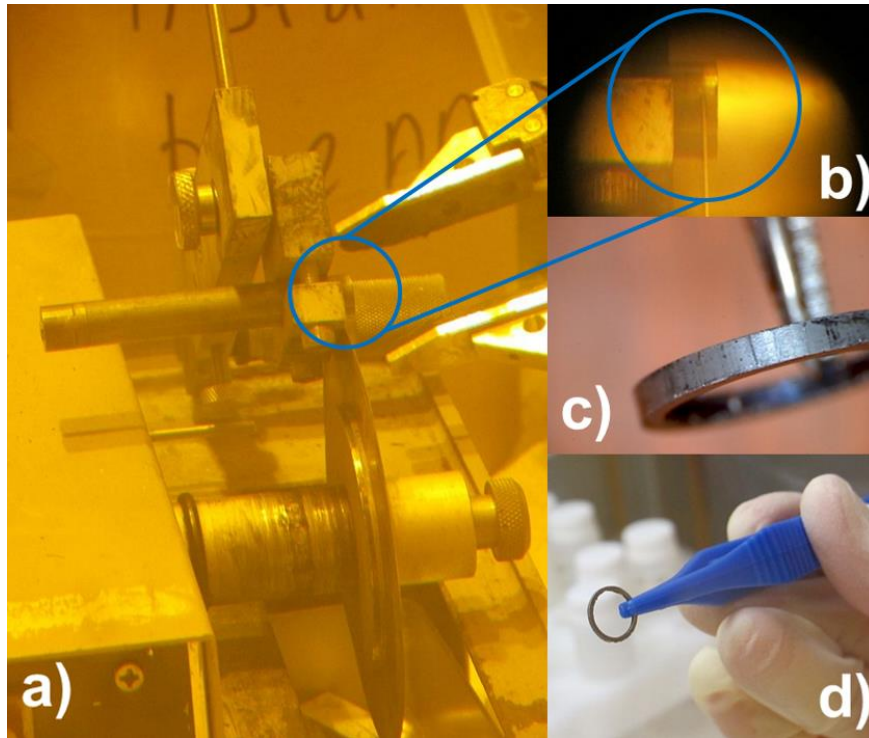


Figure 4.4: Images of the preparation of Zircaloy-4 subsamples. Photo (a) shows the low speed saw and the Zircaloy-4 plenum cutting half through a sample (photo (b)). The photo (c) was made during the optical examination using the microscope available inside the shielded box and photo (d) shows the preparation of the sample for the dissolution experiments inside a specifically manufactured glove box.

4.5 Analysis methods applied to studies with C-14 bearing samples

4.5.1 Liquid scintillation counting (LSC) for determining the carbon-14 and iron-55 concentration in solution

For determining the total C-14 and Fe-55 concentration in solutions obtained from digestion experiments performed with irradiated Zircaloy-4 (see section 4.6), liquid scintillation counting was used. LSC is a technique for determining the activity of a radioactive sample by mixing the active material with a liquid scintillator (cocktail). The radiation emitted by the radionuclide transfers energy to the solvent molecules. The excited molecules relax back to their ground states by emitting photons. A photomultiplier (a photocathode with electron multiplier) converts and multiply these light quanta into electrons which are then subsequently detected by a semiconductor detector. The detected light quanta are directly proportional to the decay energy.

LSC measurements were performed from solutions obtained from washing bottles used for C-14 separation and the digestion liquor from dissolution of Zircaloy-4 specimens (see sections 4.6.1–4.6.3) using an ultra-low level spectrometer (Quantulus 1220, Wallac Oy, PerkinElmer). Preparation of samples for the LSC measurements is summarized in Table 4.7.

Polyvials[®] (HDPE, Zinsser Analytic) were used for liquid scintillation counting. Inactive blanks containing only matrix (2M NaOH, used for absorption of C-14) and cocktail were always measured in addition and resulted in a typical background

of one to four counts per minute (cpm) for the measurements (energy window: channels 350 to 600). Detection limit for C-14 calculated from the threefold of the background was ~ 2 Bq C-14 per washing bottle. Figure 4.5 shows the quench correction curve for the C-14 sample geometry and the energy window (channels 350 to 600) used for data evaluation obtained by successive quenching of the matrix with nitromethane (0–95 μ L). Counting efficiency for C-14 was about 26% for the sample geometry and energy window used for data analysis.

Fe-55 was measured by LSC after extraction from other radionuclides in digestion liquor obtained from dissolution of irradiated Zircaloy-4 (see sections 4.6.1 and 4.6.2) by selective separation using an extraction column e.g. [GRAHEK AND ROZMARIC MACEFAT, 2006]. The energy window used for data evaluation was channels 1–200. Preparation of samples for the LSC measurements is summarized in Table 4.7. The analytical uncertainties of the LSC analyses are 5%.

[NEEB, 1997] described the quantitative release of H-3 as gaseous $^1\text{H}-^3\text{H}$ (HT) during the digestion of irradiated Zircaloy-4 cladding. H-3 significantly disturbs the C-14 quantification using LSC due to the large H-3 inventory released during digestion in contrast to the C-14 inventory and similar endpoint energies of the β -transition (H-3: 0.02 MeV vs. C-14: 0.2 MeV [MAGILL *et al.*, 2006]), which makes an effective separation of C-14 from H-3 indispensable. Although the interference of H-3 was tested using $^1\text{H}-^3\text{H}-\text{O}$ (HTO), the release of gaseous HT made an improvement of the C-14 extraction method necessary (see section 5.3.4).

I-129 also disturbs significantly the quantification of C-14 using LSC due to very similar endpoint energies of the β -transition (I-129: 0.2 MeV vs. C-14: 0.2 MeV [MAGILL *et al.*, 2006]). Therefore, recovery tests were performed using I-129 as Na^{129}I where no interference was seen (see section 5.3.1). However, in experiments performed with irradiated Zircaloy-4, I-129 was not detected in all LSC measurements (even not in the γ -spectroscopy, see section 4.5.2).

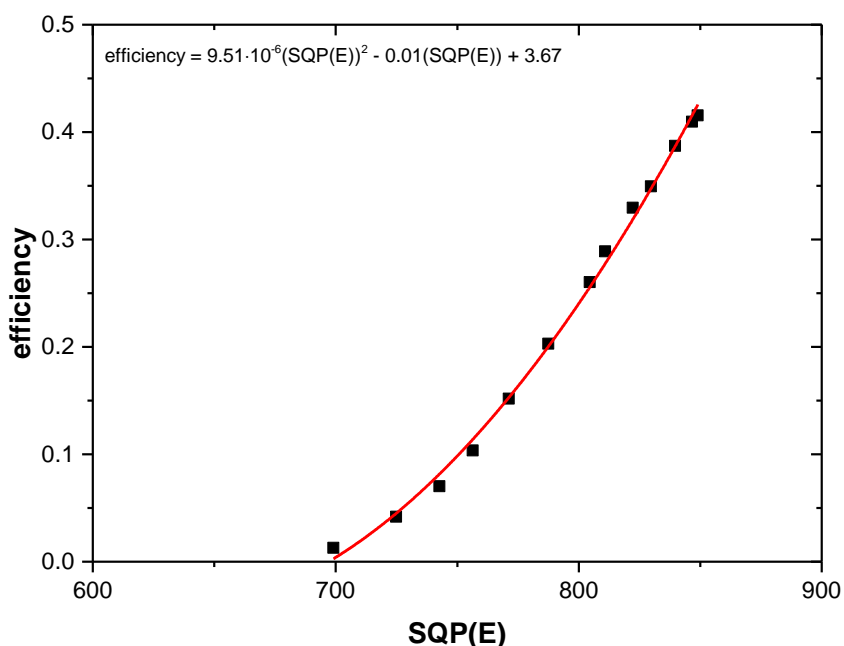


Figure 4.5: Quench correction curve for C-14 sample geometry and the energy window (channels 350–600) used for data evaluation. The counting efficiency is plotted against the spectral quench parameter of the external standard: SQP(E).

Table 4.7: Sample preparation for LSC measurements.

washing bottles (see section 4.6.3)	RN	matrix	matrix + cocktail [mL]	cocktail	measuring time [min]
#2, #5, #6	H-3	5% H ₂ SO ₄	3 + 18	Hionic Fluor™ (PerkinElmer)	3×30
#3, #4, #7, #8	C-14	2M NaOH	3 + 18	Hionic Fluor™ (PerkinElmer)	3×30
digestion liquor*	Fe-55	1.5 M HCl	1 + 10	Ultima Gold™ LLT (PerkinElmer)	1×30
#1	I-129	0.1 M AgNO ₃	2 + 10	Ultima Gold™ XR (PerkinElmer)	3×30

* Fe-55 was separated from other radionuclides in the digestion liquor by extraction column.

4.5.2 γ -spectroscopy for determining the antimony-125 and cesium-137 concentration in solution

Antimony-125 and cesium-137 were quantified in digestion liquors obtained from dissolution experiments performed with irradiated Zircaloy-4 (see sections 4.6.1 and 4.6.2) using γ -spectroscopy.

Solid-state detectors (semiconductor detectors) e.g. high purity germanium (HPGe) detectors rely on the detection of electron-hole pairs generated by γ -rays in the semiconductor material. These electrons and holes move to the respectively charged electrodes (electrons to the positive and holes to the negative contact) due to an electric field which is applied to the detector and create an electrical signal. This signal is then amplified and sent to a multichannel analyzer and on to a computer for data treatment.

γ -spectroscopy measurements in this work were performed by means of an extended range coaxial Ge detector (GX3018, Canberra Industries Inc.) with a relative efficiency of $\geq 30\%$. Energy and efficiency calibration of the detector was performed using a certified multi-nuclide standard solution (Mixed Gamma 7600, catalog number 7603 with 3% Am-241 and 30% Pb-210, 1.361 μCi , 50.36 kBq, Eckert & Ziegler Strahlen- und Medizintechnik AG). Distance above the detector (0–15 cm) as well as measurement time was depending on the activity of the sample but usually in the range of 2–4 hours. Data evaluation was performed using the Genie 2000 software (Canberra Industries Inc.)

One milliliter aliquots from the digestion liquor obtained from Zircaloy-4 specimen dissolution experiments in the flask or autoclave were measured directly or after cesium removal using APEX[®] screw-cap microcentrifuge tubes (2 mL, polypropylene, PP, Alpha Laboratories Ltd.). Cesium removal was performed by

mixing 1.5–2.0 mL of the digestion liquor with ~0.1 g ammonium molybdophosphate (AMP). Then the yellow suspension containing Cs-molybdophosphate was filtered (0.45 μm) and one milliliter of the filtrate was used for the measurements. In contrast 10 mL aliquots from all washing bottles used in the extraction procedure of C-14 (see section 4.6.3) were taken for measurements (10 mL narrow neck bottles, series 301, low-density polyethylene, LDPE, Kautex), respectively. The analytical uncertainties of the γ analyses are typically 5%.

4.5.3 Gas mass spectrometry (gas-MS)

Gaseous samples obtained from dissolution experiments of Zircaloy-4 cladding specimens in an autoclave (see section 4.6.2) were analyzed for H_2 , N_2 , O_2 , CO , CO_2 , CH_4 , Ar by means of a quadrupole gas mass spectrometer (GAM400, InProcess Instruments). The concentration of C-14 bearing compounds in the gas phase were too low for analysis. The gas-MS was equipped with a secondary electron multiplier detector and a batch inlet system, optimized for low gas consumption (see Figure 4.6). Within the gas dosage and inlet system, the total gas pressure was monitored at four successive positions. It applied three different expansion volumes to charge relatively low gas contents in the desired pressure range. Ten scans of each gas sample were measured, using the secondary electron multiplier detector and the mean value was taken. Calibration of the instrument was performed in the same pressure range as the respective range for analysis of the sample aliquots. The analytical uncertainties of the gas analyses are about 5%.



Figure 4.6: Pictures of GAM400 quadrupole gas-MS and the batch inlet system for connecting the gas collecting cylinder to the instrument.

4.6 Dissolution of irradiated Zircaloy-4 specimen

Two types of digestion experiments were conducted with the irradiated Zircaloy-4 specimens. The first approach, dissolution of Zircaloy specimens in a glass reactor, gives insight into the C-14 inventory and the partitioning between total inorganic and organic/CO C-14, whereas no information about the distribution of C-14 bearing compounds in the aqueous and gaseous phase is obtained. Therefore, dissolution of Zircaloy specimens in an autoclave were additionally performed. The partitioning of C-14 between inorganic and organic/CO compounds and their distribution between aqueous and gaseous phase is obtained by these autoclave experiments. However, the autoclave experiments are much more elaborate/costly and time-consuming.

Three cladding samples (#1 to #3) were digested in 16% H₂SO₄ + 3% HF in a flask of the C-14 extraction apparatus set-up in a specifically manufactured glove box

and two cladding sample (#4 and #6) were digested using an autoclave equipped with a glass liner and a gas collecting cylinder with two valves mounted on top. Sample #5 was digested in a glass beaker and analysed by γ -spectroscopy and LSC to check before working that the radioactive inventory of the samples is within the regulatory limits for working in a glove box.

4.6.1 Sample digestion in a glass reactor

In the experiments with samples #1, #2 and #3, the cladding specimen was placed in the flask (see Figure 4.7) connected to the C-14 extraction system after evacuating the system to 0.2 bar below atmospheric pressure and setting the nitrogen gas flow rate to 300 mL/min. 100 mL 24% H₂SO₄ was added immediately to the sample container using the dropping funnel. Then slowly 50 mL 10% HF was added through the dropping funnel to the flask and the Zircaloy-4 sample was digested within 30 minutes. As soon as the Zircaloy-4 specimen was digested successfully, the solution was purged and stirred two more hours.

The extraction of C-14 containing gases evolving during the digestion process (CO, CO₂, gaseous hydrocarbons) as well as the separation of the remaining carbon fraction (dissolved hydrocarbons e.g. alcohols, aldehydes, ketones, carboxylic acids...) in solution is described in section 4.6.3. During acid digestion, the volatility of some organic compounds (e.g. acetic and formic acids) can be increased and absorbed in the first set of alkaline washing bottles of the C-14 extraction system (see sections 4.6.3.1 and 4.6.3.2, bottles #3 and 4) resulting in an overestimation of the inorganic C-14 bearing fraction. Magnusson et al. observed up to 2.5% cross contamination of organic C-14 in the inorganic fraction in C-14 recovery tests performed with ion exchange resins [MAGNUSSON AND STENSTROEM, 2005]. In recovery tests performed in this study no significant cross contamination

Materials and Methods

of organic C-14 bearing compounds released during the acid digestion into the first set of alkaline washing bottles is observed (see section 5.3.1).

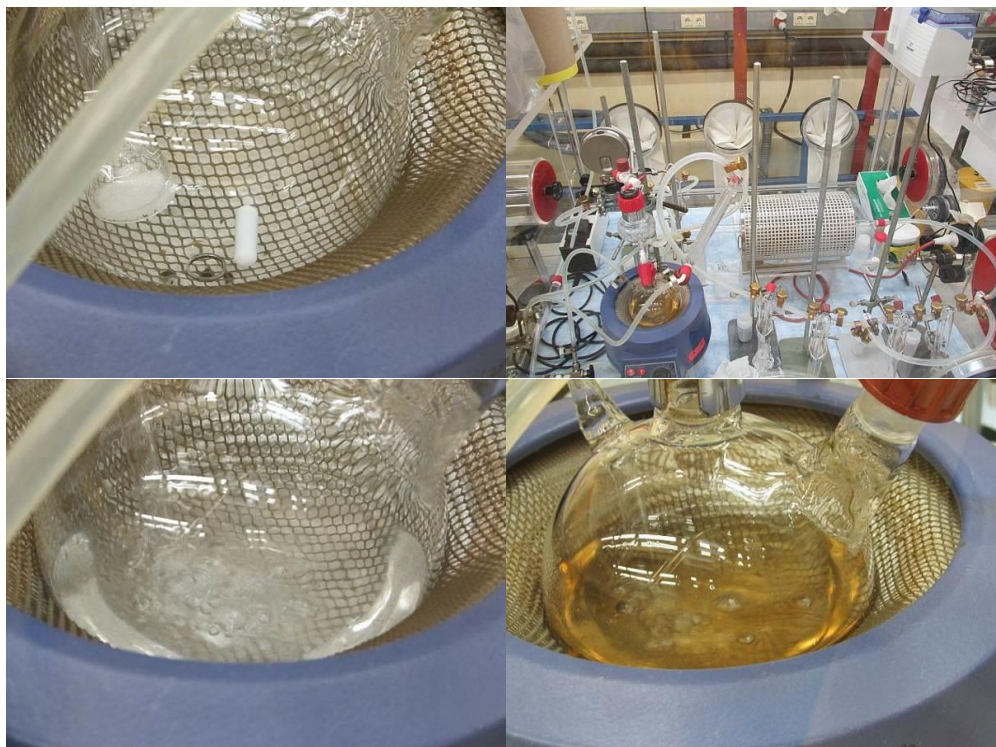


Figure 4.7: Images of the C-14 extraction and analysis system and the glass reactor. The upper pictures show the Zircaloy-4 sample inside the flask (left) and the whole C-14 extraction system including the catalytic furnace (right). The lower left pictures shows the digestion of the sample at room temperature and the lower right picture shows the wet oxidation process during which the solution turns gold/brownish before decoloring again.

4.6.2 Sample digestion in an autoclave

Samples #4 and #6 were respectively placed in an autoclave equipped with a glass liner, for the digestion (see Figure 4.8). The autoclave was sealed air tight, and an evacuated gas collecting cylinder with two valves was mounted on top of the autoclave. The autoclave was flushed with nitrogen or argon through one of the two valves in the lid of the autoclave for about 20 minutes. Then, 20 mL of a 16% H₂SO₄ + 3% HF mixture was added through a long tube inserted through the other valve in the lid of the autoclave using a syringe. After the addition, the long tube was immediately removed and all valves in the lid of the autoclave were closed. During the digestion process the autoclave developed a pressure of about 1.4 bar. After in total five hours and ensuring constant pressure, the gas collecting cylinder was opened and the gas phase collected. The final pressure (after opening the 50 mL gas collecting cylinder) in the whole system was about 0.5 bar. The gaseous phase was analyzed by gas-MS. The aqueous solution as well as the remaining gas phase in the gas collecting cylinder were also analyzed for C-14 in the C-14 extraction system described in section 4.6.3.

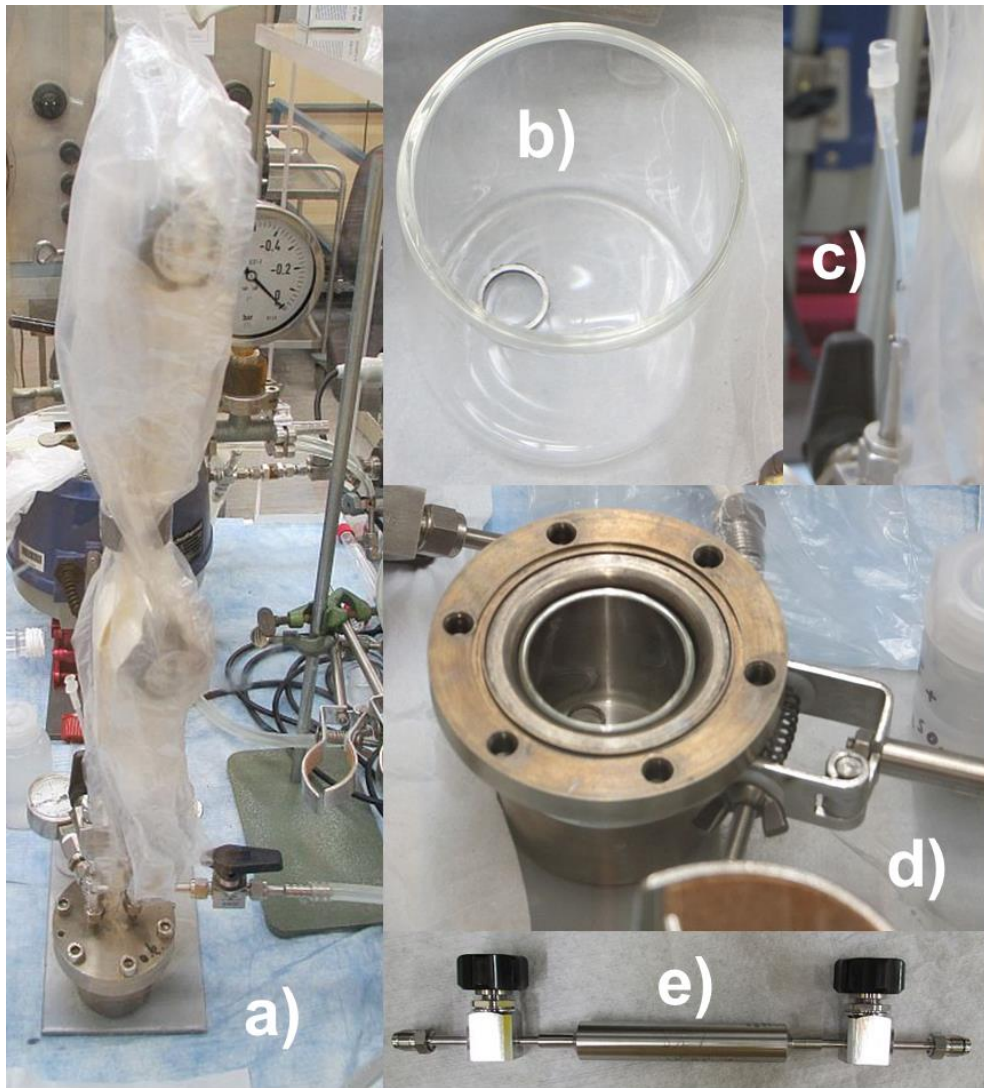


Figure 4.8: Images of the autoclave and gas collecting cylinder. Picture (a) shows the sealed autoclave with gas collecting cylinder mounted on top. The glass liner with the irradiated Zircaloy-4 sample is seen in picture (b) and the glass liner with sample inside the open autoclave in (d). Picture (c) shows the tube used for the addition of the acid. Finally the gas collecting cylinder with two valves is seen in picture (e).

4.6.3 Carbon-14 extraction and separation technique

The C-14 extraction and separation technique used in this work is based on a method developed for determining C-14 in spent ion exchange resins and process water from nuclear reactors [MAGNUSSON AND STENSTROEM, 2005; MAGNUSSON, 2007; MAGNUSSON *et al.*, 2008], and allows to determine at the same time the total inorganic and total organic C-14 content and thus the C-14 inventory. The method was adapted for highly activated materials and particularly for gaseous samples derived from dissolution experiments with irradiated Zircaloy-4 specimens using autoclaves. The total inorganic/organic C-14 analysis in aqueous and gaseous samples and simultaneous distinction of C-14 bearing inorganic/organic compounds in solution and gas phase is a novel procedure for irradiated Zircaloy-4 analysis, developed and applied in this work.

4.6.3.1 *Experimental set-up for sample digestion and C-14 extraction in a glass reactor*

The experimental design outlined in Figure 4.9 consists of a 500mL three-neck flask (glass reactor) with connections (Rodaviss, Duran) for gas-inlet, customized 120mL dropping funnel (see Figure 4.10) and cooler connected to the CO₂ extraction system.

The C-14 extraction system consists of in total eight customized washing bottles equipped with a fritted glass tip of porosity 1 (see Figure 4.10) filled with 25 mL 2M NaOH, respectively. Except bottle #1 which is the iodine-129 trap and contains 25 mL 0.1 M AgNO₃ as well as the washing bottles #2, #5 and #6 containing 25 mL

Materials and Methods

5% H₂SO₄ for trapping tritium. The washing bottles #4 and #8 are used as safety bottles.

The catalytic furnace consists of a tube furnace (MTF 12/25/250, Carbolite) operated at 750°C, holding a quartz glass tube of ~500 mm length with an outer diameter (OD) of about 25 mm. The glass tube is filled with the catalyst mixture over the length of about 200 mm. The mixture is composed of 1 wt.% platinum on alumina pellets and CuO/Cu₂O wires. The mixing ratio is about 30 wt.% Pt on Al and 70 wt.% copper oxide wires. The mixture is held in place inside the quartz glass tube by quartz glass wool.

The system is interconnected by silicon tubing (8.5 mm ID, 11.5 mm OD), with two PP/PTFE three way stopcocks (Nalgene), placed before and behind washing bottles #3 and #4. Nitrogen, supplied by a gas bottle connected through a buffer volume, is used as carrier gas. The buffer volume at atmospheric pressure is used as N₂ reservoir, fed through the gas bottle. In order to prevent the loss of any gases in the case of a leakage, the system is operated under subatmospheric pressure (0.2 bar below atmospheric pressure) by means of a diaphragm vacuum pump equipped with fine-adjustment valve and manometer (max. 16 L/min, N816.3 KT.18, KNF). Gas flow through the system is generated by means of the vacuum pump only and the flow rate (~300 mL/min) of the carrier gas through the whole apparatus is controlled by a flow meter (Model P, Aalborg Instruments & Controls). The pressure in the system is monitored by a vacuum gauge, mounted between the furnace and washing bottle #5.

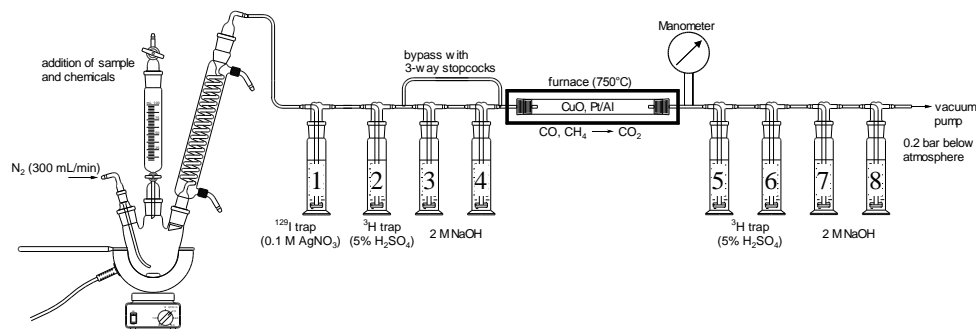


Figure 4.9: Experimental design for C-14 extraction from Zircaloy-4 digestion experiments in glass reactor or digestion liquor obtained from autoclave experiments.



Figure 4.10: Customized washing bottle (250 mm × 20 mm) equipped with a fritted glass tip of porosity 1 (upper picture) and customized dropping funnel (120 mL, lower picture).

The analytical C-14 separation procedure for the digestion of an irradiated Zircaloy-4 specimen in a glass reactor is shown in Figure 4.11. The extraction procedure involves several steps during which the inorganic (carbonates, bicarbonates) and organic (gaseous and dissolved hydrocarbons) carbon fractions are separated and converted into CO₂, which is then absorbed in various alkaline washing bottles. The method does not distinguish between C-14 bearing hydrocarbons (e.g. ¹⁴CH₄) and

Materials and Methods

carbon monoxide (^{14}CO). Both compounds are oxidized to CO_2 in the catalytic furnace and absorbed in the alkaline washing bottles behind the furnace.

In a first step, the acid digestion of a Zircaloy-4 specimen in the flask releases gaseous C-14 compounds, among others. These gaseous compounds possibly contain carbon dioxide released from carbonates during the sample dissolution as well as gaseous hydrocarbons (methane,...) or carbon monoxide (CO). The CO_2 released during digestion is absorbed in a first set of washing bottles containing 2 M NaOH (“inorganic” washing bottles, see Figure 4.9, washing bottles #3 and #4). Reduced gaseous compounds (hydrocarbons/CO) passes the “inorganic” washing bottles unaffectedly and are oxidized in a catalytic furnace to CO_2 and absorbed in a second set of washing bottles, behind the furnace, containing 2 M NaOH (“organic” washing bottles, see Figure 4.9, washing bottles #7 and #8). In a second step the remaining carbon compounds (dissolved hydrocarbons) in the acidic digestion liquor are oxidized by means of a strong oxidant potassium peroxydisulfate ($\text{K}_2\text{S}_2\text{O}_8$, KPS), a catalyst (AgNO_3), heat (95°C) and magnetic stirring to CO_2 and absorbed in the “organic” washing bottles. Prior to the wet oxidation step, washing bottles #3 and #4 are disconnected from the system using the three-way stopcocks.

Consecutively, 50 mL 5% KPS solution and 5 mL 4% AgNO_3 solution were added immediately to the sample container through the dropping funnel under simultaneous heating. During the wet oxidation process the digestion liquor turned gold/brownish due to the dissociation of KPS and formation of radicals before decoloring again (see Figure 4.7). After one hour, the same amounts of potassium peroxydisulfate and silver nitrate were added to the flask and the mixture was purged, heated and stirred for another hour. Finally, after in total four hours (including the two hours from sample digestion and purging at room temperature) samples were collected, from all washing bottles and flasks, and analyzed by γ -spectroscopy and LSC.

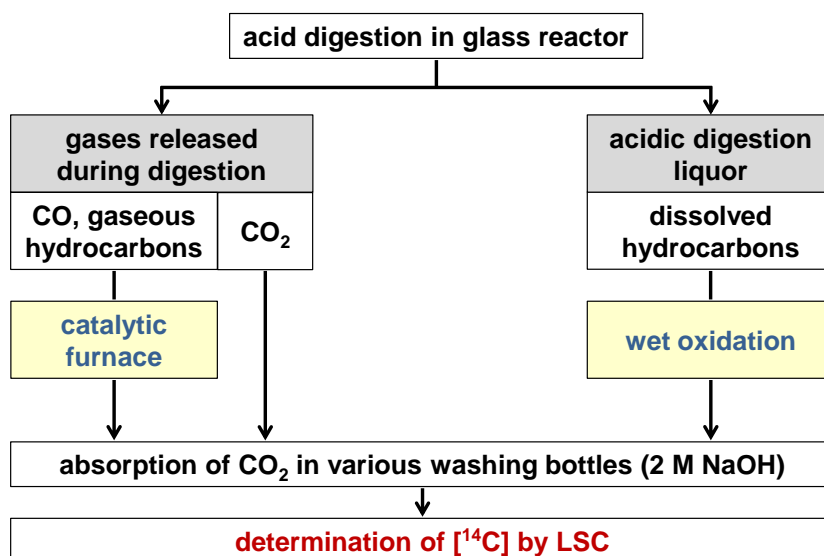


Figure 4.11: Scheme of C-14 extraction procedure for C-14 bearing compounds released during digestion experiments with Zircaloy-4 specimens in a glass reactor.

4.6.3.2 Experimental set-up and C-14 extraction from aqueous and gaseous samples derived from dissolution experiments with Zircaloy-4 performed in an autoclave

The experimental set-up for aqueous samples (digestion liquor) obtained from dissolution experiments with irradiated Zircaloy-4 in an autoclave is the very same as for the digestion experiments in the glass reactor (see Figure 4.9).

The experimental design for gaseous samples is outlined in Figure 4.12. The C-14 extraction and separation part of the experimental set-up is analogous to the apparatus described in section 4.6.3.1. Instead of a three-neck flask with gas-inlet, dropping funnel and cooler, one end of the gas collecting cylinder with two valves

Materials and Methods

(SS-4CS-TW-50, Swagelok, see Figure 4.13), containing the gaseous sample, is connected to the first washing bottle of the C-14 extraction and separation system. The other end is connected to the nitrogen gas supply via the buffer volume.

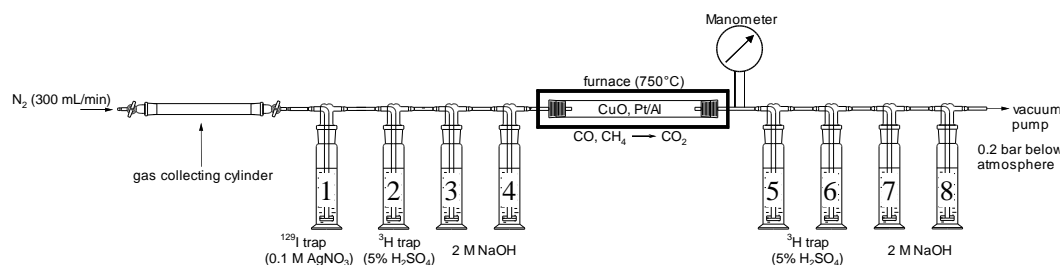


Figure 4.12: Experimental design for C-14 extraction of gaseous aliquots obtained from dissolution experiments with Zircaloy-4 specimens in an autoclave.



Figure 4.13: Double-ended gas collecting cylinder for gaseous samples derived from digestion experiments with Zircaloy-4 performed in an autoclave.

The analytical C-14 separation procedure for the digestion of irradiated Zircaloy-4 in an autoclave is outlined in Figure 4.14. The C-14 extraction procedure for digestion liquors obtained from autoclave experiments is analogous to the procedure described in section 4.6.3.1 for the sample digestion in a glass reactor. The only difference between the two procedures is a shorter purging and stirring time of the solution at room temperature (30 minutes versus two hours) prior to the wet oxidation procedure. The shorter purging time was chosen due to the fact that C-14 bearing compounds, released into the gas phase (CO, CO₂, hydrocarbons) during the specimen digestion in an autoclave, are already collected in the gas

collecting cylinder. Only dissolved hydrocarbons remain in the acidic digestion liquor, which are released as CO₂ and absorbed in alkaline washing bottles by the wet oxidation procedure as described in section 4.6.3.1.

First, a small fraction of the gaseous sample, collected in a gas collecting cylinder, is analysed by means of a gas-MS (see section 4.5.3). Then, the gas collecting cylinder is connected to the C-14 extraction and separation system as described above. Afterwards, the content of the gas collecting cylinder is flushed into the extraction apparatus, where CO₂ is absorbed in the washing bottles #3 and #4 (see Figure 4.12). Other gaseous carbon compounds (CO, hydrocarbons) are oxidized to CO₂ in a catalytic furnace, after passing the first four washing bottles unaffectedly, and are absorbed in the washing bottles #7 and #8 (see Figure 4.12).

After connecting the gas collecting cylinder to the nitrogen gas supply and the extraction system, the slight vacuum in the gas collecting cylinder (about 0.5 bar) was balanced by addition of nitrogen gas. The pressure in the C-14 extraction system was lowered to about 0.2 bar below atmospheric pressure by means of a vacuum pump, and the valve of the gas collecting cylinder next to washing bottle #1 was opened. The other valve of the gas collecting cylinder was subsequently opened and the nitrogen carrier gas flow rate was set to about 300 mL/min. Finally, after in total five hours samples were collected, from all washing bottles as well as flasks (C-14 extraction from digestion liquor obtained from autoclave experiments), and analyzed by γ -spectroscopy and LSC.

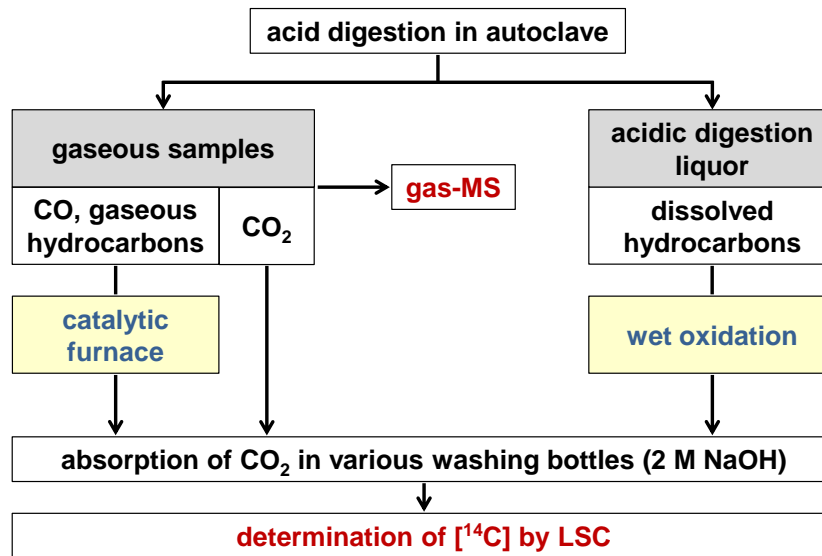


Figure 4.14: Scheme of C-14 extraction procedure from gaseous and dissolved samples derived from dissolution experiments with Zircaloy-4 specimens using an autoclave.

4.7 Activation calculation and model for the prediction of the radionuclide inventory of the irradiated Zircaloy-4

The activation of the Zircaloy-4 plenum cladding was calculated by means of the Monte Carlo N-particle code (version MCNP-X) with its burn-up and activation module CINDER [MCNP, 2011]. The nuclear data library that was used was the ENDF/B-VII database [ENDF/B-VII, 2011]. The simulation is based on a fuel subassembly of the PWR Gösgen core in which the experimental fuel rod segment SBS1108–N0204 was inserted (section 4.4.1). The calculations are performed by means of the MCNP-X transport code which evaluates the neutron flux of the subassembly. The input to the program includes beyond the geometrical shape and

the material composition, the irradiation time, the burn-up level and the linear power rate to which the subassembly was exposed to. The obtained zone (material) and energy dependent fluxes are forwarded to the sub program CINDER within MCNP-X allowing for enhanced accuracy of the reaction rates evaluations upon which the activity of the relevant nuclides is determined. The properties of the plenum Zircaloy-4 (mass, density, dimension and stainless steel spring inside, see Figure 4.15) were accounted for in such a way that it will include as much as possible all heterogeneity effects around the fuel rod segment. Thereby, the local neutron flux within the plenum could be simulated more accurately.

It is important to note that the exact composition of the Zircaloy-4 cladding components used in the fuel rod segment about 25 years ago was not available. Only limited information on the Zircaloy-4 cladding irradiated in the commercial PWR is provided by the utility and manufacturer, which is in agreement with data of a publication related to the irradiation of adjacent test fuel rods [STRATTON *et al.*, 1991]. Hence, nominal chemical composition data (see Table 4.8) were used for simulation of the neutron flux and consequently for the activation calculation. Normative specifications usually indicate a range of composition (for alloying elements) or maximum values (for impurities). Especially, the content of the C-14 precursor elements N-14, O-17 and C-13 are important for the C-14 inventory. The use of those maximum levels in activation calculations gives excessive values for C-14 and other activation/fission products in the material. [SAKURAGI *et al.*, 2013; GRAS, 2014] recommend 40ppm nitrogen impurity for Zircaloy-4 for C-14 activation calculations. This value is 25% below the initial nitrogen content in the irradiated Zircaloy-4, which was derived from information of the manufacturer of the fuel rods.

Materials and Methods

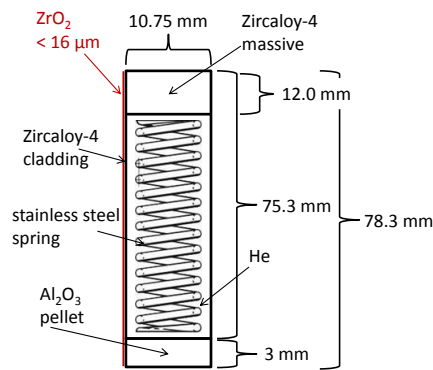


Figure 4.15: Model and dimensions of the Zircaloy-4 plenum including stainless steel spring used for calculation.

Table 4.8: Nominal composition of Zircaloy-4 and values used for calculation.

	Zircaloy-4 [wt.%] [RUDLING <i>et al.</i> , 2007]	Zircaloy-4 [wt.%] [NEEB, 1997; BAILLY <i>et al.</i> , 1999]	Zircaloy-4 used for calculation [wt.%]
Alloying elements			
Zr	balanced	balanced	balanced
Sn	1.20–1.70	1.20–1.70	0.8*
Fe	0.18–0.24	0.18–0.24	0.24
Cr	0.07–0.13	0.07–0.13	0.13
O	0.09–0.16	0.11–0.14	0.16
Si	0.005–0.012	< 0.012	
Impurities			
Al	< 0.0075	< 0.0075	
B	< 0.00005	< 0.00005	
Cd	< 0.00005	< 0.00005	
C	< 0.0270	< 0.0270	0.012
Co	< 0.0020	< 0.0020	0.002
Cu	< 0.0050	< 0.0050	
Hf	< 0.0100	< 0.0100	
H	< 0.0025	< 0.0025	
Mg	< 0.0020	< 0.0020	
Mn	< 0.0050	< 0.0050	0.005
Mo	< 0.0050	< 0.0050	
Ni	< 0.0070	< 0.0070	0.007
N	< 0.0080	< 0.0065	0.005
Ti	< 0.0050	< 0.0050	
U	< 0.00035	< 0.00035	0.00035
W	< 0.01	< 0.01	

* considered as Zircaloy-4 DX ELS 0.8: A duplex (DX) cladding which consists of an Extra-Low Sn (0.8 wt.%, ELS 0.8) outer corrosion resistant layer with a thickness < 100 μm and the rest of the thickness is Zircaloy-4 to provide the mechanical strength [RUDLING *et al.*, 2007].

4.8 Spectroscopic techniques and solid phase characterization

4.8.1 Cm(III)–TRLFS

Time-resolved laser fluorescence spectroscopy (TRLFS) allows to determine aqueous speciation and complex formation at trace concentration levels of actinide and lanthanide fluorophores such as U(VI) [RABINOWITSCH AND BELFORD, 1964], Am(III) [BEITZ *et al.*, 1989], Cm(III) [NUGENT *et al.*, 1969], Bk(III) [CARNALL *et al.*, 1984], Cf(III) [BEITZ *et al.*, 1983], Ce(III) [DECAMBOX *et al.*, 1989], Sm(III) [YAMADA *et al.*, 1982; DECAMBOX *et al.*, 1989], Eu(III) [WINSTON *et al.*, 1963; MARCANTONATOS *et al.*, 1981; SINHA AND FRESENIUS, 1982] and Gd(III) [CARNALL, 1976], among others.

Usually, the excitation of the ground state Z of Cm(III) with a half-filled $5f^7$ configuration leads to a transition to the F, G and H levels (see Figure 4.16). After the excitation, a non-radiative relaxation from these energy levels to the A state occurs. Fluorescence emission is only observed from the A to the Z state at room temperature and shows a relatively broad emission band with its maximum at $\lambda = 593.8$ nm for the aqueous Cm(III) ion [WIMMER AND KIM, 1992; FANGHÄNEL AND KIM, 1998].

In general, an inner-sphere complexation of Cm(III) with inorganic ligands shifts the emission spectrum to the red (longer wavelength) relative to the emission spectrum of the aqueous Cm(III) ion. The magnitude of the red shift depends on the ligand strength and/or the number of coordinating ligands [WIMMER AND KIM, 1992; FANGHÄNEL AND KIM, 1998].

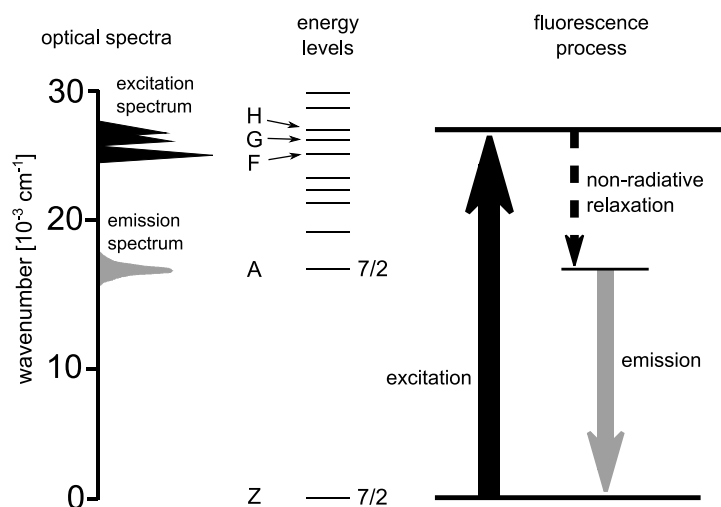


Figure 4.16: Simple term scheme of Cm(III) and its spectroscopic characteristics [FANGHÄNEL AND KIM, 1998].

4.8.1.1 *Experimental set-up of the laser system used in this work*

TRLFS measurements were performed using a Nd:YAG laser (Surelite II Laser, Continuum) pumping a dye laser (Narrowscan Dye Laser, Radiant Dyes). The repetition rate of the Nd:YAG laser was 10 Hz, with a maximum laser energy of 2 mJ. To filter out Rayleigh- and Raman-scattering, as well as short-lived background fluorescence, the emission spectra were recorded in a range of 570–630 nm with a delay of 1 μ s and in a time window of 1 ms. Emission spectra of each sample were integrated over 500 accumulations. Excitation of Cm(III) was performed at $\lambda_{\text{ex}} = 396.6$ nm, which corresponds to the maximum spectral absorbance band of Cm³⁺ aquo ion. The fluorescence emission was detected by a spectrograph (Shamrock A-SR-303i-B, Andor Technology) with a 300, 600 and 1200 lines/mm grating and an ICCD camera (iStar ICCD, Andor Technology).

4.8.1.2 Data evaluation

TRLFS spectra can be interpreted qualitatively by peak position and shape. For a quantitative interpretation, a peak deconvolution and knowledge of the respective pure component spectra is necessary. Single components were extracted by subtracting known pure component spectra from experimentally determined spectra in $\text{MgCl}_2\text{-Mg(NO}_3)_2$ systems using the OriginPro software (OriginLab Corporation).

4.8.1.3 Preparation of Cm(III) time-resolved laser fluorescence spectroscopy (TRLFS) samples

Except for the TRLFS measurement itself, the sample preparation and titration of the $\text{MgCl}_2\text{-Mg(NO}_3)_2$ samples was conducted in a glove box under argon atmosphere and exclusion of CO_2 . Cm(III)-TRLFS measurements were performed with 1×10^{-7} M Cm(III) per sample in gas tight quartz glass cuvettes with characteristic samples from the NaCl-NaNO_3 , $\text{MgCl}_2\text{-Mg(NO}_3)_2$ and $\text{CaCl}_2\text{-Ca(NO}_3)_2$ systems (see Table 4.9). Samples in NaCl-NaNO_3 and $\text{CaCl}_2\text{-Ca(NO}_3)_2$ were buffered with TRIS or CHES and the pH_m was adjusted using HCl or NaOH before the addition of Cm(III). The pH_m in both $\text{MgCl}_2\text{-Mg(NO}_3)_2$ series was buffered to pH_{max} with brucite and Mg-oxychloride, respectively. These solid phases were removed before the addition of Cm(III) by centrifugation. Samples at $\text{pH}_m = 1.00$ in the $\text{MgCl}_2\text{-Mg(NO}_3)_2$ systems were prepared with 0.1 M HCl (of same ionic strength and composition). In addition, samples in concentrated $\text{MgCl}_2\text{-Mg(NO}_3)_2$ were further titrated to $\text{pH}_m = 2.94/2.95$ using the background electrolyte prepared for the $\text{pH}_m = 1.00$ samples containing 0.1 M HCl (of same ionic strength

and composition). A total of 18 samples were prepared for the Cm(III)–TRLFS measurements.

Table 4.9: Summary of the samples prepared for the Cm(III)–TRLFS measurements.

sample*	m_{Cl^-}	$m_{\text{NO}_3^-}$	pH _m
NaCl–NaNO₃			
5.61/0.00	5.61	0.00	7.95, 8.95
0.00/6.02	0.00	6.02	7.93, 8.93
MgCl₂–Mg(NO₃)₂			
0.25/0.00	0.50	0.00	8.95
0.15/0.10	0.30	0.20	8.95
4.05/0.00	8.10	0.00	1.00, 2.95–8.95
3.77/0.29	7.54	0.58	1.00, 2.95–8.95
2.91/1.16	5.82	2.32	1.00, 2.94–8.85
1.16/2.90	2.32	5.80	2.94–8.54
0.00/4.02	0.00	8.04	2.94–8.44
CaCl₂–Ca(NO₃)₂			
1.15/2.87	2.30	5.74	7.93, 8.13, 8.43, 8.63

* $m_{\text{NaCl}}/m_{\text{NaNO}_3}$ or $m_{\text{MCl}_2}/m_{\text{M(NO}_3)_2}$ with $\text{M} = \text{Mg}^{2+}$ or Ca^{2+}

4.8.2 X-ray absorption spectroscopy (XAS)

XAS is based on the excitation of core electrons of a given element. At absorption edges, core electrons are promoted to states near the continuum level (X-ray absorption near edge spectroscopy, XANES) and beyond (extended X-ray absorption fine structure, EXAFS). From these measurements, information about the oxidation state and coordination geometry (XANES) are obtained. EXAFS analysis yields interatomic distances (up to $\sim 6 \text{ \AA}$) within an uncertainty of $\pm 0.02 \text{ \AA}$, as well as the number (within $\sim 20\%$) and type ($Z \pm 1$) of the nearest neighboring atoms.

Nd-L_{III} edge (6.208 keV) X-ray absorption fine structure (XAFS) spectra were recorded at the INE Beamline for Actinide and Radionuclide Science at Angströmquelle Karlsruhe (ANKA) [ROTHE *et al.*, 2012]. Measurements and data interpretation were performed together with the respective beamline scientists.

4.8.2.1 XAFS measurements

Spectra were energy calibrated to the first inflection point in the XANES spectra of a Mn metal foil (6.539 keV), which was measured simultaneously. The XAFS signal was recorded at room temperature in fluorescence mode using a vortex Si-drift detector. Si<111> crystals were used in the double crystal monochromator, operating in fixed-exit mode. The parallel alignment of the crystal faces was detuned to ~70% of the maximum beam intensity at the beginning of each scan. The incident intensity was then held constant by means of a piezo-driven feedback system to the second crystal.

4.8.2.2 EXAFS data evaluation

EXAFS fits were performed with D-Artemis, a program of the Demeter IFEFFIT package [RAVEL AND NEWVILLE, 2005], using phase and amplitude data calculated for a 59 atom cluster (~5.8 Å diameter sized centered on the individual metal cations). FEFF6L delivered as standard with the package was replaced by FEFF8.4 for these calculations. For magnesium atoms, single path scattering files for phase and amplitude were used. The k -range used in the modelling was [2.45–9.6 Å⁻¹]. Fits were performed in the R-space [1.25–4.5 Å] using simultaneously the k^1 -, k^2 -

and k^3 -weighted data. The model structures used to fit to the data are $\text{Nd}(\text{OH})_2\text{NO}_3$ [ICSD 63550] [MULLICA *et al.*, 1986] and $\text{Nd}(\text{NO}_3)_3(\text{H}_2\text{O})_4(\text{H}_2\text{O})_2$ [ICSD 37181] [ROGERS *et al.*, 1983].

4.8.2.3 Sample preparation for XAS

EXAFS measurements were conducted on the supernatant of a solubility experiment sample in 4.05 m MgCl_2 - $\text{Mg}(\text{NO}_3)_2$. The sample was characterized by $m_{\text{NO}_3^-} = 5.81$ m, $\text{pH}_m = 8.15$ and $m_{\text{Nd(III)}} = 1.49 \times 10^{-3}$ m, EXAFS spectra were collected after 10 kD (~1.5 nm) ultrafiltration to avoid the contribution of colloidal species in the EXAFS spectra. The sample was prepared in an argon glove box in a 400 μL polyethylene vial, mounted in a gas tight cell equipped with a Kapton[®] film (polyimide, DuPont) window and transported to the beamline. The sample was measured within few hours after the sample preparation under continuous argon gas flow.

4.8.3 X-ray diffraction (XRD)

Solid phases recovered from batch solubility experiments performed with $\text{Nd}(\text{OH})_3(\text{s})$ and/or $\text{Nd}(\text{OH})_2\text{Cl}(\text{s})$ were characterized using XRD after ensuring equilibrium conditions (constant pH and $m_{\text{Nd(III)}}$).

About 2 mg of Nd(III) solid phases, recovered from selected batch solubility experiments by centrifugation, were washed four times with 0.5 mL ethanol to remove the background electrolyte, which can interfere in the XRD analysis,

resuspended in approximately 20 μL ethanol and placed on a single crystal silicon waver for collecting the XRD diffractogram after drying.

XRD measurements were performed using a D8 Advance X-ray powder diffractometer (Bruker AXS) equipped with a Cu radiation tube, Ni filter and a Sol-X detector, working at an X-ray source current of 25 mA and a voltage of 40 kV. Diffractograms were recorded in the range $5^\circ \leq 2\Theta \leq 60^\circ$ with a step size of 0.04° 2Θ , 6 seconds counting time per step and variable slit widths. Measured reflexes were compared to XRD patterns of relevant phases of the JCPDS database [JCPDS, 2001].

4.8.4 Scanning electron microscopy – energy dispersive X-ray spectroscopy (SEM-EDS)

SEM-EDS was used to assess the chemical composition and morphology of Nd(III) solid phases, recovered from batch solubility experiments, in addition to XRD. About 1–2 mg of the already washed Nd-powder from XRD solid phase characterization was used for SEM-EDS analysis.

Further, the zirconium oxide layer (ZrO_2 , see Figure 4.17) was recovered from a digestion experiment performed with irradiated Zircaloy-4 (sample #5, see Table 4.6) in a dilute $\text{HF}/\text{H}_2\text{SO}_4$ mixture. The experiment was performed without stirring, purging and heating, and the ZrO_2 stayed intact, whereas the base metal was digested.

SEM-EDS measurements were performed to analysis the chemical composition of the oxide layer. Before the measurements a fragment of the ZrO_2 was rinsed 3 times with ultrapure water (MilliQ[®]) for cleaning.

Materials and Methods

The Nd-powder samples and the irradiated ZrO_2 fragment were both fixed on sample holders using double faced adhesive carbon tape for the SEM-EDS measurements.

SEM-EDS analyses were carried out using a Quanta 650 FEG instrument (FEI) equipped with a Thermo Scientific UltraDry silicon drift X-ray detector. SEM images were collected at an electron acceleration voltage of 20 kV, whereas SEM-EDS measurements were done at 30 kV. Data analysis was performed using the NORAN System 7 X-ray microanalysis system for the Quanta 650 FEG instrument.

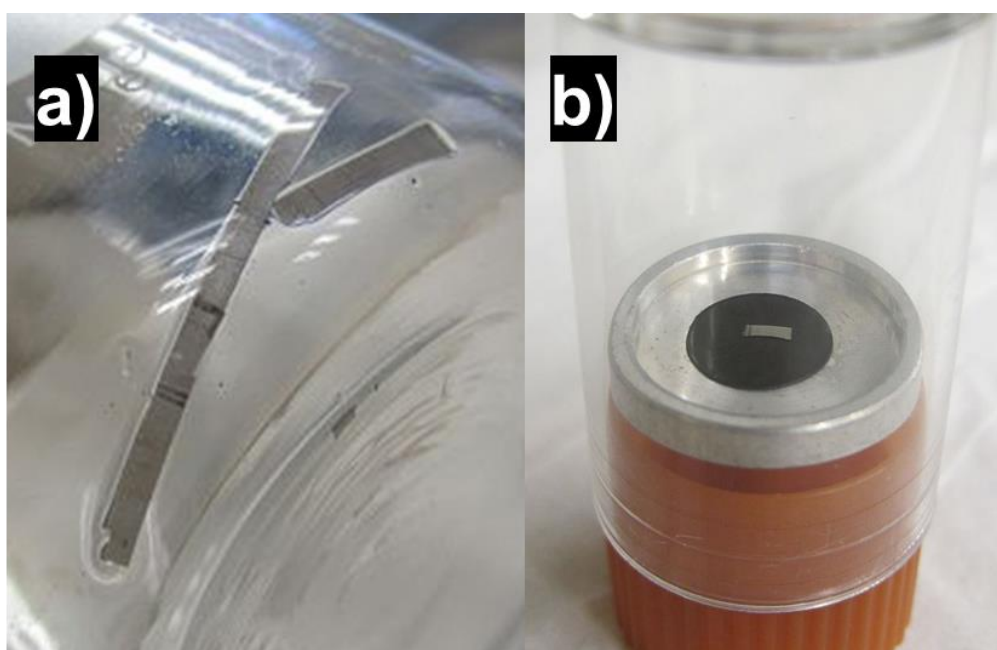


Figure 4.17: Zircaloy-4 oxide layer and ZrO_2 fragment prepared for SEM-EDS. The picture on the left (a) shows the remaining oxide layer after the digestion of the irradiated Zircaloy-4 cladding specimen, and the picture on the right (b) shows the oxide layer fragment prepared for the SEM-EDS measurements.

5 Results and Discussion

5.1 Solubility and spectroscopic study of trivalent actinides and lanthanides in dilute to concentrated Na–Mg–Ca–Cl–NO₃ mixtures¹

The complexation of An^{III}/Ln^{III} with nitrate was investigated in dilute to concentrated Na–Mg–Ca–Cl–NO₃ solutions at $2.94 \leq \text{pH}_m \leq 13.2$ and $T = 22 \pm 2^\circ\text{C}$. The last update book released within the Organization for Economic Co-operation and Development (OECD) NEA-TDB project [GUILLAUMONT *et al.*, 2003] selected only thermodynamic data for the complex AmNO₃²⁺, whereas no selection was provided for the system Pu(III)–NO₃. Recent Cm(III)–TRLFS studies with nitrate concentrations up to 4.61 m proposed the formation of CmNO₃²⁺ and Cm(NO₃)₂⁺ complexes and provided both $\lg \beta^\circ$ and $\Delta_r H^\circ$ data [SKERENCAK *et al.*, 2009; RAO AND TIAN, 2011]. So far, all these studies focused on acidic conditions, leaving

¹ This part of the present Ph.D. thesis was published in the IUPAC journal *Pure and Applied Chemistry* [HERM *et al.*, 2015].

aside the assessment of nitrate effects under neutral to alkaline, repository relevant pH conditions.

The interaction of nitrate with metal cations is considered to be weak, but slightly stronger than in the corresponding chloride systems [HUMMEL, 2001; HUMMEL *et al.*, 2005; ALTMAIER *et al.*, 2013]. A challenge in the modelling of these systems arises from the distinction between formation of (weak) complexes and variations in the activity coefficients caused by the partial exchange of the background electrolyte NaCl/MgCl₂/CaCl₂ by NaNO₃/Mg(NO₃)₂/Ca(NO₃)₂ (see section 2.4.3) [HUMMEL *et al.*, 2005; GRENTHE *et al.*, 2013].

For this purpose, extensive batch solubility experiments were conducted with Nd(III) in dilute to concentrated NaCl–NaNO₃, MgCl₂–Mg(NO₃)₂ and CaCl₂–Ca(NO₃)₂ mixed solutions. Complementary, spectroscopic measurements (Cm(III)–TRLFS, Nd–L_{III} EXAFS) and a detailed solid phase characterization (XRD, SEM-EDS) were performed to gain detailed insights into the aqueous speciation and solid phases prevailing in the studied systems. The combination of these approaches allows the development of chemical, thermodynamic and Pitzer activity models for the system Nd³⁺/Cm³⁺–H⁺–Mg²⁺–OH[–]–Cl[–]–NO₃[–]–H₂O. Considering the widely accepted chemical analogy between Nd^{III}/Cm^{III}/Am^{III}/Pu^{III}, this study provides the basis for an accurate assessment of the behavior of trivalent actinides in nitrate-rich wastes under repository-relevant conditions.

5.1.1 Solubility of $\text{Nd}(\text{OH})_3(\text{s})$ in dilute to concentrated NaCl – NaNO_3 , MgCl_2 – $\text{Mg}(\text{NO}_3)_2$ and CaCl_2 – $\text{Ca}(\text{NO}_3)_2$ mixtures

Figure 5.1 shows the experimental solubility data of $\text{Nd}(\text{OH})_3(\text{s})$ in selected NaCl – NaNO_3 mixtures with $I_m = 0.10, 0.51, 1.02, 2.64$ and 5.61 m (for all data see appendix, Table A.1). Figure 5.2 shows exemplarily the experimental solubility data of $\text{Nd}(\text{OH})_3(\text{s})$ obtained in $2.80\text{m}/4.05\text{m}$ MgCl_2 – $\text{Mg}(\text{NO}_3)_2$ mixtures with $1.1\text{ m} \leq m_{\text{NO}_3^-} \leq 5.8\text{ m}$ and 4.02 m CaCl_2 – $\text{Ca}(\text{NO}_3)_2$ mixtures with $m_{\text{NO}_3^-} = 5.75\text{ m}$. Solubility data in 0.25 and 1.04 m MgCl_2 – $\text{Mg}(\text{NO}_3)_2$, as well as data in 2.80 and 4.05 m MgCl_2 – $\text{Mg}(\text{NO}_3)_2$ with $m_{\text{NO}_3^-} < 1.1\text{ m}$ are provided in Figure A.1 in the appendix. Figure 5.1 and Figure 5.2 also show the experimental solubility data reported by Neck et al. [NECK *et al.*, 2009] in nitrate-free NaCl , MgCl_2 and CaCl_2 solutions under analogous pH and ionic strength conditions (except for the system 1.02 m NaCl – NaNO_3 , which is compared to 0.51 m NaCl reference data). Solubility curves of $\text{Nd}(\text{OH})_3(\text{s})$ calculated with the thermodynamic and activity models reported by the same authors are also appended in the figures for comparison purposes.

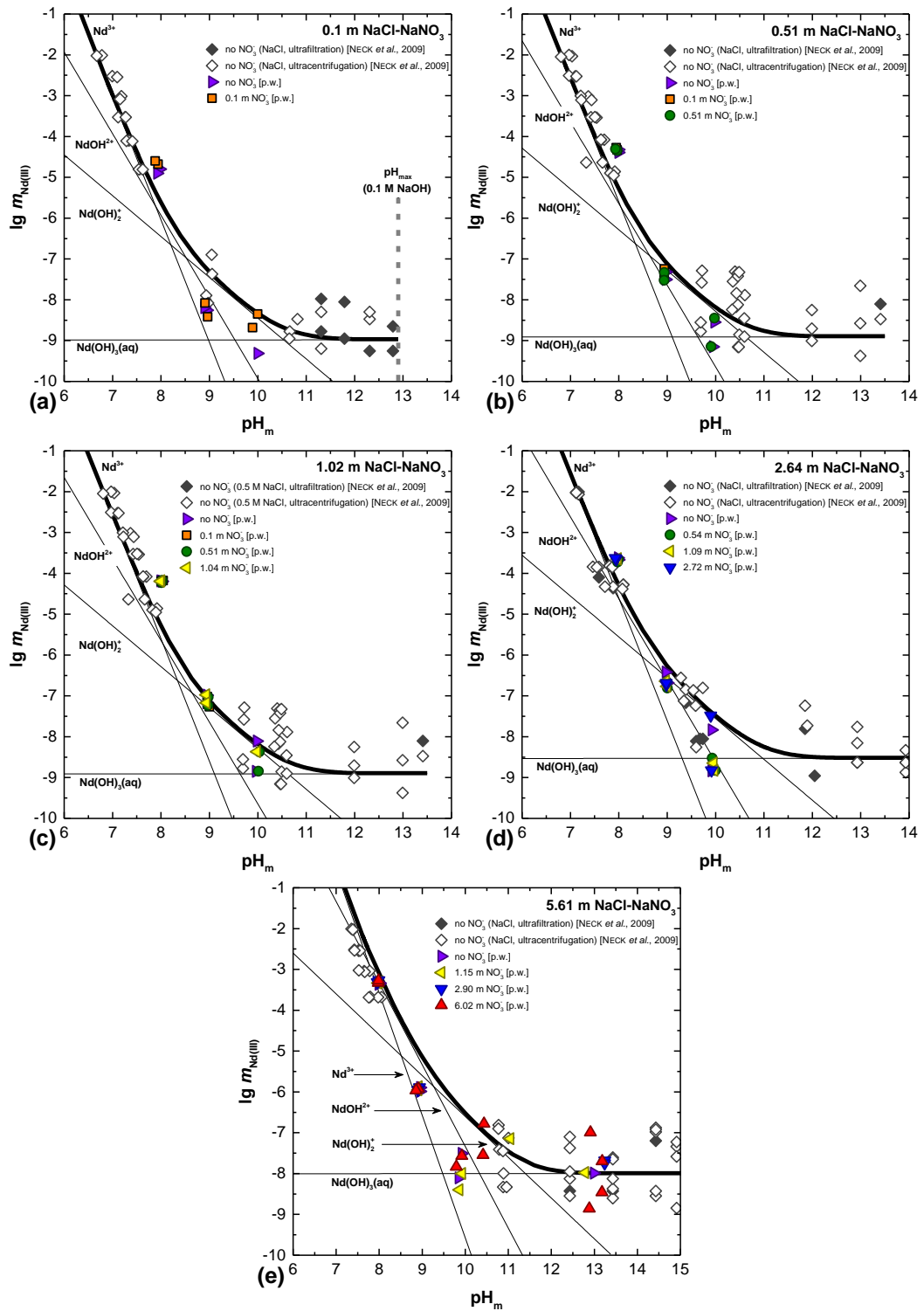


Figure 5.1: Solubility of $\text{Nd}(\text{OH})_3(\text{s})$ in 0.1–6.02 m NaCl-NaNO_3 solutions. Reference data in nitrate-free solutions [NECK *et al.*, 2009] are included in all the figures for comparison. Thick solid lines correspond to the $\text{Nd}(\text{III})$ solubility calculated using thermodynamic and activity models reported in [NECK *et al.*, 2009] for pure NaCl systems. Thin lines show $\text{Nd}(\text{III})$ aqueous speciation underlying the $\text{Nd}(\text{OH})_3(\text{s})$ solubility curve in the same background electrolyte.

No significant effect of nitrate on the solubility of $\text{Nd}(\text{OH})_3(\text{s})$ is observed for any of the studied NaCl – NaNO_3 systems. On the contrary, these solubility data show a very good agreement with $\text{Nd}(\text{III})$ solubility previously reported in nitrate-free NaCl solutions of analogous pH and ionic strength [NECK *et al.*, 2009], clearly indicating that no relevant $\text{Nd}(\text{III})$ – NO_3 complexation takes place in Na –systems within $7.5 \leq \text{pH}_m \leq 13.2$.

Nitrate has a negligible effect on the solubility of $\text{Nd}(\text{III})$ for the systems 0.25 and 1.04 m MgCl_2 – $\text{Mg}(\text{NO}_3)_2$ with nitrate concentrations up to 2.14 m (see appendix, Table A.2). These data are in good agreement with the previously reported $\text{Nd}(\text{OH})_3(\text{s})$ solubility in nitrate-free MgCl_2 solutions of analogous pH and ionic strength [NECK *et al.*, 2009]. However, a clear increase in $\text{Nd}(\text{III})$ solubility occurs for 2.80 m and 4.05 m MgCl_2 – $\text{Mg}(\text{NO}_3)_2$ mixtures and $\text{pH}_m = 8$ –9 (Figure 5.2 a–f) compared to the nitrate-free reference data by Neck and co-workers [NECK *et al.*, 2009]. The increase in solubility becomes more pronounced with increasing nitrate concentration and/or ionic strength. The maximum increase in $\text{Nd}(\text{OH})_3(\text{s})$ solubility (about one order of magnitude) is observed in the 4.05 m MgCl_2 – $\text{Mg}(\text{NO}_3)_2$ mixture with $m_{\text{NO}_3^-} = 5.81$ m (Figure 5.2 f).

The influence of nitrate complexation on the $\text{Nd}(\text{OH})_3(\text{s})$ solubility can be shown by comparing experimentally determined $m_{\text{Nd}(\text{III})}$ in equilibrium with the solid phase at $\text{pH}_m = 8.80$ in 4.05 m MgCl_2 – $\text{Mg}(\text{NO}_3)_2$ (Figure 5.3). Hence, the figure shows a clear and systematic trend to higher $\text{Nd}(\text{III})$ solubility with increasing nitrate concentration, e.g. $m_{\text{Nd}(\text{III})} = -4.49$ m at $m_{\text{NO}_3^-} = 0.24$ m, $m_{\text{Nd}(\text{III})} = -4.14$ m at $m_{\text{NO}_3^-} = 0.58$ m, $m_{\text{Nd}(\text{III})} = -3.93$ m at $m_{\text{NO}_3^-} = 1.16$ m, $m_{\text{Nd}(\text{III})} = -3.72$ m at $m_{\text{NO}_3^-} = 2.33$ m and $m_{\text{Nd}(\text{III})} = -3.50$ m at $m_{\text{NO}_3^-} = 5.81$ m (Figure 5.3). These findings hint to the likely formation of $\text{Nd}(\text{III})$ – NO_3 complexes under near-neutral to weakly alkaline pH conditions.

The slope analysis of the experimental solubility data in MgCl_2 – $\text{Mg}(\text{NO}_3)_2$ mixtures shows two well-defined pH regions with slope -2 ($\text{pH}_m \leq 8.3$) and -1

Results and Discussion

($\text{pH}_m > 8.3$). This indicates the uptake of 2 and 1 H^+ , respectively, in the chemical reaction controlling the solubility of Nd(III) in these pH regions. Based upon a system with solubility controlled by $\text{Nd}(\text{OH})_3(\text{s})$ (see next section), the formation of the aqueous species with stoichiometries Nd:OH 1:1 and 1:2 is proposed.

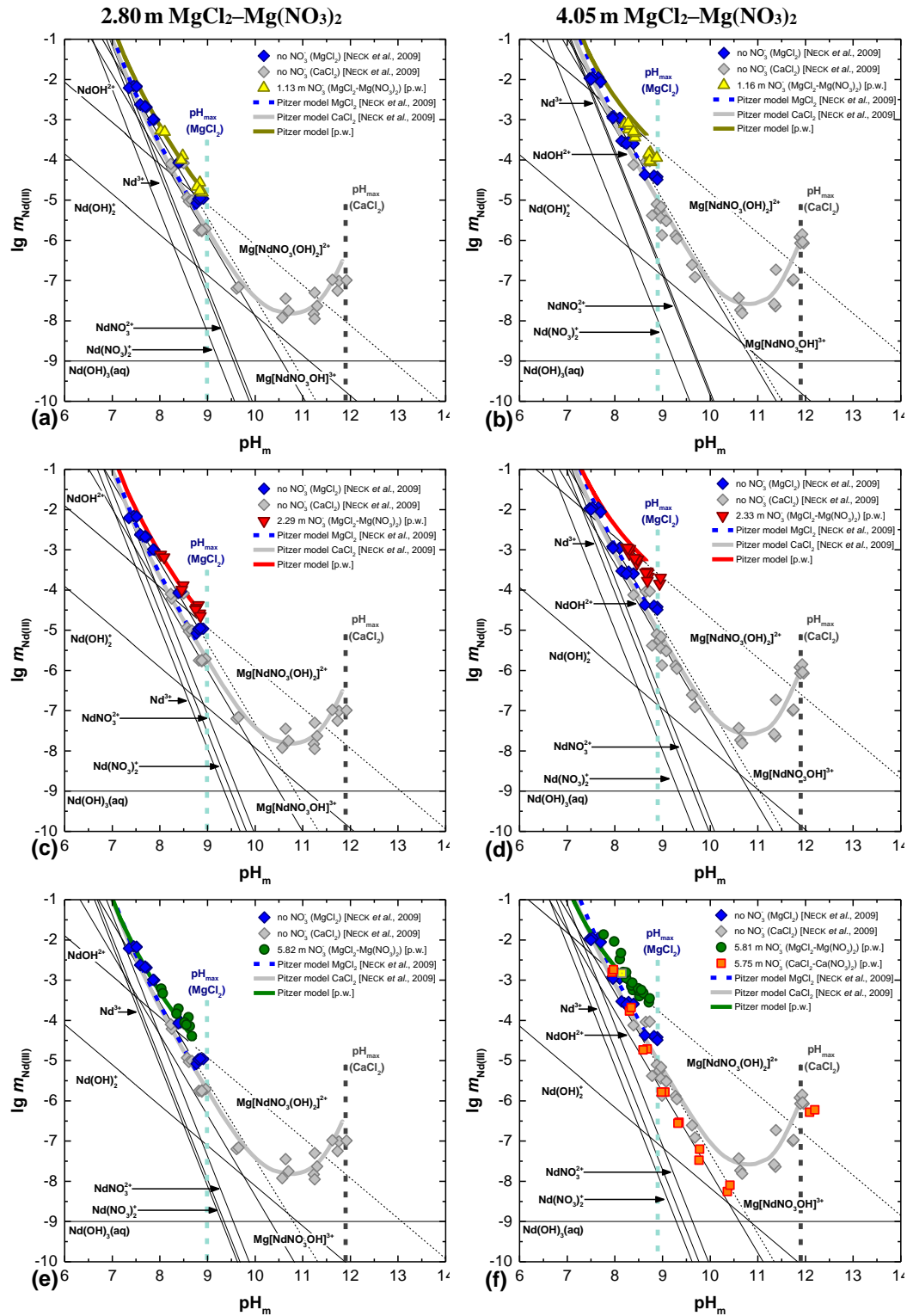


Figure 5.2: Solubility of $\text{Nd}(\text{OH})_3(\text{s})$ in 2.80 m $\text{MgCl}_2\text{-Mg}(\text{NO}_3)_2$ with (a) 1.13 m, (c) 2.29 m and (e) 5.82 m NO_3^- in comparison with 4.05 m $\text{MgCl}_2\text{-Mg}(\text{NO}_3)_2$ with (b) 1.16 m, (d) 2.33 m and (f) 5.82 m NO_3^- . The solubility data of $\text{Nd}(\text{OH})_3(\text{s})$ in 4.02 m $\text{CaCl}_2\text{-Ca}(\text{NO}_3)_2$ with 5.75 m NO_3^- are also included in figure (f). Reference data in nitrate-free solutions [NECK *et al.*, 2009] are included in all the figures for comparison. Yellow square in (f) indicates the sample used for Nd-L_{III} EXAFS measurements. Thick solid lines correspond to Nd(III) solubility calculated using thermodynamic and activity models: for pure MgCl_2 and CaCl_2 systems (blue and gray lines) [NECK *et al.*, 2009], and for $\text{MgCl}_2\text{-Mg}(\text{NO}_3)_2$ mixtures (yellow, red, green lines) [p.w.]. Thin lines show Nd(III) aqueous speciation underlying $\text{Nd}(\text{OH})_3(\text{s})$ solubility curve in $\text{MgCl}_2\text{-Mg}(\text{NO}_3)_2$ systems.

Results and Discussion

In contrast to the $\text{MgCl}_2\text{-Mg(NO}_3)_2$ system, no significant enhancement in $\text{Nd(OH)}_3(\text{s})$ solubility occurs in 2.85 m (see appendix, Table A.3) and 4.02 m $\text{CaCl}_2\text{-Ca(NO}_3)_2$ mixtures with nitrate concentrations up to 5.75 m, compared to nitrate-free CaCl_2 systems under virtually the same experimental conditions [NECK *et al.*, 2009]. This observation suggests the absence of Nd(III)-OH-NO_3 complexes in CaCl_2 solutions and thus the likely participation of Mg^{2+} in the formation of Nd(III)-NO_3 complexes in concentrated nitrate bearing $\text{MgCl}_2\text{-Mg(NO}_3)_2$ solutions and pH_m 8–9.

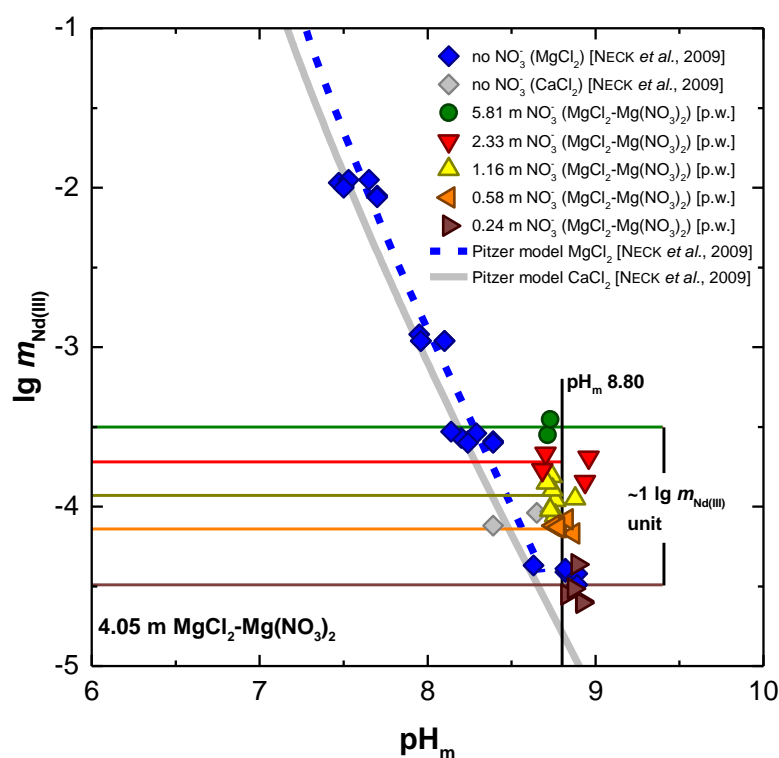


Figure 5.3: Solubility of $\text{Nd(OH)}_3(\text{s})$ in 4.05 m $\text{MgCl}_2\text{-Mg(NO}_3)_2$ solution at $\text{pH}_m = 8.80$ with increasing nitrate concentration. Reference data in nitrate-free solutions [NECK *et al.*, 2009] are included for comparison. Thick solid lines correspond to the Nd(III) solubility calculated for pure MgCl_2 and CaCl_2 using thermodynamic and activity models: for pure MgCl_2 and CaCl_2 systems (blue and gray lines) [NECK *et al.*, 2009].

5.1.2 Solid phase characterization in NaCl–NaNO₃, MgCl₂–Mg(NO₃)₂ and CaCl₂–Ca(NO₃)₂ mixtures

In all evaluated Na–Mg–Cl–NO₃ systems with $m_{\text{Cl}^-} \leq 5.82$ m, the diffractograms of solid phases recovered from selected solubility experiments match the XRD pattern of the initial Nd(OH)₃(s) powder (Figure 5.4) and are in excellent agreement with the Nd(OH)₃(s) reference diffractogram in [BEALL *et al.*, 1976] (PDF 70-0215). Besides Nd(OH)₃(s), reflexes belonging to brucite (PDF 74-2220; [ISETTI, 1965]) and Mg-oxychloride (PDF 07-0412; [DE WOLFF, 1957]), initially added to the samples, are clearly identified in those solid phases recovered from experiments with $\text{pH}_m = \text{pH}_{\text{max}}$ (data not shown).

A number of solid phases recovered from the solubility experiments in MgCl₂–Mg(NO₃)₂ solutions were also analyzed by scanning electron microscopy. SEM-EDS analysis show a considerable enrichment of chlorine in Nd(III) solid phases equilibrated with solutions at $m_{\text{Mg}^{2+}} \geq 4.05$ m and $m_{\text{Cl}^-} \geq 5.82$ m. These results hint towards a solid phase transformation in concentrated chloride brines and is further discussed in section 5.2, where a comprehensive study evaluating the formation, stability and solubility of Nd(III)–OH–Cl(s) phases is provided.

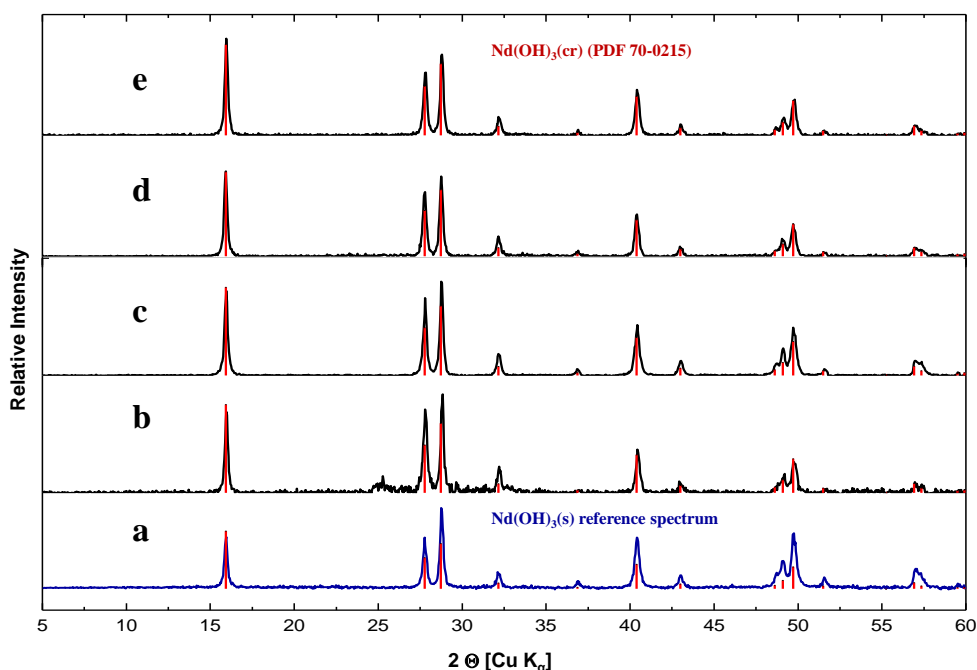


Figure 5.4: XRD patterns of Nd(III) solid phases recovered from batch solubility experiments in $\text{MgCl}_2\text{--Mg}(\text{NO}_3)_2$ systems. Initial $\text{Nd}(\text{OH})_3(\text{s})$ material (a), solid phases recovered from solubility experiments in 4.05 m $\text{MgCl}_2\text{--Mg}(\text{NO}_3)_2$ with (b) 5.81 m NO_3^- at $\text{pH}_m = 8.43$ after 331 days and (c) 2.33 m NO_3^- at $\text{pH}_m = 8.54$ after 79 days. Diffractograms (d) and (e) correspond to solid phases recovered from solubility experiments in 2.80 m $\text{MgCl}_2\text{--Mg}(\text{NO}_3)_2$ mixtures with 5.82 m NO_3^- at $\text{pH}_m = 8.42$ after 331 days and containing no nitrate at $\text{pH}_m = 8.49$ after 330 days, respectively.

5.1.3 Cm(III)–TRLFS studies in $\text{NaCl}\text{--NaNO}_3$, $\text{MgCl}_2\text{--Mg}(\text{NO}_3)_2$ and $\text{CaCl}_2\text{--Ca}(\text{NO}_3)_2$ mixtures

Figure 5.5 (a to e) shows a selection of Cm(III)–TRLFS spectra collected in 5.61 m NaCl, 6.02 m NaNO_3 , 4.05 m MgCl_2 , 4.05 m $\text{MgCl}_2\text{--Mg}(\text{NO}_3)_2$ and 4.02 m $\text{CaCl}_2\text{--Ca}(\text{NO}_3)_2$ systems. The Cm^{3+} aquo ion reference spectrum measured in a dilute

acidic solution is shown in all the figures. All other Cm(III) spectra collected in this work for MgCl₂–Mg(NO₃)₂ systems are provided in Figure B.1 in the appendix.

In the absence of other complexing ligands, a number of binary Cm(III) hydroxide, chloride and nitrate species are expected to be present in solution under acidic to weakly alkaline pH conditions. Their relative contribution depends on the pH, ionic strength and electrolyte composition. Wavelengths reported for binary Cm(III)–OH, Cm(III)–Cl and Cm(III)–NO₃ species have been included in the figures for comparison purposes [FANGHÄNEL *et al.*, 1994; FANGHÄNEL *et al.*, 1995; FANGHÄNEL AND KIM, 1998; RABUNG *et al.*, 2008; SKERENCAK *et al.*, 2009].

The second Cm(III) hydrolysis species dominates in 5.61 m NaCl (Figure 5.5 a) over the investigated pH range (between 7.95 and 8.95), whereas binary Cm(III)–NO₃ species prevail in 6.02 m NaNO₃ and pH_m = 7.93 (Figure 5.5 b). At pH_m ≥ 8.93, Cm(OH)₂⁺ becomes also predominant in 6.02 m NaNO₃ (Figure 5.5 b). The definition of additional species is not necessary to explain Cm(III) spectra collected in NaCl–NaNO₃ solutions, except some minor abundance of chloro-species in 5.61 m NaCl.

Cm(III) spectra collected in 4.05 m MgCl₂ (Figure 5.5 c) at 2.95 ≤ pH_m ≤ 8.45 are dominated by the Cm³⁺ aquo ion and binary Cm(III)–Cl species, whereas the second hydrolysis species of Cm(III) increases with pH_m and dominates at pH_m > 8.45. In the case of the 4.05 m MgCl₂–Mg(NO₃)₂ system (Figure 5.5 d), binary Cm(III)–NO₃ species dominate the spectra in the pH range 2.94 ≤ pH_m ≤ 8.14. Above pH_m ≈ 8.14, additional Cm(III) complexes with a very clear pH dependency form in this system. Peak deconvolution confirms the presence of two new components at λ = 602.7 nm and λ = 606.0 nm. These species are absent in pure MgCl₂ solutions of the same ionic strength, which clearly indicates the participation of nitrate in the complex formation. The component at λ = 602.7 nm has been assigned to the moiety “CmNO₃OH⁺”, based on λ(Cm(NO₃)₂⁺) = 602.2 nm [SKERENCAK *et al.*, 2009] and λ(Cm(OH)₂⁺) = 603.5 nm [FANGHÄNEL *et al.*, 1994; FANGHÄNEL AND KIM, 1998;

RABUNG *et al.*, 2008], and considering that stronger ligands (e.g. $\text{OH}^- > \text{NO}_3^-$) induce a greater red-shift in the Cm(III) spectra than weaker ones. The strongly red-shifted Cm(III) shoulder at $\lambda = 606.0 \text{ nm}$ has been assigned to the moiety “ $\text{CmNO}_3(\text{OH})_2(\text{aq})$ ”, taking also as a reference the wavelength reported for the complex $\text{Cm}(\text{OH})_3(\text{aq})$ ($\lambda = 607.5 \text{ nm}$) [RABUNG *et al.*, 2008].

The spectra collected in 4.02 m $\text{CaCl}_2\text{--Ca}(\text{NO}_3)_2$ (Figure 5.5 e) differ significantly from the 4.05 m $\text{MgCl}_2\text{--Mg}(\text{NO}_3)_2$ system and can be explained considering mainly the formation of binary Cm(III)– NO_3 species with minor contributions of chloro and hydroxo complexes. No mixed Cm(III)– $\text{NO}_3\text{--OH}$ complexes are observed in relevant concentrations at $\text{pH}_m \leq 8.63$. The absence of these species in $\text{CaCl}_2\text{--Ca}(\text{NO}_3)_2$ solutions under the same experimental conditions (pH_m , I_m , $m_{\text{NO}_3^-}$) as in the $\text{MgCl}_2\text{--Mg}(\text{NO}_3)_2$ systems hints towards the participation of Mg^{2+} in the complexation reaction. Consequently, the formation of the quaternary aqueous species $\text{Mg}[\text{CmNO}_3\text{OH}]^{3+}$ and $\text{Mg}[\text{CmNO}_3(\text{OH})_2]^{2+}$ is proposed and has been considered in the thermodynamic modelling summarized in section 5.1.5. Note that under alkaline conditions ($\text{pH}_m > 10$) and absence of nitrate, Neck and co-workers [NECK *et al.*, 2009] proposed the formation of the ternary species $\text{Ca}[\text{Cm}(\text{OH})_3]^{2+}$ holding the same ligand stoichiometry and charge. These Cm(III)–TRLFS observations are consistent with Nd(III) solubility data under analogous experimental conditions, and thus confirm that the observed increase in solubility for $\text{Nd}(\text{OH})_3(\text{s})$ is not caused by ion interaction processes, but is related to a genuine Cm(III) complexation reaction with nitrate.

All pure component spectra derived by peak deconvolution using the complete set of TRLFS spectra collected in 4.0 m $\text{MgCl}_2\text{--Mg}(\text{NO}_3)_2$ mixtures with $2.93 \leq \text{pH}_m \leq 8.95$ and $0.00 \leq m_{\text{NO}_3^-} \leq 8.04$ are shown in Figure 5.5 f.

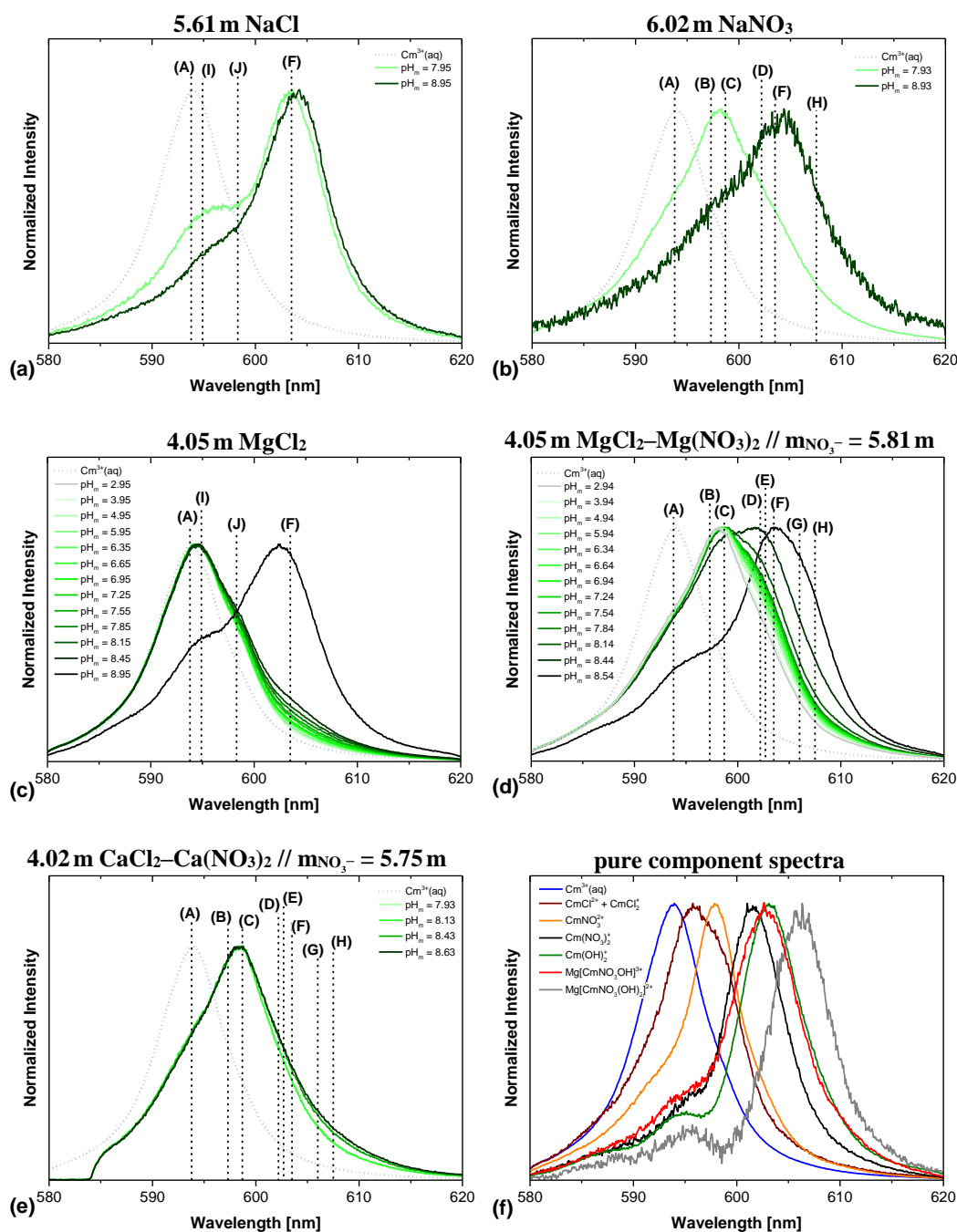


Figure 5.5: Selection of experimental Cm(III)-TRLFS spectra over the entire investigated pH range in (a) 5.61 m NaCl, (b) 6.02 m NaNO_3 , (c) 4.05 m MgCl_2 , (d) 4.05 m MgCl_2 - $\text{Mg}(\text{NO}_3)_2$ mixture with $m_{\text{NO}_3^-} = 5.81$ m and (e) 4.02 m CaCl_2 - $\text{Ca}(\text{NO}_3)_2$ mixture with $m_{\text{NO}_3^-} = 5.75$ m. Figure (f) shows all pure component spectra obtained by peak deconvolution of experimental spectra collected in MgCl_2 - $\text{Mg}(\text{NO}_3)_2$ systems. Capital letters in figures (a) to (e) refer to: A = Cm^{3+} aquo ion, B = CmNO_3^{2+} , C = CmOH^{2+} , D = $\text{Cm}(\text{NO}_3)_2^+$, E = $\text{Mg}[\text{CmNO}_3(\text{OH})]^{3+}$, F = $\text{Cm}(\text{OH})_2^+$, G = $\text{Mg}[\text{CmNO}_3(\text{OH})_2]^{2+}$, H = $\text{Cm}(\text{OH})_3(\text{aq})$, I = CmCl_2^+ and J = CmCl_2^+ .

5.1.4 Nd–L_{III} EXAFS investigations in MgCl₂–Mg(NO₃)₂ mixtures

Figure 5.6 shows the k^2 -weighted Nd–L_{III} Fourier transform EXAFS spectrum collected for the supernatant (after 10kD ultrafiltration) of the Nd(III) solubility sample in 4.05 m MgCl₂–Mg(NO₃)₂ with 5.81 m NO₃[–] and pH_m = 8.15, (see Figure 5.2 f). The structural parameters resulting from EXAFS evaluation are shown in Table 5.1. The best fit in the FT range [1.25–4.5 Å] is obtained using 6 shells. In addition to O and N shells, a shell with Mg²⁺ as backscatterer is needed to fit the peak at ~4 Å. Furthermore, no Nd–Nd interaction can be evidenced within the R range taken into account. The fit model hints to a mixture of species having one and two nitrate groups, where at least one of these species has Mg²⁺ in the direct vicinity of OH- and/or NO₃-groups. These results are in good agreement with Cm(III)–TRLFS observations in MgCl₂–Mg(NO₃)₂ systems (see Figure 5.5 d), where a mixture of binary and quaternary nitrate-bearing aqueous species were identified under analogous experimental conditions. In conclusion, Nd–L_{III} EXAFS confirms the formation of quaternary Mg–Nd(III)–NO₃–OH inner-sphere complexes with participation of Mg²⁺ and the absence of polymeric/colloidal Nd(III) species in solution.

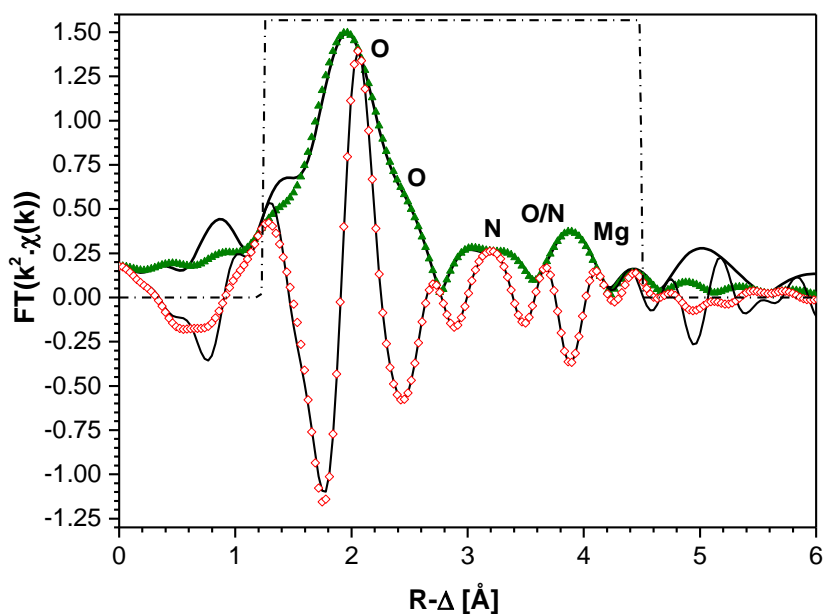


Figure 5.6: Experimental (solid lines) and fitted (symbols) k^2 -weighted Nd-L_{III} Fourier transform EXAFS spectrum of neodymium in 4.05 m MgCl₂-Mg(NO₃)₂ solution with 5.81 m NO₃⁻. Dashed line corresponding to the R-window considered in the fit.

Table 5.1: Structural parameters obtained from EXAFS data evaluation.

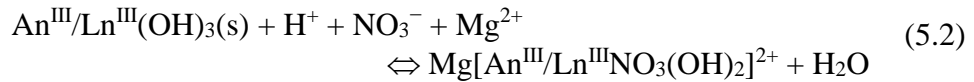
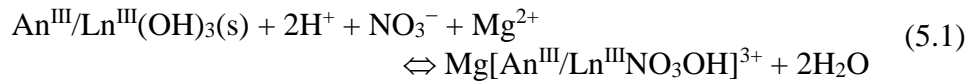
Backscatterer	R [Å] (± 0.01 Å)	N (± 20%)	σ^2 [Å ²] $\times 10^{-3}$	ΔE_0 [eV]	goodness of fit (%)
O	2.46	6.1	3.1		
O	2.64	4.7	3.5		
N	3.18	1.7	3.3	8.9	1.0
O/N	3.63	3.6	9.0		
Mg	4.10	2.6	0.4		
O	4.47	4.9	3.5		

R = distances, N = coordination number, σ^2 = EXAFS Debye-Waller factors,

ΔE_0 = relative energy held as global parameters for all atoms, S_0^2 set to 1

5.1.5 Chemical, thermodynamic and activity models

The thermodynamic model derived in [NECK *et al.*, 2009] for Ln(III) and An(III) in NaCl, MgCl₂ and CaCl₂ solutions is extended in the present work to nitrate-bearing systems by combining the results from solubility data, spectroscopic techniques and solid phase characterization. Nd(OH)₃(s) is confirmed by XRD and SEM-EDS as solid phase controlling the solubility in all the evaluated systems with $m_{\text{Cl}^-} \leq 5.82$ m. The formation of the aqueous species $\text{Mg}[\text{An}^{\text{III}}/\text{Ln}^{\text{III}}\text{NO}_3\text{OH}]^{3+}$ and $\text{Mg}[\text{An}^{\text{III}}/\text{Ln}^{\text{III}}\text{NO}_3(\text{OH})_2]^{2+}$ is proposed based on slope analysis, Cm(III)–TRLFS and Nd–L_{III} EXAFS. Hence, equilibrium reactions (5.1) and (5.2) can be defined, in combination with equations (5.3)–(5.6) for the calculation of the corresponding $\lg^*K'_{s,(1,1,n,1)}$ and $\lg^*K^{\circ}_{s,(1,1,n,1)}$ with $n = 1$ or 2 .



with

$$\begin{aligned} \lg^*K'_{s,(1,1,1,1)} = \lg [\text{Mg}[\text{An}^{\text{III}}/\text{Ln}^{\text{III}}\text{NO}_3\text{OH}]^{3+}] \\ - 2\lg [\text{H}^+] - \lg [\text{NO}_3^-] - \lg [\text{Mg}^{2+}] \end{aligned} \quad (5.3)$$

$$\begin{aligned} \lg^*K'_{s,(1,1,2,1)} = \lg [\text{Mg}[\text{An}^{\text{III}}/\text{Ln}^{\text{III}}\text{NO}_3(\text{OH})_2]^{2+}] \\ - \lg [\text{H}^+] - \lg [\text{NO}_3^-] - \lg [\text{Mg}^{2+}] \end{aligned} \quad (5.4)$$

and

$$\lg^* K_{s,(1,1,1,1)}^{\circ} = \lg^* K_{s,(1,1,1,1)}^{\gamma} + \lg \gamma_{\text{Mg}[\text{An}^{\text{III}}/\text{Ln}^{\text{III}}\text{NO}_3\text{OH}]^{3+}} - 2 \lg \gamma_{\text{H}^+} - \lg \gamma_{\text{NO}_3^-} - \lg \gamma_{\text{Mg}^{2+}} + 2 \lg a_w \quad (5.5)$$

$$\lg^* K_{s,(1,1,2,1)}^{\circ} = \lg^* K_{s,(1,1,2,1)}^{\gamma} + \lg \gamma_{\text{Mg}[\text{An}^{\text{III}}/\text{Ln}^{\text{III}}\text{NO}_3(\text{OH})_2]^{3+}} - \lg \gamma_{\text{H}^+} - \lg \gamma_{\text{NO}_3^-} - \lg \gamma_{\text{Mg}^{2+}} + \lg a_w \quad (5.6)$$

Provided the very high ionic strength in most of the evaluated systems where the effect of nitrate is observed ($I_m \geq 8.52 \text{ m}$), the Pitzer formulism has been preferred for the thermodynamic modelling [PITZER, 1991]. Parameters reported in [HARVIE *et al.*, 1984; PITZER, 1991] are used for the calculation of a_w and the activity coefficients of Mg^{2+} , Cl^- , NO_3^- and H^+ . Pitzer ion interaction coefficients for Nd(III) species derived in chloride media are reported in [NECK *et al.*, 2009]. Conditional equilibrium constants reported for binary Cm(III)– NO_3 species at $T = 25^\circ\text{C}$ and $0.10 \text{ m} \leq m_{\text{NO}_3^-} \leq 4.61 \text{ m}$ ($I \leq 4.61 \text{ m}$) [SKERENCAK *et al.*, 2009] have been used in the present work to determine the corresponding $\lg \beta^\circ$ and ion interaction parameters using the Pitzer approach (Table 5.2). For the new species $\text{Mg}[\text{An}^{\text{III}}/\text{Ln}^{\text{III}}\text{NO}_3\text{OH}]^{3+}$ and $\text{Mg}[\text{An}^{\text{III}}/\text{Ln}^{\text{III}}\text{NO}_3(\text{OH})_2]^{2+}$, only the binary parameters $\beta^{(0)}$ and the corresponding stability constant at $I = 0$ were calculated. Typical values for analogous cation-anion pairs of the same valence type are used for $\beta^{(1)}$, whereas C^ϕ was set to 0 [GRENTH AND PLYASUNOV, 1997; PLYASUNOV *et al.*, 1998]. Ternary Pitzer parameters are generally set to 0. The difference between experimental and modelled solubility was minimized by optimizing $\beta^{(0)}$ and $\lg^* K_{s,(1,1,n,1)}^{\circ}$ for the species $\text{Mg}[\text{An}^{\text{III}}/\text{Ln}^{\text{III}}\text{NO}_3\text{OH}]^{3+}$ and $\text{Mg}[\text{An}^{\text{III}}/\text{Ln}^{\text{III}}\text{NO}_3(\text{OH})_2]^{2+}$. A relevant constrain in the modelling exercise is the assumption that ion interaction parameters of cations with Cl^- and NO_3^- are the same. This assumption is based on the very similar solubility of $\text{Nd}(\text{OH})_3(\text{s})$ in NaCl – NaNO_3 and CaCl_2 – $\text{Ca}(\text{NO}_3)_2$ mixtures compared to the nitrate-free reference systems [NECK *et al.*, 2009] and the very similar SIT ion interaction parameters reported for +1 to +4 monomeric cations

Results and Discussion

[RAND *et al.*, 2008] (see Figure C.1 in the appendix). This permits to importantly decrease the number of unknown parameters whilst avoiding relevant variations in the activity coefficients for mixed solutions of same ionic strength but different $\text{Cl}^-/\text{NO}_3^-$ ratio.

Only solubility data collected for 0.25, 1.04, 2.80 and 4.05 m $\text{MgCl}_2\text{-Mg}(\text{NO}_3)_2$ were considered for the optimization exercise, consistently with the validity of the thermodynamic model derived in [NECK *et al.*, 2009]. Note that solubility samples in pure 4.05 m $\text{Mg}(\text{NO}_3)_2$ were disregarded in the calculations due to alterations in XRD pattern and SEM-EDS characterization with respect to the original $\text{Nd}(\text{OH})_3(\text{s})$ material. Stability constants and Pitzer ion interaction coefficients resulting from the optimization exercise are shown in Table 5.2 and Table 5.3, respectively, together with the constants and parameters of all other species and solid phases of relevance in the system $\text{Ln}^{3+}/\text{An}^{3+}\text{-H}^+\text{-Na}^+\text{-Mg}^{2+}\text{-Ca}^{2+}\text{-OH}^-\text{-Cl}^-\text{-NO}_3^-\text{-H}_2\text{O}$. Solubility curves and underlying aqueous speciation calculated with the thermodynamic and activity models summarized in Table 5.2 and Table 5.3 are shown in Figure 5.1, Figure 5.2 and Figure A.1.

Table 5.2: Equilibrium constants ($I = 0$, 25°C) for the solid hydroxides and aqueous complexes of Am(III)/Cm(III) and Nd(III).

Solubility: $\lg * K_{s,0}^{\circ} [M(OH)_3(s) + 3H^+ \Leftrightarrow M^{3+} + 3H_2O]$				
Am(OH) ₃ (cr/aged)	15.6 ± 0.6 [GUILLAUMONT <i>et al.</i> , 2003]	Nd(OH) ₃ (cr/aged)	16.0 ± 0.4 [DIAKONOV <i>et al.</i> , 1998b]	
Am(OH) ₃ (am)	16.9 ± 0.8 [GUILLAUMONT <i>et al.</i> , 2003]	Nd(OH) ₃ (s)	17.2 ± 0.4 [NECK <i>et al.</i> , 2009]	
Hydroxide complexes: $\lg * \beta_{1,n}^{\circ} [M^{3+} + nH_2O \Leftrightarrow M(OH)_n^{3-n} + nH^+]$				
AnOH ²⁺ (Am/Cm)	-7.2 ± 0.5 [GUILLAUMONT <i>et al.</i> , 2003]	NdOH ²⁺	-7.4 ± 0.4 [NECK <i>et al.</i> , 2009]	
An(OH) ₂ ⁺ (Am/Cm)	-15.1 ± 0.7 [GUILLAUMONT <i>et al.</i> , 2003]	Nd(OH) ₂ ⁺	-15.7 ± 0.7 [NECK <i>et al.</i> , 2009]	
Am(OH) ₃ (aq)	-26.2 ± 0.5 [GUILLAUMONT <i>et al.</i> , 2003]	Nd(OH) ₃ (aq)	analogous Am value	
Am(OH) ₄ ⁻	-40.7 ± 0.7 [NECK <i>et al.</i> , 2009]	Nd(OH) ₄ ⁻	analogous Am value	
Chloride complexes: $\lg \beta_{1,q}^{\circ} [M^{3+} + qCl^- \Leftrightarrow MCl_q^{3-q}]$				
AnCl ²⁺ (Am/Cm)	0.24 ± 0.03 [KÖNNECKE <i>et al.</i> , 1997; GUILLAUMONT <i>et al.</i> , 2003]	NdCl ²⁺	analogous Cm value	
AnCl ₂ ⁺ (Am/Cm)	-0.74 ± 0.05 [KÖNNECKE <i>et al.</i> , 1997; GUILLAUMONT <i>et al.</i> , 2003]	NdCl ₂ ⁺	analogous Cm value	
Nitrate complexes: $\lg \beta_{1,q}^{\circ} [M^{3+} + qNO_3^- \Leftrightarrow M(NO_3)_q^{3-q}]$				
AnNO ₃ ²⁺ (Cm)	1.33 ± 0.10 [p.w.] ^a	NdNO ₃ ²⁺	analogous Cm value	
An(NO ₃) ₂ ⁺ (Cm)	1.03 ± 0.10 [p.w.] ^a	Nd(NO ₃) ₂ ⁺	analogous Cm value	
Mg-M(III)-NO₃-OH complexes: $\lg * \beta_{1,1,n,1}^{\circ} [Mg^{2+} + M^{3+} + NO_3^- + nH_2O \Leftrightarrow Mg[MNO_3(OH)_n]^{4-n} + nH^+; n = 1, 2]$				
Mg[AnNO ₃ OH] ³⁺ (Am/Cm)	analogous Nd value	Mg[NdNO ₃ OH] ³⁺	-6.4 ± 0.5 [p.w.]	
Mg[AnNO ₃ (OH) ₂] ²⁺ (Am/Cm)	analogous Nd value	Mg[NdNO ₃ (OH) ₂] ²⁺	-15.6 ± 0.5 [p.w.]	

^a calculated in this work from original experimental data ($\lg K^{\circ}$) in [SKERENCAK *et al.*, 2009].

Table 5.3: Ion interaction (Pitzer) coefficients for M(III) species (M = Am, Cm, Pu and Nd) in chloride/nitrate media at 25°C; $\beta^{(0)ik}$, $\beta^{(1)ik}$, λ_{ik} and θ_{ij} in [kg·mol⁻¹], C^{ϕ}_{ik} and ψ_{ijk} in [kg²·mol⁻²].

Binary Pitzer parameter	k	$\beta^{(0)ik}$	$\beta^{(1)ik}$	C^{ϕ}_{ik}	Ternary parameter	θ_{ij}	Pitzer	Ref.
M^{3+}	Cl ⁻ /NO ₃ ⁻	0.5856	5.60	-0.016	Na ⁺	0.10	0	[KÖNNECKE <i>et al.</i> , 1997]
					Ca ²⁺ /Mg ²⁺	0.20	0	[KÖNNECKE <i>et al.</i> , 1997]
MOH ²⁺	Cl ⁻ /NO ₃ ⁻	0.055	1.81	0	Na ⁺	0	0	[NECK <i>et al.</i> , 1998]
					Ca ²⁺ /Mg ²⁺	0	0.04	[NECK <i>et al.</i> , 2009]
M(OH) ₂ ⁺	Cl ⁻ /NO ₃ ⁻	-0.13	0	0	Na ⁺	0	0	[NECK <i>et al.</i> , 2009]
					Ca ²⁺ /Mg ²⁺	0.29	0.07	[NECK <i>et al.</i> , 2009]
M(OH) ₃ (aq)	Na ⁺	$\lambda_{ik} = -0.2$						[KÖNNECKE <i>et al.</i> , 1997]
					$\lambda_{ik} = 0$ for $k = K^+, Ca^{2+}, Mg^{2+}, Cl^-, NO_3^-, OH^-$			[NECK <i>et al.</i> , 2009]
MCl ²⁺	Cl ⁻ /NO ₃ ⁻	0.593	3.15	-0.006	Na ⁺	0	0	[KÖNNECKE <i>et al.</i> , 1997]
					Ca ²⁺ /Mg ²⁺	-0.014	0	[KÖNNECKE <i>et al.</i> , 1997]
MCl ₂ ⁺	Cl ⁻ /NO ₃ ⁻	0.516	1.75	0.010	Na ⁺	0	0	[KÖNNECKE <i>et al.</i> , 1997]
					Ca ²⁺ /Mg ²⁺	-0.196	0	[KÖNNECKE <i>et al.</i> , 1997]
MNO ₃ ²⁺	Cl ⁻ /NO ₃ ⁻	0.42	1.83	0.050	Na ⁺	0	0	[p.w.] ^a
					Ca ²⁺ /Mg ²⁺	0	0	[p.w.] ^a
M(NO ₃) ₂ ⁺	Cl ⁻ /NO ₃ ⁻	0.25	0.32	0.1	Na ⁺	0	0	[p.w.] ^a
					Ca ²⁺ /Mg ²⁺	0	0	[p.w.] ^a
Mg[MNO ₃ OH] ³⁺	Cl ⁻ /NO ₃ ⁻	0.93	4.30	0	Na ⁺	0	0	[p.w.]
					Ca ²⁺ /Mg ²⁺	0	0	[p.w.]
Mg[MNO ₃ (OH) ₂] ²⁺	Cl ⁻ /NO ₃ ⁻	0.18	1.60	0	Na ⁺	0	0	[p.w.]
					Ca ²⁺ /Mg ²⁺	0	0	[p.w.]

^a calculated in this work from original experimental data (lgK^o) in [SKERENČAK *et al.*, 2009].

5.1.6 Conclusions regarding the effect of nitrate on the solubility of An^{III}/Ln^{III}

The effect of nitrate on the solubility of An^{III}/Ln^{III} was studied in dilute to concentrated NaCl–NaNO₃, MgCl₂–Mg(NO₃)₂ and CaCl₂–Ca(NO₃)₂ solutions using batch solubility experiments, Cm(III)–TRLFS, Nd–L_{III} EXAFS and extensive solid phase characterization (XRD and SEM-EDS).

Nitrate has a significant impact on the solubility of Nd(OH)₃(s) in concentrated weakly alkaline MgCl₂–Mg(NO₃)₂ solutions with total salt concentration ≥ 2.83 m and $m_{\text{NO}_3^-} \geq 1.13$ m. However, no effect of nitrate is observed in NaCl–NaNO₃ and CaCl₂–Ca(NO₃)₂ mixtures under analogous experimental conditions, thus indicating the relevant role of Mg²⁺ in the interaction between Nd(III) and nitrate. Cm(III)–TRLFS and Nd–L_{III} EXAFS confirm the participation of Mg²⁺ in the formation of quaternary inner-sphere complexes of the type Mg–An^{III}/Ln^{III}–NO₃–OH.

The combination of slope analyses, TRLFS, EXAFS and solid phase characterization confirms the relevance of the equilibrium reactions $\text{An}^{\text{III}}/\text{Ln}^{\text{III}}(\text{OH})_3(\text{s}) + \text{H}^+ + \text{NO}_3^- + \text{Mg}^{2+} \Leftrightarrow \text{Mg}[\text{An}^{\text{III}}/\text{Ln}^{\text{III}}\text{NO}_3(\text{OH})_2]^{2+} + \text{H}_2\text{O}$ and $\text{An}^{\text{III}}/\text{Ln}^{\text{III}}(\text{OH})_3(\text{s}) + 2\text{H}^+ + \text{NO}_3^- + \text{Mg}^{2+} \Leftrightarrow \text{Mg}[\text{An}^{\text{III}}/\text{Ln}^{\text{III}}\text{NO}_3\text{OH}]^{3+} + 2\text{H}_2\text{O}$ in the control of the solubility of An^{III}/Ln^{III} in concentrated MgCl₂–Mg(NO₃)₂ brines. Based on the newly generated data, the chemical, thermodynamic and activity models described in [NECK *et al.*, 2009] for Ln(III) and An(III) are further extended to Ln³⁺/An³⁺–H⁺–Na⁺–Mg²⁺–Ca²⁺–OH[–]–Cl[–]–NO₃[–]–H₂O systems.

This is the first comprehensive experimental study providing a quantitative thermodynamic description of the effect of nitrate on the aquatic chemistry of Ln(III) and An(III) under repository-relevant pH conditions. This study also highlights the key role of spectroscopic techniques in defining correct chemical models of

complex systems, especially when involving the formation of “weak complexes” in contraposition to matrix effects or pure ion interaction processes.

5.2 Mixed Nd(III)–OH–Cl(s) phases in concentrated NaCl, MgCl₂ and CaCl₂ brines: Formation, stability and solubility

An appropriate knowledge of the solubility controlling solid phase is mandatory in source term estimations and for accurate geochemical calculations. Trivalent (An^{III}) and tetravalent (An^{IV}) actinides will prevail under the reducing conditions expected after the closure of a deep geological repository for nuclear waste products. $An^{III}/Ln^{III}(OH)_3(s)$ are usually considered as solubility limiting solid phases of trivalent actinides/lanthanides in dilute to concentrated saline systems in the absence of complexing ligands. The successful synthesis of ternary An^{III}/Ln^{III} –OH–Cl(s) phases has been reported in structural studies, but no thermodynamic data has been derived so far for these systems [KLEVTSOV *et al.*, 1969; BUKIN, 1972; KLEVTSOV *et al.*, 1973; ZEHNDER *et al.*, 2010]. The formation and stability of these solid phases forming in-situ under repository conditions, can have relevant implications in the source term of disposal concepts where high chloride concentrations are expected.

In a first part of this work, the transformation of $Nd(OH)_3(s)$ into a ternary Nd–OH–Cl(s) phase was experimentally assessed as a function of pH ($7.5 \leq pH_m \leq 9.6$) and temperature ($T = 22$ and $80^\circ C$) in 5.61 m NaCl, 0.25–5.15 m MgCl₂ and 3.91 m CaCl₂ solutions. In a second part of the present study, the thermodynamic properties

of $\text{Nd}(\text{OH})_2\text{Cl}(\text{s})$ were investigated. Extensive batch solubility experiments were performed under argon atmosphere and room temperature. Undersaturation solubility experiments were conducted using $\text{Nd}(\text{OH})_2\text{Cl}(\text{s})$ synthesized at $T = 22^\circ\text{C}$ in the first part of this study. Experiments were carried out under repository-relevant pH conditions in 5.61 m NaCl ($7.5 \leq \text{pH}_m \leq 13.0$), 2.11–5.15 m MgCl_2 ($7.0 \leq \text{pH}_m \leq 9.0$) and 2.68/3.91 m CaCl_2 ($7.2 \leq \text{pH}_m \leq 12.0$) solutions. A detailed solid phase characterization (XRD and SEM-EDS) was performed to gain insights into the solid phases prevailing in the studied systems. In a second set of experiments (“mixing” experiments), $\text{Nd}(\text{OH})_2\text{Cl}(\text{s})$ and $\text{Nd}(\text{OH})_3(\text{s})$ were mixed and equilibrated under pH-unbuffered conditions with analogous background electrolyte and salt concentrations. The combination of these approaches allowed the development of the chemical and thermodynamic models for these systems.

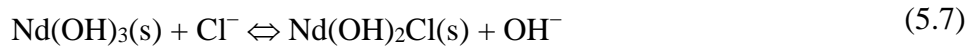
5.2.1 Formation and stability of Nd–OH–Cl(s) phases in NaCl, MgCl_2 and CaCl_2 solutions

XRD characterization of Nd solid phases equilibrated in concentrated MgCl_2 solutions (≥ 3.87 m) at $\text{pH}_m = 8$ –9 show a complete transformation of the initial $\text{Nd}(\text{OH})_3(\text{s})$ solid phase into $\text{Nd}(\text{OH})_2\text{Cl}(\text{s})$, both at $T = 22$ and 80°C (see Figure 5.7). $\text{Nd}(\text{OH})_3(\text{s})$ transforms very fast (≈ 42 days) into $\text{Nd}(\text{OH})_2\text{Cl}(\text{s})$ in 5.15 m MgCl_2 and $\text{pH}_m = 8.0$ at $T = 22^\circ\text{C}$. On the other hand, $\text{Nd}(\text{OH})_3(\text{s})$ equilibrated at the same temperature in ≥ 3.87 m MgCl_2 and higher pH_m (≈ 8.8) shows distinctly slow transformation kinetics ($>$ one year). Solid phase transformation is also accelerated at $T = 80^\circ\text{C}$, where $\text{Nd}(\text{OH})_2\text{Cl}(\text{s})$ prevails in ≥ 3.87 m MgCl_2 and pH_m up to pH_{max} (≈ 8.8) after an equilibration time of 40 days. The comparison of XRD

Results and Discussion

patterns in Figure 5.7 (b) and (c) also shows that a more crystalline $\text{Nd}(\text{OH})_2\text{Cl}(\text{s})$ solid phase is obtained at $T = 80^\circ\text{C}$.

No solid phase transformation occurs in hydrothermal experiments performed with $\leq 2.67 \text{ m MgCl}_2$ ($\text{pH}_m \approx 8.8$), 5.61 m NaCl ($\text{pH}_m \approx 9.3$) or 3.91 m CaCl_2 ($\text{pH}_m \approx 9.6$). Note that the transformation of $\text{Nd}(\text{OH})_3(\text{s})$ into $\text{Nd}(\text{OH})_2\text{Cl}(\text{s})$ is a function of m_{Cl^-} and pH_m (see equation (5.7)). Hence, these observations indicate that the experimental conditions in the latter experiments are beyond the thermodynamic stability of $\text{Nd}(\text{OH})_2\text{Cl}(\text{s})$. A thorough discussion of the boundary conditions for the transformation of $\text{Nd}(\text{OH})_3(\text{s})$ into $\text{Nd}(\text{OH})_2\text{Cl}(\text{s})$ is provided in section 5.2.5.2, in combination with the corresponding thermodynamic description of the system. The outcome of the transformation experiments conducted at $T = 22$ and 80°C is summarized in Table 5.4.



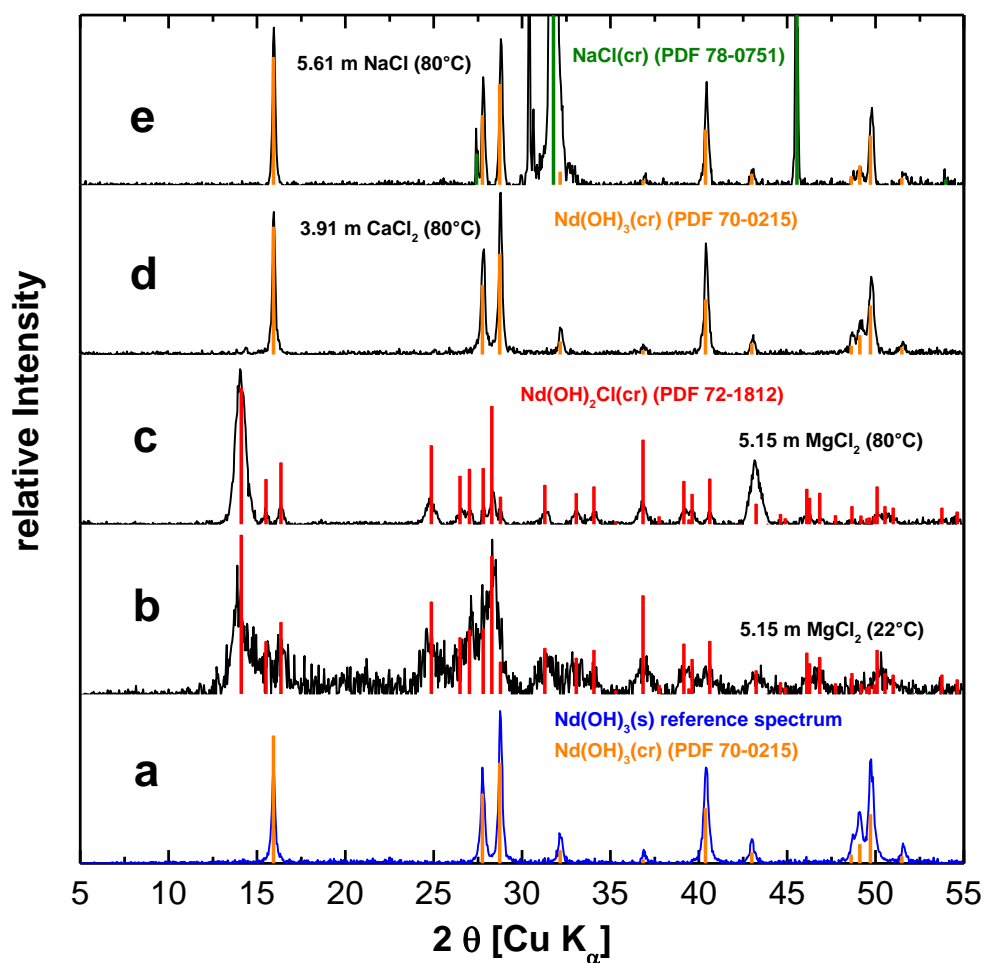


Figure 5.7: XRD patterns of $\text{Nd(OH)}_3(\text{s})$ starting material (a) and solid phases recovered from experiments in 5.15 m MgCl_2 at $T = 22^\circ\text{C}$ (b), $T = 80^\circ\text{C}$ (c) as well as solid phases recovered from experiments in 3.91 m CaCl_2 (d) and 5.61 m NaCl (e) at $T = 80^\circ\text{C}$, respectively. Reference patterns available for $\text{Nd(OH)}_3(\text{s})$ (PDF 70-0215, [BEALL *et al.*, 1976]), $\text{Nd(OH)}_2\text{Cl}(\text{s})$ (PDF 72-1812, [BUKIN, 1972]) and NaCl (PDF 78-0751, [NICKELS *et al.*, 1949]) are appended for comparison.

Table 5.4: Summary of the transformation experiments conducted in NaCl, MgCl₂ and CaCl₂ systems at $T = 22$ and 80°C . Green ticks indicate the solid phase identified by XRD upon completion of the experiment.

background electrolyte	Nd(OH) ₂ Cl(s)	Nd(OH) ₃ (s)	T [$^\circ\text{C}$]	pH _m
5.61 m NaCl		✓	80	9.3
0.25 m MgCl ₂		✓	80	pH _{max}
1.03 m MgCl ₂		✓	80	pH _{max}
2.67 m MgCl ₂		✓	80	pH _{max}
3.87 m MgCl ₂	✓		80	pH _{max}
5.15 m MgCl ₂	✓		22, 80	pH _{max}
3.91 m CaCl ₂		✓	80	9.6

5.2.2 Solubility of Nd(OH)₂Cl(s) in concentrated NaCl, MgCl₂ and CaCl₂ solutions

Figure 5.8 and Figure 5.9 show the experimental solubility data of Nd(OH)₂Cl(s) in concentrated NaCl and MgCl₂/CaCl₂ systems, respectively. Both figures also include the experimental solubility data reported in [NECK *et al.*, 2009] for Nd(OH)₃(s) in NaCl and CaCl₂ solutions under analogous pH_m and ionic strength conditions. Solubility curves of Nd(OH)₃(s) and Nd(OH)₂Cl(s), calculated with the thermodynamic and activity models reported in [NECK *et al.*, 2009] and derived in this work, are also included for comparison purposes.

Experimental solubility data determined in 5.61 m NaCl using Nd(OH)₂Cl(s) as starting material are in excellent agreement with solubility data reported in [NECK *et al.*, 2009] under analogous experimental conditions but using Nd(OH)₃(s) (Figure 5.8). This observation strongly suggests that the solid phase controlling the solubility was the same in both studies, and thus that the original Nd(OH)₂Cl(s) transformed to Nd(OH)₃(s).

The solubility curve of $\text{Nd}(\text{OH})_3(\text{s})$ calculated in 5.61 m NaCl using the thermodynamic model reported in [NECK *et al.*, 2009] clearly overestimates the experimental solubility data determined in this work within $8.5 \leq \text{pH}_m \leq 10$. Note that no experimental data were collected by Neck and co-workers within this pH-range. It is thus hypothesized that the second hydrolysis constant ($\lg^* \beta^{\circ}_{(1,2)}$) reported in [NECK *et al.*, 2009] for Nd(III) is slightly overestimated. In contrast to NaCl systems, the second hydrolysis species is slightly suppressed in MgCl_2 and CaCl_2 systems by the use of ternary Pitzer interaction parameters. The investigation of Ln(III)/An(III) hydrolysis is out of the scope of this Ph.D. thesis and is not further discussed in this chapter, although additional experimental studies are planned at KIT-INE to clarify the identified disagreements.

In contrast to the NaCl system, the solubility of $\text{Nd}(\text{OH})_2\text{Cl}(\text{s})$ in concentrated MgCl_2 and CaCl_2 systems is clearly lower (up to 1.5 lg-units) than that of $\text{Nd}(\text{OH})_3(\text{s})$ [NECK *et al.*, 2009] at $\text{pH}_m \leq 8.5$ (2.67/2.68 m $\text{MgCl}_2/\text{CaCl}_2$, Figure 5.9 a) and $\text{pH}_m \leq 9.2$ (3.91 m CaCl_2 , Figure 5.9 b). In 3.87 and 5.15 m MgCl_2 , the experimentally measured solubility of $\text{Nd}(\text{OH})_2\text{Cl}(\text{s})$ is manifestly lower than the solubility calculated for $\text{Nd}(\text{OH})_3(\text{s})$ within the complete pH-range investigated ($7.0 \leq \text{pH}_m \leq 9.0$) (Figure 5.9 b and c).

Above $\text{pH}_m \approx 8.5$ or $\text{pH}_m \approx 9.2$ (depending upon $\text{MgCl}_2/\text{CaCl}_2$ concentration), experimentally measured solubility is in good agreement with data reported in [NECK *et al.*, 2009] using $\text{Nd}(\text{OH})_3(\text{s})$. The agreement between both experimental data sets clearly indicates that the same solid phase is controlling the solubility in both systems. Furthermore, this observation is qualitatively agreeing with the expected behavior for the transformation $\text{Nd}(\text{OH})_3(\text{s}) \Leftrightarrow \text{Nd}(\text{OH})_2\text{Cl}(\text{s})$ (equation (5.7)), the former solid phase becoming more stable at higher pH_m . These findings are discussed in combination with the results of solid phase characterization in section 5.2.4.1.

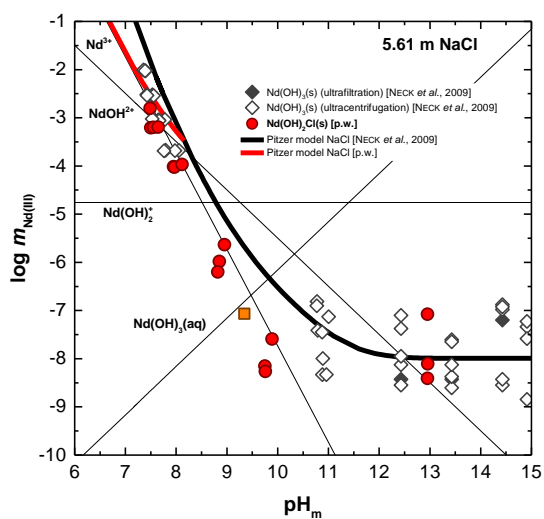


Figure 5.8: Experimentally determined solubility of Nd(III) in 5.61 m NaCl using $\text{Nd}(\text{OH})_2\text{Cl}(\text{s})$ as starting material. Previously reported solubility data of $\text{Nd}(\text{OH})_3(\text{s})$ [NECK *et al.*, 2009] are included for comparison. Thick solid lines corresponding to the solubility of $\text{Nd}(\text{OH})_3(\text{s})$ (black) and $\text{Nd}(\text{OH})_2\text{Cl}(\text{s})$ (red) calculated with thermodynamic and (Pitzer) activity models reported in [NECK *et al.*, 2009] and derived in this work, respectively. Thin lines show the aqueous speciation underlying the $\text{Nd}(\text{OH})_2\text{Cl}(\text{s})$ solubility curve in the respective system. Orange square indicates $m_{\text{Nd(III)}}$ in equilibrium with both $\text{Nd}(\text{OH})_3(\text{s})$ and $\text{Nd}(\text{OH})_2\text{Cl}(\text{s})$ (“mixing” experiment).

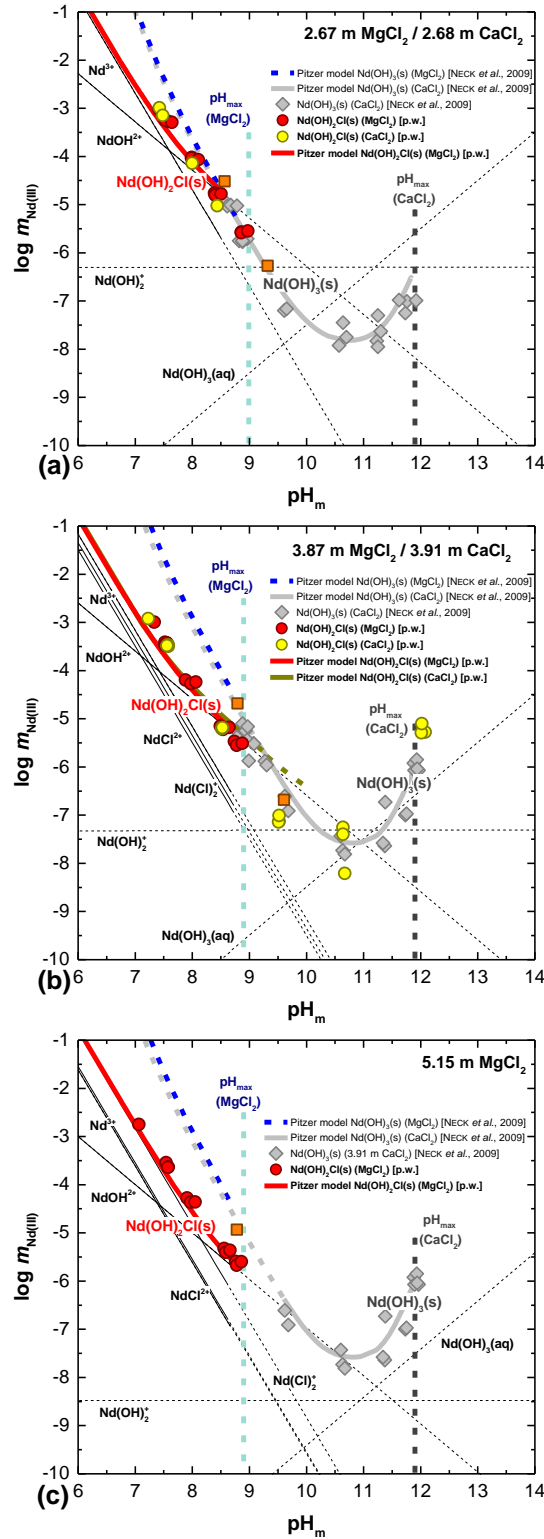


Figure 5.9: Experimentally determined solubility of Nd(III) in (a) 2.67/2.68 m MgCl₂/CaCl₂, (b) 3.87/3.91 m MgCl₂/CaCl₂ and (c) 5.15 m MgCl₂ using Nd(OH)₂Cl(s) as starting material. Previously reported solubility data of Nd(OH)₃(s) [NECK *et al.*, 2009] are included for comparison. Thick solid lines corresponding to the solubility of Nd(OH)₃(s) (pH_m > 9.2) and Nd(OH)₂Cl(s) (pH_m ≤ 9.2) calculated with thermodynamic and (Pitzer) activity models reported in [NECK *et al.*, 2009] and derived in this work, respectively. Thin lines show the aqueous speciation underlying the Nd(OH)₂Cl(s) solubility curve in the respective systems. Orange square indicates $m_{\text{Nd(III)}}$ in equilibrium with both Nd(OH)₃(s) and Nd(OH)₂Cl(s) ("mixing" experiment).

5.2.3 “Mixing” experiments in NaCl, MgCl₂ and CaCl₂ solutions

The co-existence of Nd(OH)₃(s) and Nd(OH)₂Cl(s) in the same aqueous system controls the pH_m according with the combined equilibrium reaction (5.8). The pH_m of the aqueous solution in equilibrium with both solid phases is denoted as pH_{m,mix} in the following. Based on the combined equilibrium reaction (5.8) and provided that m_{Cl^-} and $\lg^*K'_{s,0}\{\text{Nd(OH)}_3(\text{s})\}$ are known, it is possible to determine $\lg^*K'_{s,0}\{\text{Nd(OH)}_2\text{Cl}(\text{s})\}$ by only measuring pH_{m,mix} and according to equation (5.9). Note that the determination of thermodynamic data is only feasible if $\text{pH}_{\text{m,mix}} \leq \text{pH}_{\text{max}}$. This is especially relevant in the case of MgCl₂ systems, where pH_m is constrained by the precipitation of brucite/Mg-oxychloride solid phases to $\text{pH}_{\text{m}} \approx 8.7 = \text{pH}_{\text{max}}$.



$$\lg^*K'_{s,0}\{\text{Nd(OH)}_2\text{Cl}(\text{s})\} = \lg^*K'_{s,0}\{\text{Nd(OH)}_3(\text{s})\} - \text{pH}_{\text{m,mix}} + \lg m_{\text{Cl}^-} \quad (5.9)$$

Table 5.5 summarizes the values of pH_{m,mix} determined in the “mixing” experiments with concentrated NaCl (5.61 m), MgCl₂ (2.11, 2.67, 3.87, 5.15 m) and CaCl₂ (2.68, 3.91 m) solutions. Concentration of Nd(III) in equilibrium with both Nd(OH)₃(s) and Nd(OH)₂Cl(s) is plotted as orange squares in Figure 5.8 and Figure 5.9. Table 5.5 shows that greater pH_{m,mix} are obtained with increasing MgCl₂ and CaCl₂ concentration, qualitatively agreeing with the trend expected according with equation (5.9). However, this trend is not followed in the case of 2.11 m MgCl₂ and

2.67 m MgCl₂ denoting the uncertainty associated with this approach for the quantification of $\lg^*K'_{s,0}\{\text{Nd}(\text{OH})_2\text{Cl}(\text{s})\}$. Relevant discrepancies arise also between 2.67 m MgCl₂ and 2.68 m CaCl₂. Note further that pH_{m,mix} determined in 3.87 and 5.15 m MgCl₂ are \approx pH_{max}, and therefore have been disregarded in the thermodynamic interpretation of the “mixing” experiments conducted in section 5.2.5.2.

Table 5.5: Experimentally determined pH_{m,mix} values in the “mixing” experiments.

background electrolyte	pH _{m,mix}
5.61 m NaCl	9.36 ± 0.08
2.11 m MgCl ₂	8.56 ± 0.03
2.67 m MgCl ₂	8.55 ± 0.04
3.87 m MgCl ₂	8.71 ± 0.05*
5.15 m MgCl ₂	8.74 ± 0.04*
2.68 m CaCl ₂	9.27 ± 0.05
3.91 m CaCl ₂	9.53 ± 0.05

* pH_{m,mix} \approx pH_{max}

5.2.4 Solid phase characterization in NaCl, MgCl₂ and CaCl₂

5.2.4.1 Solid phases recovered from solubility experiments with Nd(OH)₂Cl(s)

In all investigated NaCl, MgCl₂ and CaCl₂ systems, the diffractograms of solid phases recovered from selected batch solubility experiments within $7 \leq \text{pH}_m \leq 13$ match the XRD pattern of the initial Nd(OH)₂Cl(s) material and are in excellent agreement with the Nd(OH)₂Cl(s) reference diffractogram reported in [BUKIN, 1972] (PDF 72-1812) (Figure 5.10). These observations appear as inconsistent with the results obtained in the solubility experiments, where the transformation of Nd(OH)₂Cl(s) into Nd(OH)₃(s) was hinted above $\text{pH}_m \approx 8.5$ in 2.67/2.68 m MgCl₂/CaCl₂ and $\text{pH}_m \approx 9.2$ in 3.87/3.91 m MgCl₂/CaCl₂. A detailed discussion on this disagreement is provided below. In addition to Nd(OH)₂Cl(s), the sharp reflections observed in the solid phase equilibrated in 5.61 m NaCl at $\text{pH}_m = 12.95$ correspond to the Ca(OH)₂(cr) used for the pH-buffering of the sample.

A number of solid phases recovered from the solubility experiments were also characterized by SEM-EDS. Figure 5.11 exemplarily shows SEM images of Nd(III) solid phases recovered from experiments in 5.61 m NaCl at $\text{pH}_m = 10$ (a) and 5.15 m MgCl₂ at $\text{pH}_m = 8.5$ (b). Figure 5.11 c and (d) shows also SEM images of the original Nd(OH)₃(s) and Nd(OH)₂Cl(s) material, respectively. All solid phases recovered from solubility experiments show a similar morphology with the presence of less regularly shaped crystals, which retain close similarities with the morphology of the original Nd(OH)₃(s) material. The less crystalline appearance of the original material is noteworthy, especially in view of its sharp XRD patterns

and the relatively large particle size calculated from the Rietveld analysis (96 ± 5 nm) [RODRIGUEZ-CARVAJAL, 1990]. Consequently, it is hypothesized that the solubility of $\text{Nd}(\text{OH})_3(\text{s})$ is not controlled by large crystalline structures resulting from the hydration of $\text{Nd}_2\text{O}_3(\text{cr})$ (see section 4.2.1), but rather by a surface layer of $\text{Nd}(\text{OH})_3(\text{am})$ growing as a coating of the bulk $\text{Nd}(\text{OH})_3(\text{cr})$ and giving the appearance of less crystalline aggregates observed by SEM.

A similar phenomena can be claimed to explain the solubility behavior of $\text{Nd}(\text{OH})_2\text{Cl}(\text{s})$ in 5.61 m NaCl over the entire investigated pH-range and in $\text{MgCl}_2/\text{CaCl}_2$ above $\text{pH}_m \approx 8.5$ or $\text{pH}_m \approx 9.2$ (depending upon concentration). As described in section 5.2.2, the solubility of Nd(III) in these systems/pH-regions follows the behavior of $\text{Nd}(\text{OH})_3(\text{s})$, although XRD patterns confirm both the presence of $\text{Nd}(\text{OH})_2\text{Cl}(\text{s})$ and the absence of crystalline $\text{Nd}(\text{OH})_3(\text{s})$. Hence, the formation of a coating of $\text{Nd}(\text{OH})_3(\text{am})$ on the surface of $\text{Nd}(\text{OH})_2\text{Cl}(\text{s})$ would be consistent with observations gained by both solubility and XRD. The lack of sharp diffraction patterns corresponding to $\text{Nd}(\text{OH})_3(\text{cr})$ is attributed to the different source of $\text{Nd}(\text{OH})_3(\text{s})$, which in this case has not been formed from the hydration of $\text{Nd}_2\text{O}_3(\text{cr})$.

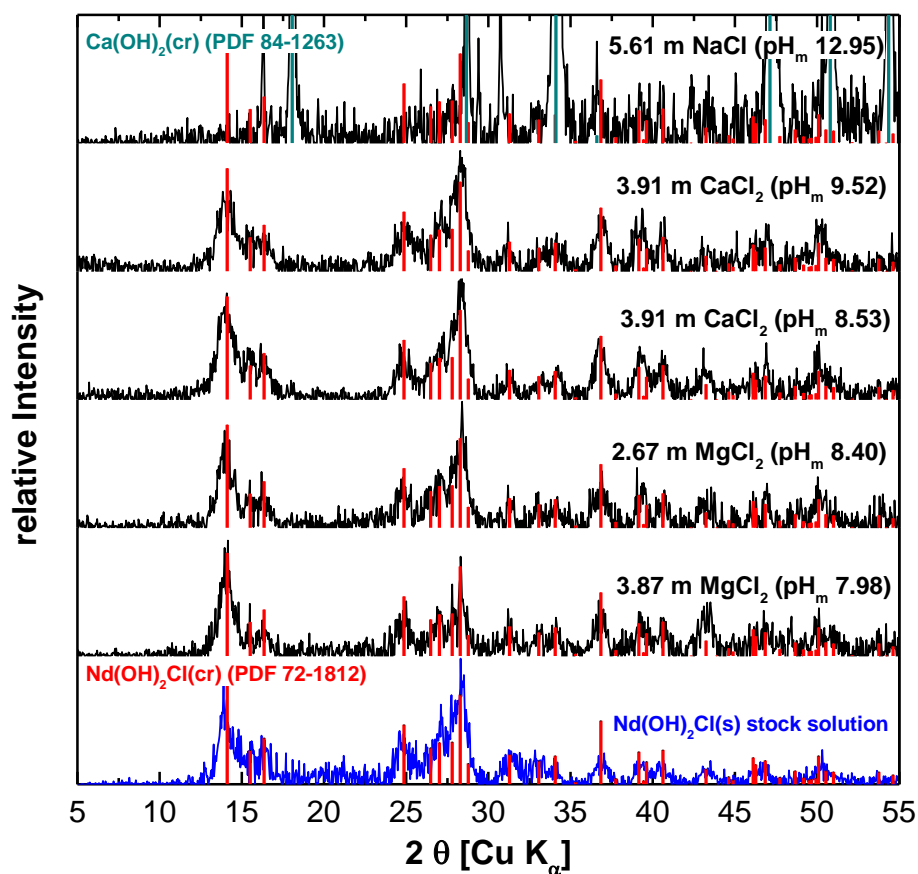


Figure 5.10: XRD patterns of Nd(III) solid phases recovered from batch solubility experiments after > 225 days in comparison with the initial Nd(OH)₂Cl(s) material (blue) synthesized at $T = 22^{\circ}\text{C}$. Reference patterns available for Nd(OH)₂Cl(s) (PDF 72-1812, [BUKIN, 1972]) and Ca(OH)₂(cr) (PDF 84-1263, [CHAIX-PLUCHERY *et al.*, 1987]) are appended for comparison.

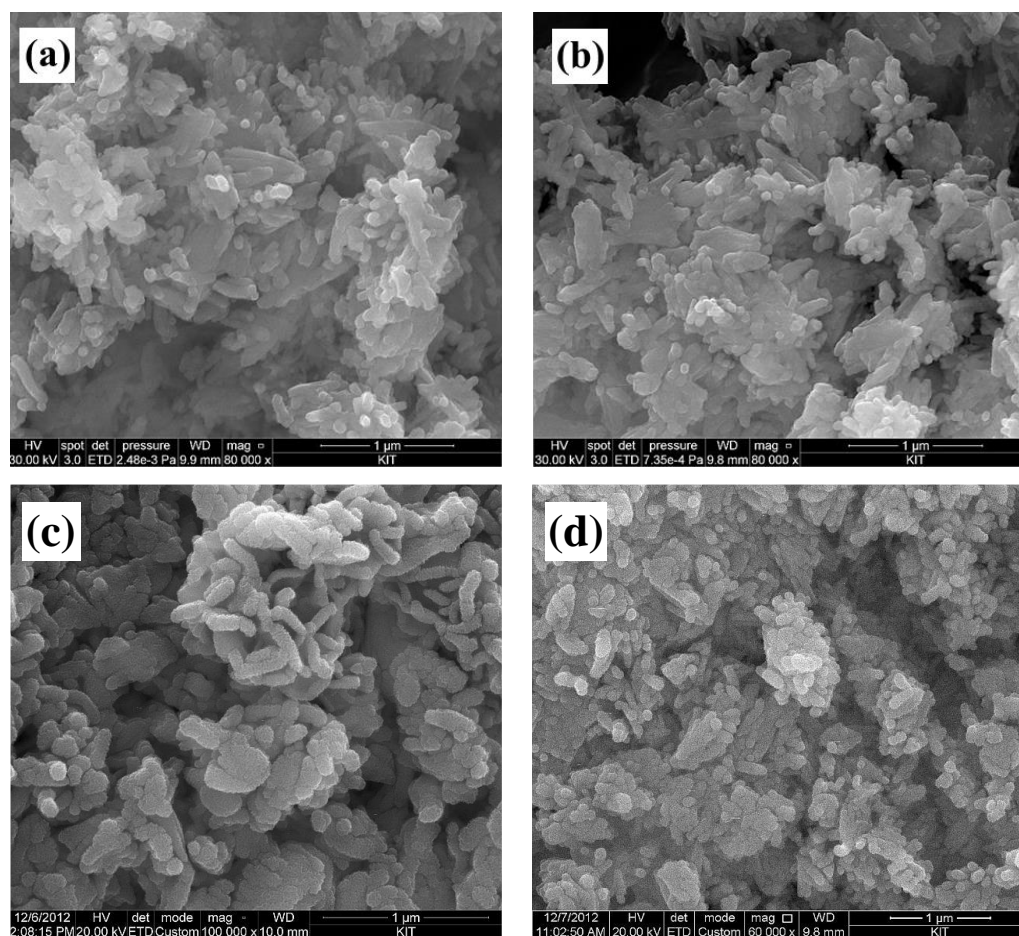


Figure 5.11: SEM images of solid phases recovered from batch solubility experiments using $\text{Nd}(\text{OH})_2\text{Cl}(\text{s})$ as starting material in (a) 5.61 m NaCl at $\text{pH}_m = 10$ and in (b) 5.15 m MgCl_2 at $\text{pH}_m = 8.5$. The original $\text{Nd}(\text{OH})_3(\text{s})$ and $\text{Nd}(\text{OH})_2\text{Cl}(\text{s})$ materials are shown in SEM images (c) and (d), respectively.

5.2.4.2 Solid phases recovered from “mixing” experiments with $\text{Nd}(\text{OH})_3(\text{s})$ and $\text{Nd}(\text{OH})_2\text{Cl}(\text{s})$

Figure 5.12 shows the diffractograms of solid phases recovered from “mixing” experiments in concentrated NaCl, MgCl_2 and CaCl_2 solutions. In all cases, the

XRD patterns confirm the presence of both $\text{Nd}(\text{OH})_2\text{Cl}(\text{s})$ and $\text{Nd}(\text{OH})_3(\text{s})$, in good agreement with $\text{Nd}(\text{OH})_3(\text{s})$ (PDF 70-0215, [BEALL *et al.*, 1976]) and $\text{Nd}(\text{OH})_2\text{Cl}(\text{s})$ (PDF 72-1812, [BUKIN, 1972]) reference data.

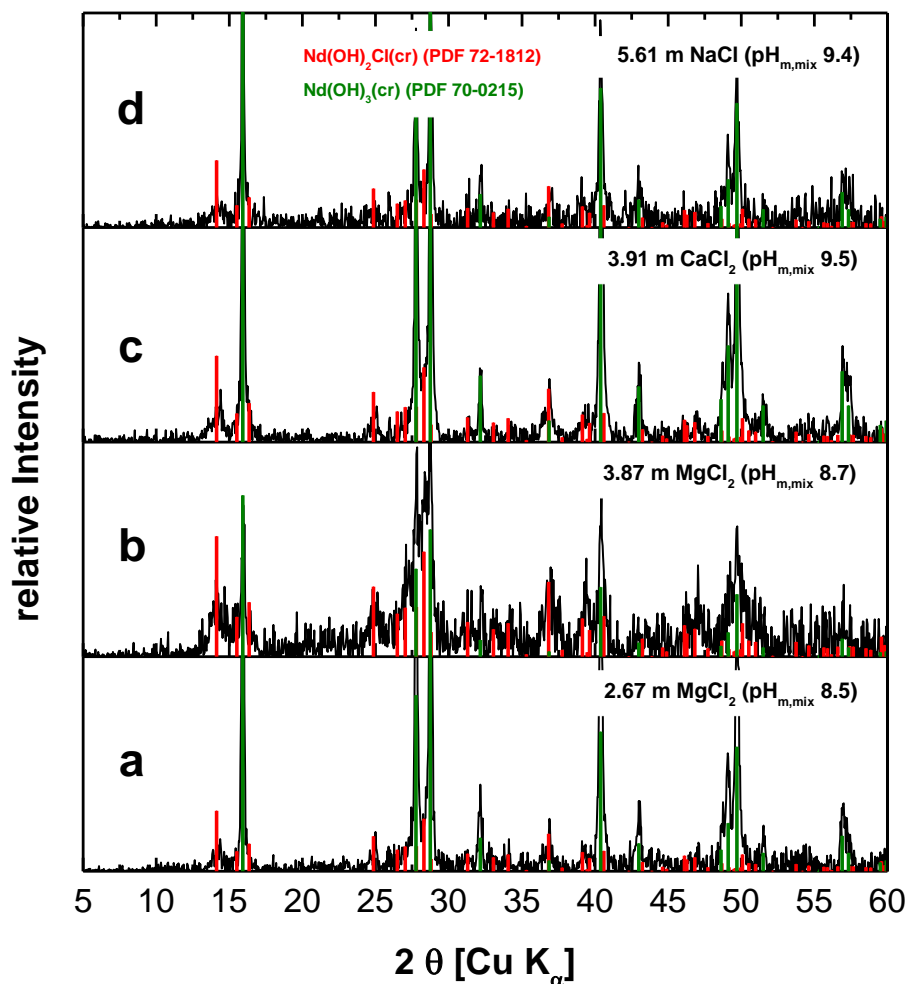


Figure 5.12: XRD patterns of Nd(III) solid phases recovered from “mixing” experiments performed with $\text{Nd}(\text{OH})_3(\text{s})$ and $\text{Nd}(\text{OH})_2\text{Cl}(\text{s})$. Reference patterns available for $\text{Nd}(\text{OH})_3(\text{s})$ (PDF 70-0215, [BEALL *et al.*, 1976]) and $\text{Nd}(\text{OH})_2\text{Cl}(\text{s})$ (PDF 72-1812, [BUKIN, 1972]) are appended for comparison.

5.2.5 Chemical and thermodynamic models

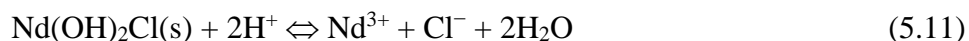
Due to the very high ionic strength in most of the evaluated systems ($I_m \geq 8.01$ m), the Pitzer formalism has been preferred for the thermodynamic modelling (section 2.4.2). Parameters reported in [HARVIE *et al.*, 1984; PITZER, 1991] are used for the calculation of a_w and the activity coefficients of Mg^{2+} , Ca^{2+} , Cl^- and H^+ . Pitzer ion interaction coefficients for Nd(III) aqueous species derived in chloride media are reported in [NECK *et al.*, 2009]. Two different approaches for the determination of $lg^*K_{s,0}^\circ$ were applied in this work. In the first approach, the combination of the experimental Nd(III) solubility data, determined in $MgCl_2$ and $CaCl_2$ solutions, with the corresponding thermodynamic and Pitzer activity models derived in [NECK *et al.*, 2009] for Ln(III) and An(III) aqueous species allows the quantification of $lg^*K_{s,0}^\circ$ for $Nd(OH)_2Cl(s)$. In the second method, $lg^*K_{s,0}^\circ\{Nd(OH)_2Cl(s)\}$ was derived from the extrapolation of $lg^*K'_{s,0}\{Nd(OH)_2Cl(s)\}$, obtained from the “mixing” experiments, to zero ionic strength.

5.2.5.1 Determination of $lg^*K_{s,0}^\circ\{Nd(OH)_2Cl(s)\}$ from solubility experiments

Only solubility data obtained under experimental conditions where $Nd(OH)_2Cl(s)$ controls the solubility of Nd(III) (see sections 5.2.2 and 5.2.4) are used in this section to determine $lg^*K_{s,0}^\circ\{Nd(OH)_2Cl(s)\}$. Hence, solubility data at $pH_m \geq 8.5$ (2.67/2.68 m $MgCl_2/CaCl_2$) and $pH_m \geq 9.2$ (3.91 m $CaCl_2$) have been disregarded in the modelling exercise described in the following.

Slope analysis ($lg m_{Nd(III)}$ vs. pH_m) of the experimental solubility data indicates the release of one (slope -1) and two (slope -2) H^+ in the equilibrium reaction

controlling the solubility of Nd(III) in the investigated pH-region. Providing the solubility control by Nd(OH)₂Cl(s), as confirmed by XRD and SEM-EDS, equilibrium reactions (5.10) and (5.11) can be defined.



The coupling of this chemical model with the thermodynamic and activity models reported in [NECK *et al.*, 2009] for Nd(III) aqueous species allows the determination of $\lg^*K_{s,0}^\circ\{\text{Nd(OH)}_2\text{Cl(s)}\}$ by minimizing the difference between experimental and calculated solubility data in 2.11–5.15 m MgCl₂ and 2.68/3.91 m CaCl₂ systems. The resulting value ($\lg^*K_{s,0}^\circ = 10.56 \pm 0.10$) has been used in Figure 5.8 and Figure 5.9 to calculate the solubility of Nd(III) in concentrated NaCl and MgCl₂/CaCl₂ systems, respectively. Figure 5.9 shows that $\lg^*K_{s,0}^\circ\{\text{Nd(OH)}_2\text{Cl(s)}\}$ derived in this work perfectly explains experimental observations obtained in concentrated MgCl₂ and CaCl₂ solutions. In 5.61 m NaCl, the model predicts a solubility control of Nd(OH)₂Cl(s) only below $\text{pH}_m \approx 8$. Although experimental solubility data under near-neutral pH conditions were also gained for this system ($\text{pH}_m \approx 7.5$ and 7.6), the experimental uncertainties as well as the minor differences between the calculated solubility for Nd(OH)₂Cl(s) and Nd(OH)₃(s) do not allow a definitive prediction of the relevance of the former solid phase under these boundary conditions.

5.2.5.2 Inputs from “mixing” experiments

“Mixing” experiments performed in 5.61 m NaCl, 2.11/2.67 m MgCl₂ and 2.68/3.91 m CaCl₂ were used for the determination of $\lg^*K_{s,0}^{\circ}\{\text{Nd}(\text{OH})_2\text{Cl}(\text{s})\}$. $\text{pH}_{\text{m,mix}}$ values obtained in 3.87/5.15 m MgCl₂ systems were disregarded in this section due to the limitation of pH_{m} in the MgCl₂ systems ($\text{pH}_{\text{m,mix}} \leq \text{pH}_{\text{max}}$, see section 5.2.3).

As discussed in section 5.2.3 and according to equation (5.9), $\lg^*K_{s,0}^{\circ}\{\text{Nd}(\text{OH})_2\text{Cl}(\text{s})\}$ can be calculated by measuring $\text{pH}_{\text{m,mix}}$ in the respective system if m_{Cl^-} and $\lg^*K_{s,0}^{\circ}\{\text{Nd}(\text{OH})_3(\text{s})\}$ are known. The unweighted average of the conditional constants calculated for the above mentioned systems can be extrapolated to $I_{\text{m}} = 0$ using the Pitzer activity model reported for Nd(III) in [NECK *et al.*, 2009]. The resulting value ($\lg^*K_{s,0}^{\circ}\{\text{Nd}(\text{OH})_2\text{Cl}(\text{s})\} = 9.93 \pm 1.24$) agrees within the uncertainty with $\lg^*K_{s,0}^{\circ}\{\text{Nd}(\text{OH})_2\text{Cl}(\text{s})\}$ determined from solubility experiments in concentrated MgCl₂ and CaCl₂ solutions. The latter value is favored in the present work due to the greater accuracy of the experimental approach, the significantly larger data set available (only five experimental points considered in the “mixing” experiments), as well as the fact that the solubility of Nd(III) follows the behavior of Nd(OH)₃(s) over the entire investigated pH range in 5.61 m NaCl and above $\text{pH}_{\text{m}} = 8.5$ in 2.68 m and $\text{pH}_{\text{m}} = 9.2$ in 3.91 m CaCl₂ solutions (see also section 5.2.2).

5.2.5.3 Understanding the transformation of $\text{Nd}(\text{OH})_3(\text{s})$ into $\text{Nd}(\text{OH})_2\text{Cl}(\text{s})$

The combination of solubility and “mixing” experiments sets the basis for deriving sound chemical and thermodynamic models for Nd(III) in concentrated NaCl, MgCl_2 and CaCl_2 solutions, and provides key inputs for the understanding of the transformation of $\text{Nd}(\text{OH})_3(\text{s})$ into $\text{Nd}(\text{OH})_2\text{Cl}(\text{s})$.

Hence, Figure 5.13 shows the thermodynamic model for $\text{Nd}(\text{OH})_2\text{Cl}(\text{s})$ derived in this work together with the solubility of $\text{Nd}(\text{OH})_3(\text{s})$ calculated according with [NECK *et al.*, 2009] in 2.67/2.68 m $\text{MgCl}_2/\text{CaCl}_2$ (a) and 3.87/3.91 m $\text{MgCl}_2/\text{CaCl}_2$ (b). The blue star in Figure 5.13 a indicates the pH_m ($\approx 8.8 = \text{pH}_{\text{max}}$) in the autoclave experiment performed in 2.67 m MgCl_2 . The figures show that pH_m in the autoclave experiment was above the calculated $\text{pH}_{m,\text{mix}}$ (≈ 8.5 , black circle in Figure 5.13 a), and hence beyond the thermodynamic stability of $\text{Nd}(\text{OH})_2\text{Cl}(\text{s})$ in 2.67 m MgCl_2 . The observation is further supported by the solubility data, where the solubility of Nd(III) follows the behavior of $\text{Nd}(\text{OH})_3(\text{s})$ above $\text{pH}_m = 8.5$ in 2.67 m MgCl_2 (cf. Figure 5.9 a). For systems in < 2.67 m MgCl_2 , the calculated $\text{pH}_{m,\text{mix}}$ is even lower and therefore the stability field of $\text{Nd}(\text{OH})_2\text{Cl}(\text{s})$ is significantly smaller.

A similar outcome arises for the system 3.91 m CaCl_2 in Figure 5.13 b, where the $\text{pH}_m = 9.6$ (red star) in the autoclave experiment was again slightly above the calculated $\text{pH}_{m,\text{mix}} = 9.5$ (black circle in Figure 5.13 b), and thus beyond the thermodynamic stability of $\text{Nd}(\text{OH})_2\text{Cl}(\text{s})$. This observation is further supported by the solubility experiment, where $m_{\text{Nd(III)}}$ above $\text{pH}_m = 9.2$ perfectly agrees with experimental and calculated solubility of $\text{Nd}(\text{OH})_3(\text{s})$ (cf. Figure 5.9 b).

On the other hand, the calculated $\text{pH}_{m,\text{mix}}$ falls below pH_{max} for ≥ 3.87 m MgCl_2 systems (green star in Figure 5.13 b) and consequently $\text{Nd}(\text{OH})_2\text{Cl}(\text{s})$ is predicted as the stable Nd(III) solid phase over the entire pH-range in these MgCl_2 systems.

These results highlight the key role of both m_{Cl^-} and pH_m in the process of solid phase transformation.

In the case of autoclave experiment in 5.61 m NaCl, the $\text{pH}_m \approx 9.4$ is clearly above the calculated $\text{pH}_{m,\text{mix}} = 8.1$, thus preventing the transformation of $\text{Nd}(\text{OH})_3(\text{s})$ into $\text{Nd}(\text{OH})_2\text{Cl}(\text{s})$. This finding is also supported by the solubility data, where the $m_{\text{Nd(III)}}$ agrees very well with the experimental and calculated solubility of $\text{Nd}(\text{OH})_3(\text{s})$ over the entire investigated pH-range (see Figure 5.8).

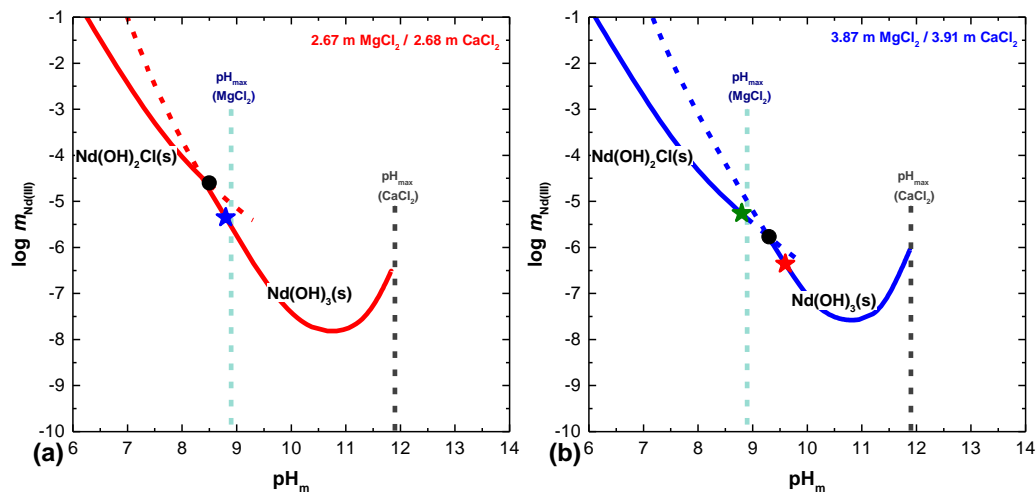


Figure 5.13: Solubility of $\text{Nd}(\text{OH})_2\text{Cl}(\text{s})$ and $\text{Nd}(\text{OH})_3(\text{s})$ in 2.67/2.68 m $\text{MgCl}_2/\text{CaCl}_2$ (a) and 3.87/3.91 m $\text{MgCl}_2/\text{CaCl}_2$ (b) as calculated with the Pitzer models reported for $\text{Nd}(\text{OH})_3(\text{s})$ and $\text{Nd}(\text{OH})_2\text{Cl}(\text{s})$ in [NECK *et al.*, 2009] and in the present work, respectively. The blue, green and red stars indicate the pH_m in the autoclave experiments performed in the respective systems and the black circle indicate the calculated $\text{pH}_{m,\text{mix}}$ in 2.68 m MgCl_2 and 3.91 m CaCl_2 .

5.2.6 Conclusions regarding mixed Nd–OH–Cl(s) phases

The formation and stability of $\text{Nd}(\text{OH})_2\text{Cl}(\text{s})$ was investigated in dilute to concentrated NaCl , MgCl_2 and CaCl_2 solutions using room temperature ($T = 22 \pm 2^\circ\text{C}$) and hydrothermal preparation experiments ($T = 80 \pm 3^\circ\text{C}$). Thermodynamic properties of this solid phase were derived from batch solubility experiments complemented by “mixing” experiments and extensive solid phase characterization (XRD, SEM-EDS).

Solid phase transformation of $\text{Nd}(\text{OH})_3(\text{s})$ into $\text{Nd}(\text{OH})_2\text{Cl}(\text{s})$ was found to occur both at $T = 22$ and 80°C in $\geq 3.87\text{ m}$ MgCl_2 and at $\text{pH}_m \leq \text{pH}_{\text{max}}$. Although kinetically slow, the transformation is enhanced by temperature, high m_{Cl^-} ($\geq 5.34\text{ m}$) and pH_m values lower than ≈ 9 .

The comparison of $\text{Nd}(\text{OH})_2\text{Cl}(\text{s})$ and $\text{Nd}(\text{OH})_3(\text{s})$ solubility under virtually the same experimental conditions (present work and [NECK *et al.*, 2009]) shows significantly lower Nd(III) concentrations (up to 1.5 lg-units) in equilibrium with $\text{Nd}(\text{OH})_2\text{Cl}(\text{s})$ in 2.11–2.67 m MgCl_2 and 2.68 m CaCl_2 and $\text{pH}_m \leq 8.5$, over the entire investigated pH-range in 3.87/5.15 m MgCl_2 and in 3.91 m CaCl_2 solutions and $\text{pH}_m \leq 9.2$. On the contrary, no differences in $m_{\text{Nd(III)}}$ are observed in 5.61 m NaCl within the investigated pH-range, indicating, that $\text{Nd}(\text{OH})_2\text{Cl}(\text{s})$ has no (or only very minor) stability field under these conditions.

Based on the combination of experimental solubility data, solid phase characterization and the Pitzer activity model reported in [NECK *et al.*, 2009], $\lg^*K_{\text{s},0}^\circ\{\text{Nd}(\text{OH})_2\text{Cl}(\text{s})\} = 10.56 \pm 0.10$ has been determined in the present work. The resulting value is in good agreement with the results gained in “mixing” experiments with $\text{Nd}(\text{OH})_3(\text{s})$ and $\text{Nd}(\text{OH})_2\text{Cl}(\text{s})$ in MgCl_2 solutions.

This is the first comprehensive experimental study providing a sound understanding of the formation, stability and solubility of $\text{Nd}(\text{OH})_2\text{Cl}(\text{s})$ in dilute to concentrated NaCl , MgCl_2 and CaCl_2 solutions over a broad range of pH_m and I_m conditions. The results demonstrate that $\text{Nd}(\text{OH})_2\text{Cl}(\text{s})$ can play a relevant role in controlling the solubility of $\text{An}^{\text{III}}/\text{Ln}^{\text{III}}$ in repository systems with high chloride concentrations, e.g. disposal in rock-salt formations. This experimental observation also implies that the use of $\text{Nd}(\text{OH})_3(\text{s})$ as solubility-controlling solid phase for $\text{An}^{\text{III}}/\text{Ln}^{\text{III}}$ in source term estimations for a safety analysis of a deep geological repository for nuclear waste disposal is a conservative upper limit.

5.3 Determination of C-14 and other activation/fission products in Zircaloy-4 cladding from an irradiated UO_2 fuel rod segment

C-14 is one of the crucial radionuclides with respect to estimated doses arising from the release in a repository for nuclear waste to the environment in a canister failure scenario due to its long half-life and assumed mobility. However, C-14 is a difficult radionuclide to measure (soft β^- -emitter and has no γ -rays). Therefore, it requires an elaborate and robust extraction and analysis technique.

In the present study, the amount and chemical form of C-14 as well as the inventories of Fe-55, Sb-125 and Cs-137 are determined in Zircaloy-4 cladding from an irradiated UO_2 fuel rod segment.

Experimentally measured radionuclide contents are compared to the theoretically predicted inventory of the Zircaloy-4 obtained by means of MCNP-X calculations.

5.3.1 Chemical yield of the separation technique

Recovery tests, performed with C-14 labelled sodium carbonate, acetic and formic acid (sodium salts) reference material with about 10 to 1000 Bq for the inorganic and organic compounds respectively, indicate that the chemical yield of the separation method is well above 90% for the inorganic ($99.8 \pm 8.7\%$) and the organic ($92.7 \pm 6.7\%$) C-14 fraction (see Table 5.6). In addition, different ratios of activity between the carbonate and the hydrocarbons were tested and no cross contamination of e.g. organic C-14 bearing compounds in the first set of alkaline washing bottles (inorganic fraction) was seen.

Tests including other radionuclides (e.g. 2800 Bq HTO, 1845 Bq Na^{36}Cl and 1850 Bq Na^{129}I), solely or in combination with C-14 bearing reference material, show that about 98–99% of the H-3, Cl-36 and I-129 bearing compounds remain in the glass reactor used for the extraction of C-14 in aqueous samples (see section 4.6.3). About 1–2% of H-3 added as HTO is mobilized from the glass reactor during the C-14 recovery procedure and absorbed in the first tritium trap (see Figure 4.9, page - 65 -, washing bottle #2). The same is true for I-129, where about 1–2% of the added Na^{129}I is also mobilized from the flask during the extraction and absorbed in the iodine trap (see Figure 4.9, page - 65 -, washing bottle #1). In contrast Cl-36 added as Na^{36}Cl is only found in the glass reactor. Neither a contamination of the alkaline washing bottles (see Figure 4.9, page - 65 -, washing bottles #3/#4 and #7/#8) by those radionuclides is seen in the recovery tests nor is the chemical yield of the C-14 recovery affected by these other radionuclides.

Blank tests (including the addition of all chemicals but without radionuclides) performed for the whole C-14 extraction set-up and procedure show a typical background of one to four cpm in LSC measurements and is virtually the same as the typical background obtained for those measurements (cf. section 4.5.1). In addition, recovery tests and blank tests containing non-irradiated Zircaloy

(140 ± 30 mg) show no impact on the chemical yield of the separation procedure and background for the LSC measurements.

The oxidation efficiency of the catalytic furnace was tested using a mixture of 10% methane and 90% argon with a yield of about 99% for the conversion of methane into carbon dioxide.

The tests performed with and without radionuclide reference material and non-irradiated Zircaloy demonstrate the effectiveness and robustness of the complete method which consists of the extraction of C-14 from other radionuclides in highly activated samples, the conversion of inorganic/organic carbon bearing compounds into $^{14}\text{CO}_2/\text{CO}_2$ and its absorption in specific C-14 traps, as well as the analysis of C-14 and other radionuclides in the obtained fractions.

Table 5.6: Results of recovery tests performed with C-14 labelled compounds.

added C-14 component	added activity [Bq] ($\pm 5\%$)	recovery of [Bq]		recovery of [%]	
		C-14 (inorg.) ($\pm 5\%$)	C-14 (org.) ($\pm 5\%$)	C-14 (inorg.) ($\pm 5\%$)	C-14 (org.) ($\pm 5\%$)
inorganic C-14					
test 1	987.3	964.4	–	97.7	–
test 2	983.9	855.0	–	86.9	–
test 3	932.1	801.8	–	86.0	–
organic C-14					
test 4	1121.8	–	1036.2	–	92.4
test 5	882.0	–	756.0	–	85.7
test 6	10.9	–	10.6	–	96.4
test 7	1142.2	–	1086.3	–	95.1
mixtures*					
test 8	71.5 + 84.0	74.7	67.5	104.5	80.4
test 9	74.3 + 88.3	70.6	79.7	95.1	90.3
test 10	74.8 + 87.8	60.0	69.4	80.2	79.1
test 11	85.4 + 114.7	90.6	110.3	106.1	96.2
test 12	83.2 + 111.3	86.5	109.9	104.0	98.7
test 13	80.7 + 114.4	79.9	109.8	99.0	96.1
test 14	6.0 + 10.6	6.2	10.8	102.5	101.9
test 15	8.2 + 12.2	8.9	10.7	108.1	87.4
test 16	8.1 + 10.9	8.7	10.9	107.0	99.7
test 17	8.0 + 10.7	8.7	10.8	108.1	101.3
test 18	88.3 + 108.8	89.6	98.9	101.5	90.9
test 19	84.6 + 110.2	92.9	103.3	109.8	93.8
test 20	955.1 + 1082.4	961.2	984.7	100.6	91.0
Mean \pm SD				99.8 \pm 8.7	92.7 \pm 6.7

* mixtures: inorganic C-14 + organic C-14 compounds

5.3.2 Optical examination of the Zircaloy-4 and precipitations on the inner cladding surface

The optical examination of the cut Zircaloy-4 samples under the microscope available in the shielded box-line shows black/blueish precipitates on the inner surface of the cladding (see Figure 5.14). Similar precipitates were observed on the inner surface of claddings consisting of cesium, among other fission products

[GÖTZMANN *et al.*, 1974; GÖTZMANN, 1979, 1982; SIDKY, 1998; VISWANATHAN, 2014]. Volatile cesium is released during reactor operation from subjacent UO₂/MOX pellets and precipitates on the cooler inner surface of the cladding. The precipitates contribute to clad corrosion, which limits the life of a fuel assembly at high burn-up, among other factors [VISWANATHAN, 2014]. Viswanathan reported that post irradiation examinations of claddings showed crack or penetration of the cladding up to one third of the tube thickness [VISWANATHAN, 2014]. Moreover, clad corrosion possibly has important implications for the long-term interim storage of SNF. If the cladding fails during the long-term storage, radionuclides could get released e.g. during loading/unloading of the spent fuel assemblies from the interim storage cask to the final disposal cask. The determination of the radionuclide inventory and chemical composition of the precipitates were out of scope of this Ph.D. thesis.



Figure 5.14: Black/blueish precipitates seen on the inner surface of the irradiated Zircaloy-4 cladding.

5.3.3 Improvement of the digestion experiments

The digestion experiment conducted with sample #5, performed in a glass beaker without stirring, purging or heating the solution (see Figure 4.17 a), showed that the

Results and Discussion

oxide layer of the Zircaloy-4 remains physically intact whereas the base metal was completely digested at room temperature within one hour. The thickness of the remaining ZrO_2 is about 5–10 μm , which is in good accordance with oxide layer thickness measurements performed for the fuel rod segment N0204 [WEGEN *et al.*, 2012b]. Wegen *et al.* determined an oxide thickness of $\leq 17 \mu\text{m}$ at the top end of the fuel rod segment but still below the plenum of the rod, where the Zircaloy specimens used in the present work were obtained from.

However, in order to determine the radionuclide inventory, a digestion of the whole specimen is necessary (the oxide layer also contains e.g. C-14, see section 3.1). Therefore, the Zircaloy dissolution and C-14 extraction procedure was extended by one hour and the ZrO_2 successfully dissolved (slowly). In addition, the samples were stirred, which shreds completely the oxide layer.

The oxide remnant of sample #5 was analysed by SEM-EDS, and the chemical analysis is shown in Figure 5.15. The atomic Zr:O ratio was determined to 1.79 ± 0.09 .

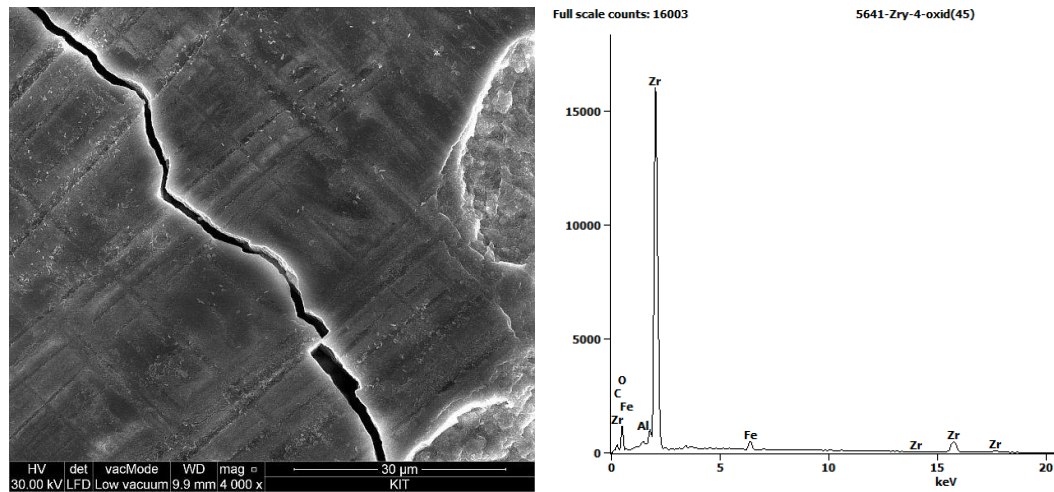


Figure 5.15: Exemplary SEM image and chemical analysis of the irradiated ZrO_2 .

5.3.4 Improvement of the separation technique

Digestion of irradiated Zircaloy-4 releases quantitatively tritium as gaseous HT as described in [NEEB, 1997]. Other than HTO, large amounts of gaseous HT released from irradiated Zircaloy passes through the first four washing bottles (#1 to #4, see Figure 4.9, page - 65 -) unaffectedly and are oxidized in the catalytic furnace to HTO. The HTO is then absorbed in the alkaline washing bottles #7 and #8, after the furnace, (see Figure 4.9, page - 65 -) and disturbs substantially the quantification of C-14 present in these washing bottles. Therefore, two additional tritium traps were implemented after the furnace in the C-14 extraction set-up.

Figure 5.16a shows the LSC spectrum for washing bottle #7 (alkaline washing bottle for trapping “organic” C-14, see Figure 4.9) with only one tritium trap (washing bottle #2, see Figure 4.9). Since HT passes through the first four washing bottles unaffectedly, the vast amount of HT is oxidized in the catalytic furnace and absorbed in the alkaline washing bottles, especially bottle #7. A significant improvement is the installation of a second tritium trap (washing bottle #5, see Figure 4.9). This trap is situated directly after the furnace and traps the majority of tritium. But still a tritium peak is visible in the LSC spectrum (cf. Figure 5.16a and Figure 5.16b). Finally, a third tritium trap was installed after the furnace (washing bottle #6, see Figure 4.9) and as a result the LSC spectrum shown in Figure 5.16c was obtained for washing bottle #7. Figure 5.16c shows a single peak attributed only to C-14. Nevertheless, a minor contribution of tritium cannot be ruled out and therefore only the channels 350 to 600 (energy window) are used for the evaluation of the C-14 concentration in the washing bottles (area between the red and the green vertical line in Figure 5.16). By doing this, a contribution of tritium to the C-14 concentration can be excluded.

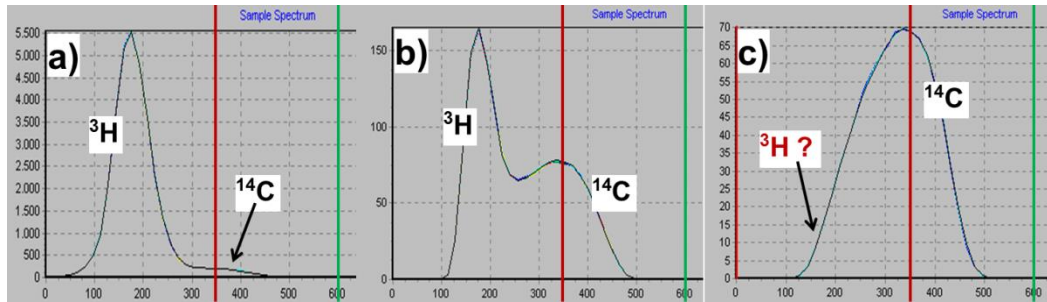


Figure 5.16: LSC spectra obtained from alkaline washing bottle #7 of the C-14 extraction and analysis system. Figure a) shows the LSC spectrum obtained for washing bottle #7 and only one tritium trap (washing bottle #2, see Figure 4.9). Whereas Figure b) shows the LSC spectrum obtained for washing bottle #7 and two tritium traps (washing bottles #2 and #5, see Figure 4.9). Finally the outcome of LSC measurements of washing bottle #7 and three tritium traps (washing bottles #2, #5 and #6, see Figure 4.9) is shown in figure c).

5.3.5 Results of experimental inventory analysis of irradiated Zircaloy-4 and chemical form of C-14 released from the studied cladding

Table 5.7 shows the results of the experimental inventory analysis obtained for each of the six Zircaloy-4 specimens. The experimentally determined activities of C-14, Fe-55, Sb-125 and Cs-137 for each sample are in good agreement among themselves within the analytical uncertainty. The results demonstrate the reliability of the C-14 extraction and analysis method for both Zircaloy dissolution approaches (glass reactor/autoclave) used in this work.

Mean values of the experimentally determined inventories of C-14, Fe-55, Cs-137 and Sb-125 are summarized in Table 5.8. These were further compared to the MCNP-X inventory calculations performed in the present study. Additionally, the C-14 inventory was compared to Zircaloy-4 hull specimens studied by [YAMAGUCHI *et al.*, 1999] (see also section 3.1). The experimental results obtained

in this study for the inventory of C-14, Fe-55 and Sb-125 are in very good agreement with the MCNP-X calculations within the uncertainties. The experimental C-14 inventory exceeds the calculated value only by a factor of 1.2. In contrast, the experimental C-14 inventory in irradiated stainless steel, recently assessed by [SCHUMANN *et al.*, 2014], exceeds the calculated by a factor of four. Moreover, the C-14 inventory is in good agreement with data of a similar PWR fuel rod hull specimen studied by [YAMAGUCHI *et al.*, 1999].

The C-14 inventory of Zircaloy-2 reported by Bleier *et al.* [BLEIER *et al.*, 1984; BLEIER *et al.*, 1987; BLEIER *et al.*, 1988] (see section 3.1) is slightly higher than that of Zircaloy-4, although the average burn-up of the PWR fuel rod (35.7 GWd/t_{HM} in 3 cycles and 882 effective full power days) is much higher than that of the BWR fuel rod (22.4 GWd/t_{HM} in 2 cycles and 804 effective full power days). In addition, the reported N-14 impurity of the PWR fuel rod (manufacturer analysis: 46–47 ppm) is also slightly higher than that of the BWR fuel rod (manufacturer analysis: 39–42 ppm). In consequence, the C-14 inventories of Zircaloy-2 and Zircaloy-4 reported by Bleier *et al.* are contradictory among themselves, considering that the C-14 inventory mainly depends on the N-14 content in Zircaloy and the burn-up history of the respective fuel rod, and possibly indicate analytical problems or experimental shortcomings.

Further, the calculations performed by Bleier *et al.* [BLEIER *et al.*, 1984; BLEIER *et al.*, 1988] regarding the C-14 inventories in BWR claddings are in clear contrast to the C-14 inventories calculated by the same authors for PWR claddings. At the same burn-up and N-14 content of the Zircaloy-2 and Zircaloy-4, the theoretically predicted inventory of C-14 in Zircaloy-2 exceeds that of Zircaloy-4 by a factor up to 2.4 (240%). However, no significant difference between the cladding of a BWR and PWR is expected regarding the C-14 inventory at the same burn-up and N-14 content [GRAS, 2014].

Results and Discussion

In contrast, the experimental Cs-137 inventory exceeds by a factor of 117 the calculated value². The excess of Cs-137 is related to the precipitation of Cs-137 on the inner Zircaloy-4 surface, which was released during reactor operation from subjacent UO₂ pellets (see section 5.3.2). The additional Cs-137 inventory is not taken into account in the MCNP-X calculation, since the neutronic simulation does not include the migration of volatile elements.

Table 5.7: Results from LSC and γ -measurements obtained from the six Zircaloy-4 specimens.

sample no.	total C-14 [Bq/g Zry-4]	Fe-55 [Bq/g Zry-4]	Cs-137 [Bq/g Zry-4]	Sb-125 [Bq/g Zry-4]
#1	$3.9(\pm 0.4)\times 10^4$	$1.3(\pm 0.1)\times 10^5$	$3.7(\pm 0.2)\times 10^6$	$2.6(\pm 0.1)\times 10^5$
#2	$4.2(\pm 0.4)\times 10^4$	ND*	$3.2(\pm 0.2)\times 10^6$	$2.4(\pm 0.1)\times 10^5$
#3	$3.4(\pm 0.3)\times 10^4$	ND	$3.8(\pm 0.2)\times 10^6$	$2.5(\pm 0.1)\times 10^5$
#4	$3.2(\pm 0.3)\times 10^4$	ND	$3.8(\pm 0.2)\times 10^6$	$2.3(\pm 0.1)\times 10^5$
#5	ND	$1.7(\pm 0.2)\times 10^5$	$3.3(\pm 0.2)\times 10^6$	$2.5(\pm 0.1)\times 10^5$
#6	$3.8(\pm 0.4)\times 10^4$	ND	$2.6(\pm 0.1)\times 10^6$	$2.2(\pm 0.1)\times 10^5$

ND: not determined

² Cs-137 is formed by fission of uranium impurities present in Zircaloy cladding.

Table 5.8: Mean values of the experimentally determined inventories of C-14, Fe-55, Cs-137 and Sb-125 in comparison with results from the activation calculations performed in this study and experimentally measured C-14 contents in a spent PWR Zircaloy-4 specimen with a similar burn-up [YAMAGUCHI *et al.*, 1999].

	C-14 [Bq/g Zry-4]	Fe-55 [Bq/g Zry-4]	Cs-137 [Bq/g Zry-4]	Sb-125 [Bq/g Zry-4]
measured contents in Zry-4 of segment SBS1108-N0204 (50.4 GWd/t_{HM}) [p.w.]	3.7(±0.4)×10 ⁴	1.5(±0.1)×10 ⁵	3.4(±0.2)×10 ⁶	2.4(±0.1)×10 ⁵
calculated contents in Zry-4 of segment SBS1108-N0204 (50.4 GWd/t_{HM}) [p.w.]	3.2(±0.3)×10 ⁴	1.3(±0.1)×10 ⁵	2.9(±0.1)×10 ⁴	2.6(±0.1)×10 ⁵
measured contents in Zry-4 of spent PWR fuel rod hull specimen (47.9 GWd/t_{HM}) [Yamaguchi <i>et al.</i>, 1999]	3.2×10 ⁴			

Table 5.9 shows the partitioning between the total inorganic and organic C-14 fractions for each of the six analysed samples. Again, the results obtained for each sample are in good agreement among themselves within the analytical uncertainty, and virtually no differences are seen for the two Zircaloy dissolution approaches used in this study (glass reactor/autoclave). In all experiments, the vast majority of C-14 is found in the organic/CO fraction, whereas almost no inorganic C-14 is found.

Moreover, the autoclave experiments provide additional information about the distribution of the inorganic/organic C-14 compounds released during the acid digestion into the aqueous and gaseous phases. The partitioning of C-14 bearing compounds in inorganic and organic fractions and furthermore the distribution of these fractions in the gaseous and aqueous phase is provided in Table 5.10.

About 88 ± 10% of the C-14 inventory present in irradiated Zircaloy-4 is released as gaseous hydrocarbons/CO during the dissolution into the gas phase. On the contrary, about 11 ± 10% remains as dissolved hydrocarbons in the acidic digestion liquor. Almost no inorganic C-14 bearing compounds (< 1%) are found in all

Results and Discussion

experiments (glass reactor and autoclave) either in the gaseous or in the aqueous phase. Similar to the leaching/digestion experiments performed by Bleier et al. most of the C-14 is found in the gas phase as hydrocarbons/CO [BLEIER *et al.*, 1988]. However, Bleier and co-workers did not analyze the chemical form of C-14 in the aqueous phase of the digestion experiments. In experiments conducted in this study, it is seen that about $11 \pm 10\%$ of the C-14 inventory remains as dissolved hydrocarbons in the aqueous phase. In contrast to results obtained in the present work and [BLEIER *et al.*, 1988], the majority of C-14 leached from irradiated Zircaloy-4 by Yamaguchi et al. was found in the aqueous phase as dissolved hydrocarbons, no C-14 was found in the gas phase [YAMAGUCHI *et al.*, 1999]. However, Yamaguchi et al. neither provide details of the sampling of the gaseous phase for the C-14 extraction and analysis nor details on the oxidation efficiency of the used catalyst for the conversion of CO, CH₄ to CO₂.

Table 5.9: Partitioning of C-14 between total inorganic/organic fractions for each of the six samples.

sample no.	TIC-14	TOC-14
	[Bq/g Zry-4]	[Bq/g Zry-4]
#1	$9.5(\pm 0.1) \times 10^1$	$3.9(\pm 0.4) \times 10^4$
#2	$11.9(\pm 0.1) \times 10^1$	$4.2(\pm 0.4) \times 10^4$
#3	$11.8(\pm 0.1) \times 10^1$	$3.4(\pm 0.3) \times 10^4$
#4	$6.2(\pm 0.1) \times 10^1$	$3.2(\pm 0.3) \times 10^4$
#5	ND	ND
#6	$10.4(\pm 0.1) \times 10^1$	$3.8(\pm 0.4) \times 10^4$

Table 5.10: Distribution of inorganic and organic C-14 bearing compounds in the gaseous and aqueous phase obtained from dissolution experiments performed in an autoclave.

	inorganic C-14		organic C-14	
	mean activity [Bq/g Zry-4]	fraction in %	mean activity [Bq/g Zry-4]	fraction in %
aqueous phase	$1.0(\pm 0.1) \times 10^1$	< 1	$4.0(\pm 0.4) \times 10^3$	11.4 ± 10
gaseous phase	$7.2(\pm 0.7) \times 10^1$	< 1	$3.1(\pm 0.3) \times 10^4$	88.4 ± 10

5.3.6 Conclusions regarding the inventory and chemical form of C-14 in Zircaloy-4

Using the C-14 separation and analysis techniques developed in this work for gaseous and aqueous samples derived from acid digestion of irradiated Zircaloy-4 specimens, it was possible to quantify the C-14 content in these samples. Furthermore, the partitioning of C-14 between inorganic and organic C-14 bearing compounds and their distribution between solution and gas phase was investigated. In addition to C-14, the contents of Fe-55, Sb-125 and Cs-137 in irradiated Zircaloy-4 were analysed and also compared to MCNP-X calculations.

The experimentally determined inventories of C-14, Fe-55 and Sb-125 are in good agreement with the calculated, whereas the Cs-137 inventory exceeds the calculated by a factor of 117 due to the precipitation of Cs-137, released from subjacent UO₂ pellets, on the inner Zircaloy-4 surface, which is not taken into account in the calculations. The vast majority of C-14 is released from irradiated Zircaloy-4 as hydrocarbons/CO into the gas phase (about 88%) and aqueous phase (> 11%). Almost no (< 1%) inorganic C-14 bearing compounds (e.g. carbonates, bicarbonates) were found in all experiments (glass reactor as well as autoclave) conducted with irradiated Zircaloy-4.

The comparison of experimental and theoretically predicted contents of various radionuclides (not only C-14) and their good agreement further proves the reliability of the obtained data. The experimentally determined activities of the activation products in the irradiated Zircaloy-4 agrees within a factor < 2 with the MCNP-X calculation, except for the fission product Cs-137. The difference is considered as relatively small taking into account the limited availability of data for the calculations. Especially, the contents of C-14 precursors in Zircaloy (e.g. N-14,

Results and Discussion

O-17, see section 4.7) and as complete as possible irradiation characteristics are of particular importance for the calculations.

Although the separation technique was tested by dissolving non-irradiated Zircaloy, the interference of ^1H - ^3H (HT), quantitatively released from irradiated Zircaloy-4 during digestion, and its oxidation to HTO was not taken into account and modifications of the separation technique were necessary (see section 5.3.4).

This is the first study assessing the quantity and chemical form of C-14, after release from Zircaloy-4 cladding, in aqueous and gaseous samples derived from respective dissolution experiments. The combination of glass reactor and autoclave experiments allowed to gain not only knowledge about the partitioning of C-14 between inorganic and organic C-14 bearing compounds, but also about the distribution of these compounds in solution and gas phase. Further the release of > 88% of C-14 bearing compounds into the gas phase during acid digestion of irradiated Zircaloy-4 cladding emphasizes the importance of analyzing the C-14 speciation in the gas phase.

Although the digestion experiments were performed under acidic/oxic conditions, clearly outside of repository-relevant conditions, little impact on the chemical form of C-14 released from irradiated Zircaloy under repository relevant conditions is expected. The vast majority of C-14 is found as dissolved/gaseous hydrocarbons and almost no dependency on the pH is expected for the organic compounds. In addition, strongly reducing conditions potentially developing in a deep underground repository for nuclear waste favors the formation of reduced/organic C-14 compounds. The similar outcome of experiments performed in this study under acidic/oxic conditions, room temperature and air/N₂ or air/Ar atmosphere and [BLEIER *et al.*, 1988] using HF, NaCl or NaCl–NaF, 200°C and air atmosphere further support this assumption.

The results obtained in this study can have implication on safety analyses of deep geological repositories for nuclear waste, where C-14 is assumed highly mobile in the aqueous and gaseous phase either as dissolved or gaseous hydrocarbons.

The developed C-14 extraction and analysis methods described in this study for irradiated Zircaloy-4 are not only very reliable but can also be applied in future investigations with other structural parts such as stainless steel or SNF itself of a fuel rod.

6 Summary and Conclusions

This Ph.D. thesis has successfully addressed the aqueous and gaseous speciation of some actinides, lanthanides and the activation product C-14, and further contributed to the understanding of Ln(III) solid phase transformations taking place under repository-relevant conditions. Provided the key role of solubility phenomena and aqueous/gas speciation in the retention/mobilization of radionuclides in deep geological repositories, the scientific results generated in this work represent a significant step forward in the accurate estimation of the source term for several different scenarios as well as in the quantitative description of key geochemical processes.

Nitrate is a relevant but less investigated ligand in the context of nuclear waste disposal. Although the strong hydrolysis of An(III) is expected to outcompete nitrate complexation under near-neutral to hyperalkaline pH conditions, high nitrate concentrations, expected in certain waste forms, may lead to the formation of binary or ternary complexes under repository-relevant pH conditions, eventually leading to the enhancement of An(III) solubility. The effect of nitrate on the solubility and aqueous speciation of An(III)/Ln(III) was studied in dilute to concentrated NaCl–NaNO₃, MgCl₂–Mg(NO₃)₂ and CaCl₂–Ca(NO₃)₂ solutions at $2.91 \leq \text{pH}_m \leq 13.2$ and $T = 22 \pm 2^\circ\text{C}$. Batch solubility experiments with Nd(III) were performed in combination with Cm(III)–TRLFS, Nd–L_{III} EXAFS and extensive solid phase characterization. Nitrate shows a significant influence on the solubility of Nd(OH)₃(s) in concentrated weakly alkaline MgCl₂–Mg(NO₃)₂ solutions, whereas

Summary and Conclusions

no effect is observed in any of the studied NaCl–NaNO₃ and CaCl₂–Ca(NO₃)₂ systems. These results highlight the key role of Mg²⁺ in the Nd(III)–NO₃ interaction, which is further confirmed by Cm(III)–TRLFS and Nd–L_{III} EXAFS. These spectroscopic techniques support the formation of quaternary inner-sphere complexes of the type Mg²⁺–An^{III}/Ln^{III}–NO₃–OH. Based on the newly generated data, the chemical, thermodynamic and activity models for Ln(III) and An(III) are further extended to Ln³⁺/An³⁺–H⁺–Na⁺–Mg²⁺–Ca²⁺–OH[–]–Cl[–]–NO₃[–]–H₂O.

The transformation of Nd(OH)₃(s) into a ternary Nd–OH–Cl(s) solid phase was experimentally assessed in NaCl (5.61 m), MgCl₂ (0.25–5.15 m) and CaCl₂ (3.91 m) systems as a function of pH (7.5 ≤ pH_m ≤ 9.6) and temperature ($T = 22$ and 80°C). Solid phase characterization shows a clear transformation of the initial solid phase into Nd(OH)₂Cl(s) in ≥ 3.87 m MgCl₂ systems at $T = 22$ and 80°C. In a second step of this study, batch solubility experiments were performed using the Nd(OH)₂Cl(s) phase synthesized at $T = 22$ °C in 5.61 m NaCl, 2.11–5.15 m MgCl₂, 2.68/3.91 m CaCl₂ and 7.0 ≤ pH_m ≤ 13. The comparison of Nd(OH)₂Cl(s) and Nd(OH)₃(s) solubility determined under analogous experimental conditions shows significantly lower m_{Nd} (up to 1.5 lg-units) in equilibrium with Nd(OH)₂Cl(s) in 2.11–5.15 m MgCl₂ and 2.68/3.91 m CaCl₂ at pH_m ≤ 9.2. On the contrary, no differences in $m_{\text{Nd(III)}}$ are observed in 5.61 m NaCl within 7.5 ≤ pH_m ≤ 13, indicating that Nd(OH)₂Cl(s) has no (or a very limited) stability field under these conditions. The combination of the experimental solubility data and solid phase characterization gained in this study with the thermodynamic and activity models previously reported in the literature for Nd(III) aqueous species allowed the quantification of $\lg^*K^{\circ}_{s,0}\{\text{Nd(OH)}_2\text{Cl(s)}\}$. The solubility control by this ternary phase in concentrated saline systems represents a previously unknown retention mechanism for An(III) and Ln(III) under repository-relevant pH conditions, and further indicates that the use of An^{III}/Ln^{III}(OH)₃(s) in geochemical calculations and source term estimations is a conservative upper limit.

The activation product C-14 is of high interest in long-term safety assessments of nuclear waste repositories due to its long half-life and high mobility especially assumed for organic/gaseous compounds. Consequently, the chemical form of C-14 is a key parameter for the transport/retention of this radionuclide in the near-field of a repository. Because of the difficulties in separating and quantifying this radionuclide (pure β^- emitter), a robust C-14 extraction and analysis system was developed, applicable to highly radioactive samples. The methodology developed in this Ph.D. thesis allows the simultaneous separation/quantification of C-14 from other radionuclides present in the activated material in aqueous and gaseous aliquots, as well as the determination of the chemical form of the C-14 bearing compounds.

The amount and chemical form of C-14 as well as the inventories of Fe-55, Sb-125 and Cs-137 were determined in Zircaloy-4 cladding from an irradiated UO₂ fuel rod segment. Experimentally measured radionuclide contents were compared to the theoretically predicted inventory of the Zircaloy-4 obtained by means of Monte Carlo N-particle (MCNP-X) calculations. C-14 was separated from other radionuclides in gaseous and aqueous aliquots derived from dissolution experiments performed with the irradiated Zircaloy-4 cladding. Within the analytical uncertainty, the measured C-14, Fe-55 and Sb-125 inventories are in good agreement with the calculations. Moreover, the vast majority of C-14 is found in the gaseous and dissolved organic fractions. Almost no inorganic C-14 bearing compounds were found. The experimental Cs-137 inventory exceeds by a factor of 117 the calculated. The excess of Cs-137 is related to precipitation of Cs-137 on the inner Zircaloy-4 surface of the plenum. This excess of Cs-137 is assumed to be released from subjacent UO₂ pellets during reactor operation and is not taken into account in the calculations, since the MCNP-X simulation does not include the migration of volatile elements.

Appendix

Appendix A

Table A.1: Experimental solubility data of $\text{Nd}(\text{OH})_3(\text{s})$ in NaCl – NaNO_3 mixtures.

Sample $m_{\text{NaCl}} / m_{\text{NaNO}_3}$	23 days		196 days		30 days		398 days	
	pH _m	lg $m_{\text{Nd}^{3+}}$						
$m_{\text{Na}^+} = 0.10$								
0.10/0.00	7.97	-4.80	7.97	-4.90				
	8.95	-8.25	8.95	-8.19				
	9.99	-9.31	9.99	-9.86				
0.00/0.10	7.94	-4.68	7.88	-4.60				
	8.96	-8.42	8.91	-8.08				
	10.00	-8.34	9.87	-9.86				
$m_{\text{Na}^+} = 0.51$								
0.51/0.00	8.00	-4.39	8.00	-4.33				
	8.98	-7.32	8.98	-7.51				
	9.98	-8.55	9.95	-9.15				
0.40/0.10	7.98	-4.34	7.96	-4.28				
	8.95	-7.25	8.95	-7.40				
0.30/0.20	7.99	-4.36	7.97	-4.30				
	8.98	-7.42	8.98	-7.53				
	9.98	-8.61	9.98	-9.16				
0.00/0.51	7.97	-4.35	7.94	-4.31				
	8.95	-7.34	8.94	-7.53				
	9.98	-8.45	9.91	-9.15				
$m_{\text{Na}^+} = 1.02$								
1.02/0.00	8.02	-4.20	7.99	-4.19				
	8.94	-6.98	8.94	-7.17				
	9.98	-8.11	9.96	-8.85				
0.92/0.10	8.00	-4.19	8.05	-4.18				
	8.96	-7.02	9.00	-7.27				
0.82/0.20	7.98	-4.14	8.02	-4.13				
	8.97	-7.08	9.00	-7.24				
0.51/0.51	8.03	-4.17	8.01	-4.23				
	8.98	-7.03	8.97	-7.23				
	10.03	-8.37	10.02	-8.85				

Appendix

0.00/1.03	8.01	-4.18	7.99	-4.20				
	8.93	-6.97	8.94	-7.17				
	9.98	-8.37	9.88	-8.67				
$m_{\text{Na}^+} = 2.64$								
2.64/0.00	7.98	-3.62	7.99	-3.67				
	8.97	-6.42	9.00	-6.68				
	9.92	-7.83	9.92	-8.83				
2.57/0.11	7.95	-3.61	7.97	-3.63				
	9.00	-6.66	9.02	-6.83				
2.47/0.21	7.95	-4.10	7.97	-3.66				
	9.01	-6.79	9.02	-6.82				
2.16/0.54	7.98	-3.72	7.99	-3.65				
	8.99	-6.66	9.00	-6.81				
	9.93	-8.52	10.00	-8.83				
1.63/1.09	7.98	-3.66	7.98	-3.64				
	8.97	-6.64	9.00	-6.77				
	9.96	-8.65	9.98	-8.82				
0.00/2.72	7.95	-3.65	7.93	-3.62				
	8.99	-6.72	8.98	-6.68				
	9.90	-7.48	9.91	-8.82				
$m_{\text{Na}^+} = 5.61$								
5.61/0.00	7.99	-3.37	8.01	-3.34				
	8.95	-5.90	8.95	-5.99				
	9.92	-7.51	9.85	-8.11				
	11.29 ^a	-5.68						
	13.04 ^b	-8.04						
5.61/0.11	7.99	-3.37	8.00	-3.32				
	8.94	-5.89	8.91	-5.96				
5.50/0.23	8.01	-3.33	8.01	-3.29				
	8.95	-5.84	8.92	-6.00				
	10.02	-7.62	9.88	-8.10				
	11.11 ^a	-8.68						
	13.00 ^b	-7.71						
5.17/0.57	7.99	-3.39	8.01	-3.34				
	8.92	-5.78	8.89	-5.85				
	11.12 ^a	-8.68						
	12.97 ^b	-8.04						
4.61/1.15	8.00	-3.33	8.03	-3.31				
	8.94	-5.88	8.93	-5.95				
	9.95	-8.00	9.88	-8.40				
	11.11 ^a	-7.21						
	12.85 ^b	-8.04						
3.48/2.32	11.07 ^a	-8.68						
	12.94 ^b	-8.68						
2.90/2.90	7.97	-3.31	8.01	-3.27	13.20 ^c	-7.68	13.24 ^c	-7.75
	8.95	-5.88	8.91	-5.95				
1.75/4.08	7.98	-3.26	7.99	-3.20	13.15 ^c	-8.86	13.24 ^c	-7.69
	8.94	-5.79	8.89	-5.86				
	9.92	-8.00	9.81	-8.39				
0.00/6.02	7.96	-3.33	7.97	-3.27	10.34 ^a	-7.47	10.44 ^a	-6.78
	8.89	-5.92	8.83	-5.96	12.81 ^b	-8.78	12.91 ^b	-7.00
	9.90	-7.57	9.77	-7.84	13.11 ^c	-8.38	13.18 ^c	-7.70

^a buffered with brucite. ^b buffered with portlandite. ^c pH adjusted with NaOH.

Table A.2: Experimental solubility data of Nd(OH)₃(s) in MgCl₂–Mg(NO₃)₂ mixtures.

Sample <i>m</i> _{MgCl₂} / <i>m</i> _{Mg(NO₃)₂}	14 days		36 days		74 days		238 days	
	pH _m	lg <i>m</i> _{Nd³⁺}						
<i>m</i> _{Mg²⁺} = 0.25								
0.25/0.00	9.22 ^a	-7.59	9.09 ^a	-7.73				
	8.32	-5.10	8.20	-5.23				
	7.65	-3.37	7.58	-3.46				
0.20/0.05	9.20 ^a	-7.68	9.07 ^a	-7.76				
	8.30	-5.04	8.21	-5.17				
	7.65	-3.39	7.58	-3.52				
0.15/0.10	9.20 ^a	-7.61	9.03 ^a	-7.67				
	8.30	-5.00	8.19	-5.20				
	7.65	-3.38	7.58	-3.51				
<i>m</i> _{Mg²⁺} = 1.04								
1.04/0.00	9.06 ^a	-6.56	8.95 ^a	-6.64	9.07 ^a	-6.72	9.03 ^a	-6.65
	8.47	-4.87	8.38	-4.96				
	7.91	-4.34	7.81	-3.48				
0.99/0.05	9.06 ^a	-5.53	8.91 ^a	-6.60	9.03 ^a	-6.72	9.05 ^a	-6.33
	8.46	-5.20	8.34	-4.95				
	7.89	-3.59	7.79	-3.67				
0.94/0.10	9.04 ^a	-6.52	8.92 ^a	-6.59	9.05 ^a	-6.69	9.01 ^a	-6.42
	8.44	-4.86	8.40	-4.92				
	7.90	-3.47	7.89	-3.58				
0.79/0.26	9.02 ^a	-6.39	8.90 ^a	-6.49	9.05 ^a	-6.54	8.96 ^a	-6.47
	8.42	-4.77	8.38	-4.87				
	7.89	-4.59	7.88	-3.43				
0.53/0.53	8.94 ^a	-6.28	8.86 ^a	-6.41	9.01 ^a	-6.55	8.95 ^a	-6.44
	8.38	-4.67	8.34	-4.82				
	7.88	-3.54	7.91	-3.64				
0.00/1.07	8.89 ^a	-5.30	8.80 ^a	-6.18	8.91 ^a	-6.33	8.87 ^a	-6.16
	8.40	-4.60	8.32	-4.75				
	7.95	-3.55	7.88	-3.69				
<i>m</i> _{Mg²⁺} = 2.80								
2.80/0.00	8.89 ^a	-4.88	8.87 ^a	-5.00			8.82 ^a	-5.06
	8.46	-3.99	8.46	-4.07			8.90 ^a	-5.53
	8.06	-3.33	8.13	-3.38				
	9.07 ^a	-5.50						
2.75/0.06	8.91 ^a	-4.91	8.88 ^a	-4.98			8.85 ^a	-5.07
	8.52	-4.04	8.49	-4.20			8.93 ^a	-5.54
	8.02	-3.36	8.10	-3.41				
	9.10 ^a	-5.46						
2.70/0.11	8.90 ^a	-4.86	8.87 ^a	-4.92			8.88 ^a	-5.00
	8.52	-3.97	8.51	-4.14			8.93 ^a	-5.42
	8.07	-3.29	8.12	-3.31				
	9.09 ^a	-5.38						
2.54/0.28	8.89 ^a	-4.76	8.85 ^a	-4.87	8.93 ^a	-5.01	8.87 ^a	-4.93
	8.48	-3.97	8.47	-4.07			8.91 ^a	-5.10
	8.06	-3.25	8.10	-3.35				
	9.06 ^a	-5.17						
2.27/0.57	8.84 ^a	-4.56	8.78 ^a	-4.67	8.90 ^a	-4.81	8.84 ^a	-4.77
	8.48	-3.89	8.45	-4.00			8.89 ^a	-5.19
	8.02	-3.27	8.10	-3.30				

Appendix

	9.01 ^a	-5.13							
1.72/1.14	8.81 ^a	-4.37	8.77 ^a	-4.44	8.84 ^a	-4.58	8.75 ^a	-4.48	
	8.49	-3.88	8.46	-3.99			8.85 ^a	-4.65	
	8.02	-3.12	8.09	-3.18					
	8.94 ^a	-4.84							
0.00/2.91	8.60 ^a	-3.92	8.52 ^a	-4.05	8.63 ^a	-4.14	8.56 ^a	-4.11	
	8.39	-3.71	8.35	-3.83			8.67 ^a	-4.39	
	8.03	-3.21	8.06	-3.33					
	8.69 ^a	-4.58							
$m_{\text{Mg}^{2+}} = 4.05$									
4.05/0.00	8.81 ^a	-4.28	8.86 ^a	-4.46	8.84 ^a	-4.66	8.81 ^a	-4.60	
	8.32	-3.63	8.47	-3.88	8.47	-4.17	8.52	-4.41	
	8.15	-3.16	8.20	-3.38	8.13	-3.65	7.96	-4.07	
	8.93 ^a	-4.49					8.80 ^a	-4.41	
	8.88 ^a	-4.43							
4.00/0.06	8.80 ^a	-4.21	8.83 ^a	-4.39	8.84 ^a	-4.58	8.78 ^a	-4.53	
	8.30	-3.55	8.45	-3.78	8.49	-4.07	8.51	-4.39	
	8.10	-3.04	8.15	-3.22	8.17	-3.42	7.79	-3.71	
	8.98 ^a	-4.66					8.82 ^a	-4.58	
	8.86 ^a	-4.62							
3.94/0.12	8.80 ^a	-4.14	8.84 ^a	-4.30	8.87 ^a	-4.53	8.78 ^a	-4.49	
	8.41	-3.57	8.46	-3.81	8.50	-4.17	8.51	-4.28	
	8.18	-3.14	8.22	-3.27	8.21	-3.27	7.92	-3.57	
	8.87 ^a	-4.34					8.82 ^a	-4.45	
	8.87 ^a	-4.54							
3.77/0.29	8.78 ^a	-3.97	8.79 ^a	-4.13	8.83 ^a	-4.08	8.75 ^a	-4.12	
	8.38	-3.37	8.44	-3.55	8.45	-3.56	8.42	-3.83	
	8.23	-3.10	8.30	-3.22	8.30	-3.16	8.19	-3.20	
	8.87 ^a	-4.17					8.78 ^a	-4.13	
	8.77 ^a	-4.13							
3.49/0.58	8.74 ^a	-3.81	8.76 ^a	-3.96	8.74 ^a	-3.89	8.71 ^a	-3.85	
	8.40	-3.32	8.42	-3.45	8.44	-3.33	8.39	-3.30	
	8.20	-3.11	8.29	-3.25	8.31	-3.15	8.28	-3.08	
	8.88 ^a	-3.95					8.73 ^a	-4.02	
	8.76 ^a	-4.06							
2.91/1.16	8.68 ^a	-3.54	8.70 ^a	-3.67	8.70 ^a	-3.57	8.64 ^a	-3.57	
	8.41	-3.22	8.46	-3.34	8.48	-3.24	8.41	-3.20	
	8.24	-2.94	8.30	-3.10	8.31	-2.97	8.27	-2.95	
	8.96 ^a	-3.69					8.68 ^a	-3.77	
	8.94 ^a	-3.84							
1.16/2.90	8.53 ^a	-3.29	8.52 ^a	-3.40	8.50 ^a	-3.26	8.49 ^a	-3.20	
	8.35	-3.16	8.38	-3.25	8.35	-3.13	8.37	-3.06	
	8.18	-2.80	8.24	-2.95	8.21	-2.84	8.24	-2.81	
	8.88 ^a	-3.95	8.04	-2.42			7.76	-1.87	
	8.72 ^a	-3.55	8.67 ^a	-3.39			7.99	-2.04	
							8.13	-2.33	
							8.56 ^a	-3.25	
							8.60 ^a	-3.32	
0.00/4.02	8.41 ^a	-3.14	8.36 ^a	-3.22	8.42 ^a	-3.10	8.37 ^a	-3.03	
	8.33	-3.13	8.30	-3.23	8.28	-3.10	8.33	-2.99	
	8.08	-2.82	8.11	-2.95	8.11	-2.80	8.18	-2.78	
	8.71 ^a	-3.86					8.45 ^a	-3.33	
	8.62 ^a	-3.63							

$m_{\text{Mg}^{2+}} = 5.24$						
5.24/0.00	8.85 ^a	-4.23	8.84 ^a	-4.53	8.78 ^a	-4.77
	8.39	-3.99	8.39	-4.34	8.35	-4.71
	7.91	-3.51	7.82	-3.65	7.68	-3.67
5.19/0.06	8.87 ^a	-4.12	8.84 ^a	-4.40		
	8.39	-3.85	8.40	-4.19		
	7.99	-3.43	7.93	-3.63		
5.13/0.12	8.86 ^a	-4.07	8.79 ^a	-4.30		
	8.33	-3.71	8.40	-4.07		
			7.67	-3.01		
4.95/0.29	8.80 ^a	-3.99	8.76 ^a	-4.06	8.72 ^a	-3.80
	8.48	-3.38	8.48	-3.51	8.40	-4.11
			7.81	-2.96	7.47	-2.90
4.65/0.58	8.71 ^a	-3.49	8.69 ^a	-3.58	7.55	-2.76
	8.43	-3.22	8.45	-3.32	8.41	-3.60
			7.93	-2.74	8.65 ^a	-3.58
4.05/1.16	8.57 ^a	-3.32	8.56 ^a	-3.42	8.51 ^a	-3.20
	8.39	-3.06	8.56	-2.98	8.52	-3.56
			8.11	-2.27	7.43	-2.24

^a buffered with brucite/Mg-oxychloride.

Table A.3: Experimental solubility data of $\text{Nd}(\text{OH})_3(\text{s})$ in $\text{CaCl}_2\text{--Ca}(\text{NO}_3)_2$ mixtures.

Sample $m_{\text{CaCl}_2} / m_{\text{Ca}(\text{NO}_3)_2}$	14 days		30 days		398 days	
	pH_m	$\lg m_{\text{Nd}^{3+}}$	pH_m	$\lg m_{\text{Nd}^{3+}}$	pH_m	$\lg m_{\text{Nd}^{3+}}$
$m_{\text{Ca}^{2+}} = 2.85$						
2.85/0.00	11.94 ^b	-7.30				
2.74/0.11	11.97 ^b	-7.13				
2.57/0.29	11.99 ^b	-6.77				
2.30/0.57	12.04 ^b	-7.20				
1.73/1.16	12.09 ^b	-7.19				
$m_{\text{Ca}^{2+}} = 4.02$						
1.15/2.87			7.94	-2.81	7.97	-2.74
			8.30	-3.77	8.34	-3.68
			8.68	-4.71	8.59	-4.74
			9.05	-5.78	8.98	-5.78
			9.34	-6.54	9.33	-6.56
			9.76	-7.48	9.78	-7.20
			10.36 ^a	-8.25	10.42 ^a	-8.10
			12.08 ^b	-6.28	12.20 ^b	-6.23

^a buffered with brucite. ^b buffered with portlandite.

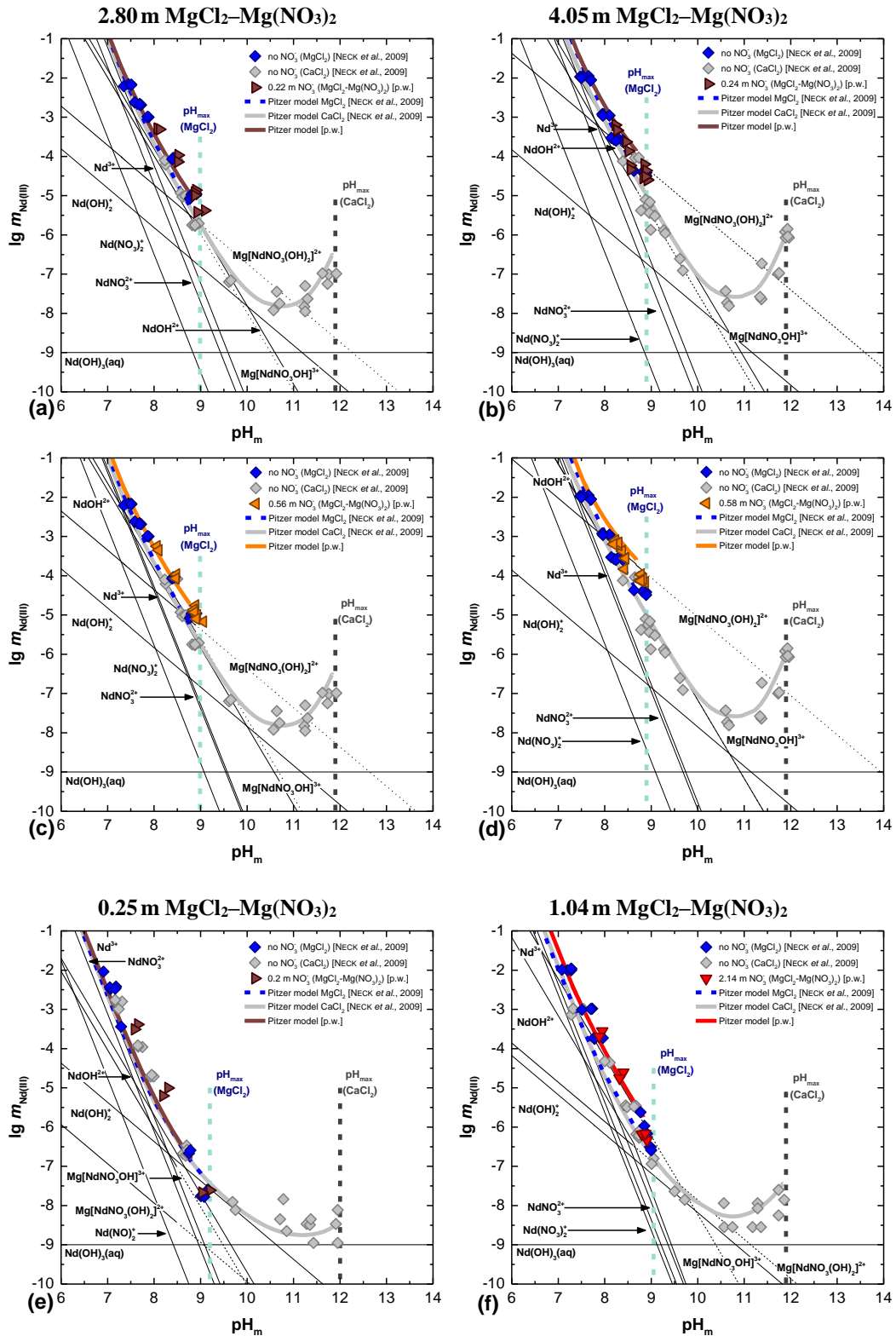


Figure A.1: Solubility of $\text{Nd(OH)}_3(\text{s})$ in 2.80 m $\text{MgCl}_2\text{-Mg(NO}_3)_2$ with (a) 0.22 m and (c) 0.56 m NO_3^- in comparison with 4.05 m $\text{MgCl}_2\text{-Mg(NO}_3)_2$ with (b) 0.24 m and (d) 0.58 m NO_3^- . Together with solubility of $\text{Nd(OH)}_3(\text{s})$ in (e) 0.25 m $\text{MgCl}_2\text{-Mg(NO}_3)_2$ with 0.2 m NO_3^- and (f) 1.04 m $\text{MgCl}_2\text{-Mg(NO}_3)_2$ with 2.14 m NO_3^- . Reference data in nitrate-free solutions [NECK *et al.*, 2009] is included in all the figures for comparison. Thick solid lines correspond to the Nd(III) solubility calculated using thermodynamic and activity models: for pure MgCl_2 and CaCl_2 systems (blue and grey lines) [NECK *et al.*, 2009]; for $\text{MgCl}_2\text{-Mg(NO}_3)_2$ mixtures (brown, orange, red lines) [p.w.]. Thin lines show the aqueous speciation underlying $\text{Nd(OH)}_3(\text{s})$ solubility curve in $\text{MgCl}_2\text{-Mg(NO}_3)_2$ systems.

Appendix B

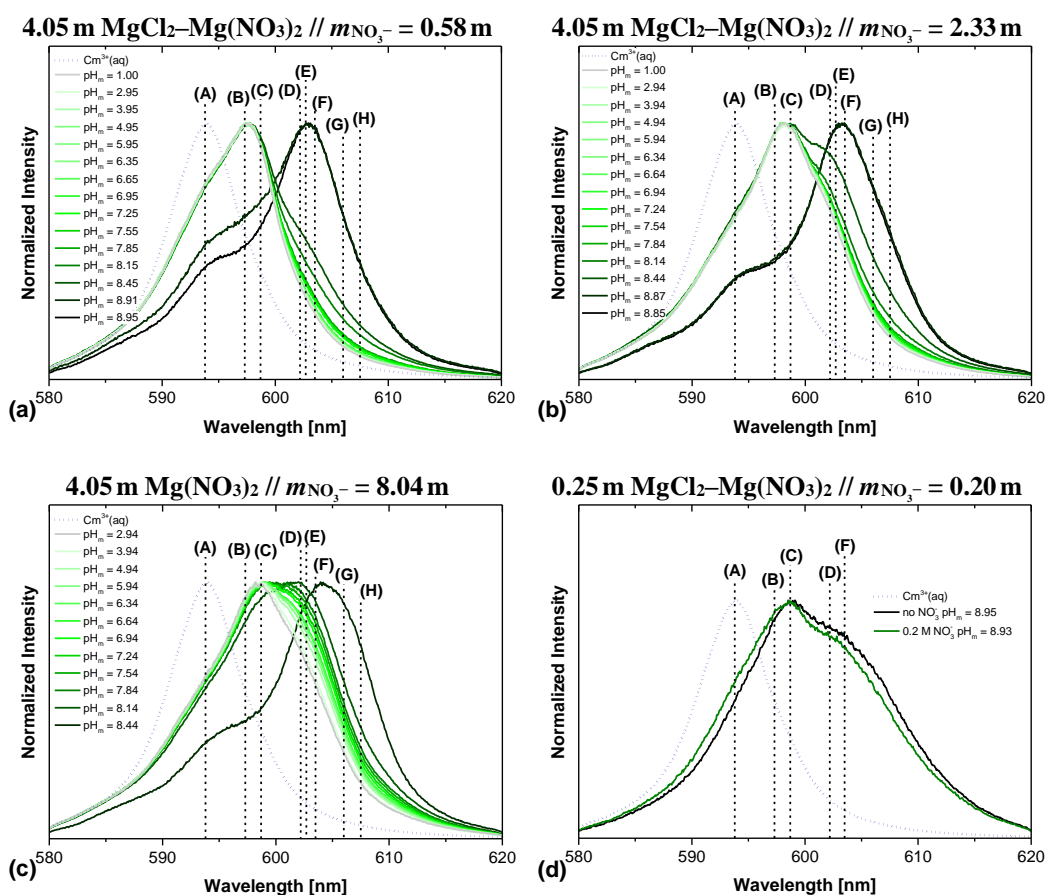


Figure B.1: Cm(III)-TRLFS spectra over the entire investigated pH range obtained in (a) 4.05 m MgCl₂-Mg(NO₃)₂ mixture with m_{NO₃⁻} = 0.58 m, (b) 4.05 m MgCl₂-Mg(NO₃)₂ mixture with m_{NO₃⁻} = 2.33 m, (c) 4.05 m Mg(NO₃)₂ with m_{NO₃⁻} = 8.04 m and (d) 0.25 m MgCl₂-Mg(NO₃)₂ mixture with m_{NO₃⁻} = 0.20 m. Capital letters in figures (a) to (d) refer to: A = Cm³⁺ aquo ion, B = CmNO₃²⁺, C = CmOH²⁺, D = Cm(NO₃)₂⁺, E = Mg[CmNO₃OH]³⁺, F = Cm(OH)₂⁺, G = Mg[CmNO₃(OH)₂]²⁺, H = Cm(OH)₃(aq), I = CmCl²⁺ and J = CmCl₂⁺.

Appendix C

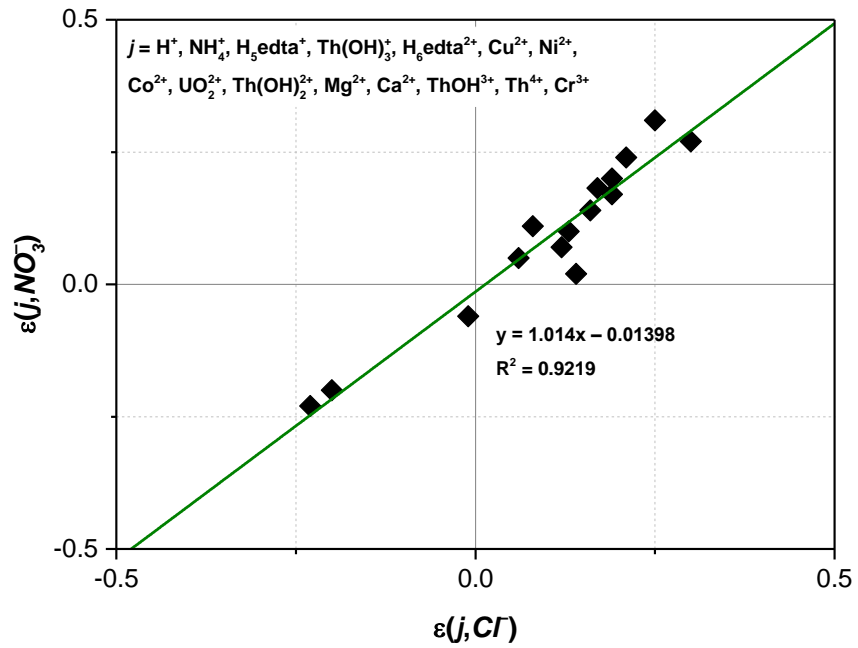


Figure C.1: Correlation of SIT ion interaction parameters reported for +1 to +4 monomeric cations [RAND *et al.*, 2008] with chloride and nitrate.

Appendix D

Table D.1: Experimental solubility data of Nd(OH)₂Cl(s) in NaCl solutions.

[NaCl]	39 days		97 days		112 days		321 days	
	pH _m	lgm _{Nd³⁺}						
5.61 m	7.5	-3.21	7.49	-2.80	7.55	-3.20	7.65	-3.19
	7.95	-4.02			7.97	-4.03	8.12	-3.97
	8.85	-5.98			8.82	-6.20	8.95	-5.64
	9.75	-8.15			9.76	-8.26	9.89	-7.59
	12.96	-8.11			12.95	-8.41	12.95	-7.08

Table D.2: Experimental solubility data of Nd(OH)₂Cl(s) in MgCl₂ solutions.

[MgCl ₂]	39 days		97 days		112 days		321 days	
	pH _m	lgm _{Nd³⁺}						
2.11 m			7.46	-2.81				
			7.63	-3.21				
			7.99	-3.84				
			8.59	-4.57				
2.67 m	7.58	-3.27	7.42	-3.03	7.53	-3.24	7.64	-3.29
	7.99	-4.02			7.99	-4.04	8.11	-4.07
	8.39	-4.76			8.40	-4.81	8.50	-4.77
	8.86	-5.57			8.86	-5.58	8.97	-5.55
3.87 m	7.52	-3.41	7.34	-3.00	7.52	-3.47	7.56	-3.43
	7.88	-4.20			7.98	-4.27	8.06	-4.24
	8.49	-5.15			8.54	-5.22	8.65	-5.18
	8.74	-5.47			8.78	-5.55	8.88	-5.51
5.15 m	7.54	-3.54	7.06	-2.75	7.58	-3.63	7.57	-3.64
	7.91	-4.28			7.97	-4.36	8.05	-4.36
	8.56	-5.32			8.58	-5.40	8.66	-5.36
	8.76	-5.59			8.78	-5.67	8.86	-5.60

Appendix

Table D.3: Experimental solubility data of $\text{Nd}(\text{OH})_2\text{Cl}(\text{s})$ in CaCl_2 solutions.

[CaCl ₂]	39 days		97 days		112 days		321 days	
	pH _m	lgm _{Nd³⁺}						
2.68 m			7.42	-2.99				
			7.48	-3.15				
			8.00	-4.14				
			8.44	-5.02				
3.91 m	7.58	-3.47	7.23	-2.92	7.58	-3.49	7.56	-3.48
	8.53	-5.19			8.52	-5.21	8.53	-5.19
	9.52	-7.13			9.51	-7.14	9.52	-7.01
	10.67	-8.21			10.64	-7.25	10.64	-7.40
	12.08	-5.28			12.01	-5.29	12.02	-5.10

Table D.4: Experimental solubility data of “mixing” experiments performed with $\text{Nd}(\text{OH})_3(\text{s})$ and $\text{Nd}(\text{OH})_2\text{Cl}(\text{s})$ in various background electrolytes.

	220 days	
	pH _m	lgm _{Nd³⁺}
5.61 m NaCl	9.34	-7.07
2.11 m MgCl₂	8.59	-4.68
2.67 m MgCl₂	8.57	-4.52
3.87 m MgCl₂	8.79	-4.68
5.15 m MgCl₂	8.78	-4.93
2.68 m CaCl₂	9.32	-6.27
3.91 m CaCl₂	9.61	-6.68

References

ALMOND, P. M., SKANTHAKUMAR, S., SODERHOLM, L., AND BURNS, P. C. 2007. Cation-cation interactions and antiferromagnetism in $\text{Na}[\text{Np}(\text{V})\text{O}_2(\text{OH})_2]$: synthesis, structure, and magnetic properties. *Chem. Mater.*, Vol. 19, 280-285.

ALTMAIER, M., NECK, V., METZ, V., MÜLLER, R., SCHLIEKER, M., AND FANGHÄNEL, T. 2003a. Solubility of U(VI) in NaCl and MgCl_2 solution. *Proceedings of the 9th International Conference on the Chemistry and Migration Behaviour of Actinides and Fission Products in the Geosphere, MIGRATION '03*. Gyeongju, Korea.

ALTMAIER, M., METZ, V., NECK, V., MÜLLER, R., AND FANGHÄNEL, T. 2003b. Solid-liquid equilibria of $\text{Mg}(\text{OH})_2(\text{cr})$ and $\text{Mg}_2(\text{OH})_3\text{Cl} \cdot 4\text{H}_2\text{O}(\text{cr})$ in the system Mg-Na-H-OH-Cl- H_2O at 25°C. *Geochim. Cosmochim. Acta*, Vol. 67, 3595-3601.

ALTMAIER, M., NECK, V., AND FANGHÄNEL, T. 2008. Solubility of Zr(IV), Th(IV) and Pu(IV) hydrous oxides in CaCl_2 solutions and the formation of ternary Ca-M(IV)-OH complexes. *Radiochim. Acta*, Vol. 96, 541-550.

ALTMAIER, M., GAONA, X., AND FANGHÄNEL, T. 2013. Recent Advances in Aqueous Actinide Chemistry and Thermodynamics. *Chem. Rev.*, Vol. 113, 901-943.

BAILLY, H., MÉNESSIER, D., AND PRUNIER, C. 1999. *The nuclear fuel of pressurized water reactors and fast reactors: design and behaviour* (Paris: Lavoisier Publishing).

BATES, R. G. 1948. Definition of pH scales. *Chem. Rev.*, Vol. 42, 1-61.

BEALL, G. W., MILLIGAN, W. O., DILLIN, D. R., WILLIAMS, R. J., AND MCCOY, J. J. 1976. Refinement of neodymium trihydroxide. *Acta Crystallogr. Sec. B.*, Vol. 32, 2227-2229.

References

- BEITZ, J. V., WESTER, D. W., AND WILLIAMS, C. W. 1983. 5f state interaction with inner coordination sphere ligands - Es^{3+} -ion fluorescence in aqueous and organic phases. *J. Less. Common. Met.*, Vol. 93, 331-338.
- BEITZ, J. V., JURSIK, G., AND SULLIVAN, J. C. 1989. Fluorescence studies of Am^{3+} in Aqueous Solution. *Proceedings of the Rare Earth. Lausanne.*
- BERNHARD, G., GEIPEL, G., BRENDLER, V., AND NITSCHKE, H. 1996. Speciation of uranium in seepage waters from a mine tailing pile studied by time-resolved laser-induced fluorescence spectroscopy (TRLFS). *Radiochim. Acta*, Vol. 74, 87-91.
- BERNHARD, G., GEIPEL, G., REICH, T., BRENDLER, V., AMAYRI, S., AND NITSCHKE, H. 2001. Uranyl(VI) carbonate complex formation: validation of the $\text{Ca}_2\text{UO}_2(\text{CO})_3(\text{aq})$ species. *Radiochim. Acta*, Vol. 89, 511-518.
- BGBL 2005. Verordnung über den Schutz vor Schäden durch ionisierende Strahlen (Strahlenschutzverordnung - StrlSchV). Teil I Nr. 49.
- BLEIER, A., BEUERLE, M., AND NEEB, K. H. 1984. Untersuchung zum Inventar und der Verteilung von ^3H und ^{14}C in abgebrannten SWR-Brennstäben. *Kraftwerk Union, KWU*, R 917/84/018.
- BLEIER, A., KROEBEL, R., NEEB, K. H., AND WIESE, H. W. 1987. Kohlenstoff-14 in LWR-Brennstäben und dessen Verhalten beim Wiederaufarbeitungsprozess. *Proceedings of the Jahrestagung Kerntechnik '87. Karlsruhe.*
- BLEIER, A., BEUERLE, M., ELLINGER, M., AND BOHLEN, D. 1988. Untersuchungen zum chemischen Status von C14 nach Auslaugung mit einer Salzlösung aus Hüllmaterial bestrahlter DWR- und SWR-Brennelemente. *Siemens, KWU*, U9 414/88/001.
- BREWITZ, W. 1980. F+E Programm zur Eignungsprüfung der Schachtanlage Konrad für die Einlagerung radioaktiver Abfälle – Zusammenfassender Zwischenbericht. GSF-T 114.
- BUBE, C., METZ, V., BOHNERT, E., GARBEV, K., SCHILD, D., AND KIENZLER, B. 2013. Long-term cement corrosion in chloride-rich solutions relevant to radioactive waste disposal in rock salt - Leaching experiments and thermodynamic simulations. *Phys. Chem. Earth*, Vol. 64, 87-94.
- BUCK, R., RONDININI, S., COVINGTON, A., BAUCKE, F., BRETT, C., CAMOES, M., MILTON, M., MUSSINI, T., NAUMANN, R., AND PRATT, K. 2002. Measurements of pH. Definition, standards, and procedures (IUPAC Recommendations 2002). *Pure Appl. Chem.*, Vol. 74, 2169-2200.

- BUKIN, V. I. 1972. Neutron diffraction and X-ray diffraction study of the crystalline structure of neodymium hydroxyl-chloride, $\text{Nd}(\text{OH})_2\text{Cl}$. *Dokl. Akad. Nauk SSSR*, Vol. 207, 1332-1335.
- BUTLER, J. AND COGLEY, D. 1998. *Ionic Equilibrium: Solubility and pH Calculations* (New York: John Wiley and Sons).
- CARNALL, W. T. 1976. *The absorption and fluorescence spectra of rare earth ions in solution in Handbook on the physics and chemistry of rare earth* (Amsterdam: North Holland Publishing).
- CARNALL, W. T., BEITZ, J. V., AND CROSSWHITE, H. 1984. Electronic-energy level and intensity correlations in the spectra of the trivalent actinide aquo ions. III. Bk^{3+} . *J. Chem. Phys.*, Vol. 80, 2301-2308.
- CHAIX-PLUCHERY, O., PANNETIER, J., BOUILLOT, J., AND NIEPCE, J. C. 1987. Structural pre-reactional transformation in $\text{Ca}(\text{OH})_2$. *J. Solid State Chem.*, Vol. 67, 225-234.
- CHOPPIN, G. R. 1983. Solution Chemistry of the Actinides. *Radiochim. Acta*, Vol. 32, 43-53.
- CHOPPIN, G. R. AND RIZKALLA, E. N. 1994. Solution Chemistry of Actinides and Lanthanides. In *Handbook on the Physics and Chemistry of Rare Earth* (Gschneidner Jr. KA and Eyring L, Eds.). North Holland. Amsterdam.
- CIAVATTA, L. 1980. The Specific Interaction Theory in Evaluating Ionic Equilibria. *Ann. Chim.*, Vol. 70, 551-567.
- CLEGG, S. L. AND WHITFIELD, M. 1991. Activity coefficients in natural water. In *Activity coefficients in electrolyte solutions* (Pitzer KS, Ed.). CRC Press. Boca Raton.
- COTTON, S. 2006. *Lanthanide and Actinide Chemistry* (West Sussex: John Wiley & Sons Ltd.).
- CRAWFORD, B. A., LOTT, S. A., SPARKS, L. D., VAN SOEST, G., AND MCINROY, B. 2006. The Road to Recertification: WIPP TRU Waste Inventory. *Proceedings of the Waste Management 2006 Conference, WM'06 Conference. Tucson, Arizona.*
- DE WOLFF, P. M. 1957. *Technisch Physische Dienst, Delft, Netherlands.*
- DECAMBOX, P., KIRSCH, B., MAUCHIEN, P., AND MOULIN, C. 1989. New

References

spectrofluorometer with pulsed intensified photodiodes array for direct trace determination of actinides and lanthanides in solutions. *Proceedings of the Pittsburgh Conference. Atlanta.*

DIAKONOV, I. I., RAGNARSDOTTIR, K. V., AND TAGIROV, B. R. 1998a. Standard thermodynamic properties and heat capacity equations of rare earth hydroxides: II. Ce(III)-, Pr-, Sm-, Eu(III)-, Gd-, Tb-, Dy-, Ho-, Er-, Tm-, Yb-, and Y-hydroxides. Comparison of thermochemical and solubility data. *Chem. Geol.*, Vol. 151, 327-347.

DIAKONOV, I. I., TAGIROV, B. R., AND RAGNARSDOTTIR, K. V. 1998b. Standard Thermodynamic Properties and Heat Capacity Equations for Rare Earth Element Hydroxides: I. La(OH)₃(s) and Nd(OH)₃(s). Comparison of Thermochemical and Solubility Data. *Radiochim. Acta*, Vol. 81, 107-116.

DURRANT, P. J. AND DURRANT, B. 1970. *Introduction to Advanced Inorganic Chemistry* (London: Longman Grp. Ltd.).

ENDF/B-VII 2011. Special Issue on ENDF/B-VII.1 Library. *Nucl. Data Sheets*, Vol. 112, 2887-3152.

ENDRIZZI, F. AND RAO, L. 2014. Chemical speciation of uranium(VI) in marine environments: complexation of calcium and magnesium ions with [(UO₂)(CO₃)₃]⁴⁻ and the effect on the extraction of uranium from seawater. *Chem. Eur. J.*, Vol. 20, 14499-14506.

FANGHÄNEL, T., KIM, J. I., PAVIET, P., KLENZE, R., AND HAUSER, W. 1994. Thermodynamics of Radioactive Trace Elements in Concentrated Electrolyte Solutions: Hydrolysis of Cm³⁺ in NaCl-Solutions. *Radiochim. Acta*, Vol. 66/67, 81-87.

FANGHÄNEL, T., KIM, J. I., KLENZE, R., AND KATO, Y. 1995. Formation of Cm(III) chloride complexes in CaCl₂ solutions. *J. Alloy Compd.*, Vol. 225, 308-311.

FANGHÄNEL, T. AND KIM, J. I. 1998. Spectroscopic evaluation of thermodynamics of trivalent actinides in brines. *J. Alloy Compd.*, Vol. 271-273, 728-737.

FELLHAUER, D., NECK, V., ALTMAIER, M., LÜTZENKIRCHEN, J., AND FANGHÄNEL, T. 2010. Solubility of tetravalent actinides in alkaline CaCl₂ solutions and formation of Ca₄[An(OH)₈]⁴⁺ complexes. A study of Np(IV) and Pu(IV) under reducing conditions and the systematic trend in the An(IV) series. *Radiochim. Acta*, Vol. 98, 541-548.

FELLHAUER, D. 2013. Untersuchung zur Redoxchemie und Löslichkeit von

Neptunium und Plutonium. Ruprecht-Karls-Universität Heidelberg.

FELMY, A. R., RAI, D., SCHRAMKE, J. A., AND RYAN, J. L. 1989. The solubility of plutonium hydroxide in dilute solution and in high-ionic-strength chloride brines. *Radiochim. Acta*, Vol. 48, 29-36.

FRAPE, S. K. AND FRITZ, P. 1984. Water-rock interaction and chemistry of groundwaters from the Canadian Shield. *Geochim. Cosmochim. Acta*, Vol. 48, 1617-1627.

FUGER, J., NITSCHKE, H., POTTER, P., RAND, M. H., RYDBERG, J., SPAHIU, K., SULLIVAN, J. C., ULLMAN, W. J., VITORGE, P., AND WANNER, H. 2001. *Chemical Thermodynamics Vol. 4. Chemical Thermodynamics of Neptunium and Plutonium* (Amsterdam: Elsevier).

GAONA, X., FELLHAUER, D., AND ALTMAIER, M. 2013. Thermodynamic description of Np(VI) solubility, hydrolysis, and redox behavior in dilute to concentrated alkaline NaCl solutions. *Pure Appl. Chem.*, Vol. 85, 2027-2049.

GIFFAUT, E., GRIVÉ, M., BLANC, P., VIEILLARD, P., COLÀS, E., GAILHANOU, H., GABOREAU, S., MARTY, N., MADÉ, B., AND DURO, L. 2014. Andra thermodynamic database for performance assessment: ThermoChimie. *Appl. Geochem.*, Vol. 49, 225-236.

GONZALEZ-ROBLES, E., BOHNERT, E., LOIDA, A., MÜLLER, N., LAGOS, M., METZ, V., AND KIENZLER, B. 2012. Fission gas measurements and description of leaching experiments with of KIT's irradiated PWR fuel rod segment (50.4 GWd/t_{HM}). *Proceedings of the 1st Annual Workshop Proceedings of the Collaborative Project Fast/Instant Release of Safety Relevant Radionuclides from Spent Nuclear Fuel. Budapest, Hungary.* KIT Scientific Publishing, KIT SR 7639.

GÖTZMANN, O., HOFMANN, P., AND THÜMMLER, F. 1974. Attack upon the cladding of oxide fuel pins by fuel and fission products. *J. Nucl. Mater.*, Vol. 52, 33-50.

GÖTZMANN, O. 1979. A thermodynamic model for the attack behaviour in stainless steel clad oxide fuel pins. *J. Nucl. Mater.*, Vol. 84, 39-54.

GÖTZMANN, O. 1982. Thermochemical evaluation of PCI failures in LWR fuel pins. *J. Nucl. Mater.*, Vol. 107, 185-195.

GRAHEK, Z. AND ROZMARIC MACEFAT, M. 2006. Extraction chromatographic separation of iron from complex liquid samples and the determination of ⁵⁵Fe. *J. Radioanal. Nucl. Chem.*, Vol. 267, 131-137.

References

GRAS, J.-M. 2014. State of the art of ^{14}C in Zircaloy and Zr alloys - ^{14}C release from zirconium alloy hulls (D3.1). *Carbon-14 Source Term WP3 Deliverable D3.1*, CAST-D3.1.

GRENTHE, I., FUGER, J., KONINGS, R. J. M., LEMIRE, R. J., MULLER, A. B., NGUYEN-TRUNG, C., AND WANNER, H. 1992. *Chemical Thermodynamics Vol. 1. Chemical Thermodynamics of Uranium* (Amsterdam: Elsevier).

GRENTHE, I. AND PLYASUNOV, A. 1997. On the use of semiempirical electrolyte theories for the modeling of solution chemical data. *Pure Appl. Chem.*, Vol. 69, 951-958.

GRENTHE, I., MOMPEAN, F., SPAHIU, K., AND WANNER, H. 2013. *Guidelines for the Extrapolation to Zero Ionic Strength* (Issy-les-Moulineaux: OECD-NEA).

GUILLAUMONT, R., FANGHÄNEL, T., NECK, V., FUGER, J., PALMER, D. A., GRENTHE, I., AND RAND, M. H. 2003. *Chemical Thermodynamics Vol. 5. Update on the Chemical Thermodynamics of Uranium, Neptunium, Plutonium, Americium and Technetium* (Amsterdam: Elsevier).

HARVIE, C. E., MOLLER, N., AND WEARE, J. H. 1984. The prediction of mineral solubilities in natural waters: The Na-K-Mg-Ca-H-Cl-SO₄-OH-HCO₃-CO₃-CO₂-H₂O system to high ionic strengths at 25°C. *Geochim. Cosmochim. Acta*, Vol. 48, 723-751.

HERM, M., GAONA, X., RABUNG, T., FELLHAUER, D., CREPIN, C., DARDENNE, K., ALTMAIER, M., AND GECKEIS, H. 2015. Solubility and spectroscopic study of An^{III}/Ln^{III} in dilute to concentrated Na-Mg-Ca-Cl-NO₃ solutions. *Pure Appl. Chem.*, Vol. 87, 487-502.

HUMMEL, W. 2001. Nitrate complexation: A non-issue in PA. *Paul Scherrer Institut*, Report AN-44-01-28.

HUMMEL, W., BERNER, U., CURTI, E., PEARSON, F. J., AND THOENEN, T. 2002. Nagra/PSI Chemical Thermodynamic Data Base 01/01. *Nagra, Wettingen, Switzerland, and Universal Publishers, Parkland, Florida*, Nagra Technical Report NTB 02-16.

HUMMEL, W., ANDEREGG, G., RAO, L., PUIGDOMENECH, I., AND TOCHIYAMA, O. 2005. *Chemical Thermodynamics Vol. 9. Chemical Thermodynamics of Compounds and Complexes of U, Np, Pu, Am, Tc, Se, Ni and Zr with Selected Organic Ligands* (Amsterdam: Elsevier).

ISETTI, G. 1965. Ricerche sulla struttura della Brucite. *Period. Mineral.*, Vol. 34,

327-335.

JCPDS 2001 JCPDS - Powder diffraction files. Powder diffraction files. Joint Committee on Powder Diffraction Standards.

KALMYKOV, S. N. AND CHOPPIN, G. R. 2000. Mixed $\text{Ca}^{2+}/\text{UO}_2^{2+}/\text{CO}_3^{2-}$ complex formation at different ionic strengths. *Radiochim. Acta*, Vol. 88, 603-606.

KALTSOYANNIS, N. AND SCOTT, P. 1999. *The elements* (Oxford: Oxford University Press).

KATZ, J. J., SEABORG, G. T., AND MORSS, L. R. 1986. *The Chemistry of Actinide Elements* (New York: Chapman and Hall).

KERNKRAFTWERK-GÖSGEN 2010. Technik und Betrieb – Technische Hauptdaten. *Kernkraftwerk Gösgen-Däniken AG*.

KICKER, D. C. AND HERRICK, C. G. 2013. Parameter Summary Report for the 2014 Compliance Recertification Application. *Sandia National Laboratories*, WIPP:1.2.5:PA:QA-L:559199.

KIM, J. I. 1986. *Handbook on the Physics and Chemistry of the Actinides* (Amsterdam: Elsevier Science Publishers B. V.).

KIM, J. I. 1993. The Chemical Behavior of Transuranium Elements and Barrier Functions in Natural Aquatic Systems. *Mat. Res. Soc. Symp. Proc.*, Vol. 294, 3-21.

KLEVTSOV, P. V., BEMBEL, V. M., AND GRANKINA, Z. A. 1969. Crystalline Hydroxychlorides, $\text{Ln}(\text{OH})_2\text{Cl}$, of the rare-earth elements of the cerium group. *Zh. Strukt. Khim.*, Vol. 10, 638-644.

KLEVTSOV, P. V., LYSENINA, T. G., AND KHARCHENKO, L. Y. 1973. Hydrothermal synthesis and study of the Hydroxychlorides of rare-earth elements of the yttrium group $\text{Ln}_3\text{Cl}_2\text{O}(\text{OH})_5$ and $\text{Ln}(\text{OH})_2\text{Cl}$. *Zh. Strukt. Khim.*, Vol. 14, 87-91.

KNAUSS, K. G., WOLERY, T. J., AND JACKSON, K. J. 1990. A new approach to measuring pH in brines and other concentrated electrolytes. *Geochim. Cosmochim. Acta*, Vol. 54, 1519-1523.

KÖNNECKE, T., FANGHÄNEL, T., AND KIM, J. I. 1997. Thermodynamics of trivalent actinides in concentrated electrolyte solutions: Modelling of the chloride complexation of Cm(III). *Radiochim. Acta*, Vol. 76, 131-135.

References

- LEE, J.-Y. AND YUN, J.-I. 2013. Formation of ternary $\text{CaUO}_2(\text{CO}_3)_3^{2-}$ and $\text{Ca}_2\text{UO}_2(\text{CO}_3)_3(\text{aq})$ complexes under neutral to weakly alkaline conditions. *Dalton Trans.*, Vol. 42, 9862-9869.
- MAGILL, J., PFENNIG, G., AND GALY, J. 2006. Chart of the Nuclides 7th edition 2006. *JRC-ITU, KIT*, Report EUR 22276 EN.
- MAGNUSSON, A. AND STENSTROEM, K. 2005. Determination of organic and inorganic ^{14}C on ion exchange resins - method description. *Department of Physics, LUNFD6/(NFFR-3097)*.
- MAGNUSSON, A. 2007. ^{14}C Produced by Nuclear Power Reactors - Generation and Characterization of Gaseous, Liquid and Solid Waste. Lund Universiät.
- MAGNUSSON, A., STENSTROEM, K., AND ARONSSON, P. O. 2008. ^{14}C in spent ion-exchange resins and process water from nuclear reactors: A method for quantitative determination of organic and inorganic fractions. *J. Radioanal. Nucl. Ch.*, Vol. 275, 261-273.
- MARCANTONATOS, M. D., DESCHAUX, M., AND VUILLEUMIER, J. J. 1981. Interactions of $\text{Eu}^{3+}(\text{aq})$ ^7F , $^5\text{D}_1$ and $^5\text{D}_0$ levels with nitrate and inner-sphere (EuNO_3^{2+})* exciplex formation. *Chem. Phys. Letters*, Vol. 82, 36-43.
- MCNP 2011. A general Monte Carlo N-Particle Transport Code, Version MCNP-X. LA-UR-11-1502.
- METZ, V., GECKEIS, H., GONZALEZ-ROBLES, E., LOIDA, A., BUBE, C., AND KIENZLER, B. 2012. Radionuclide behaviour in the near-field of a geological repository for spent nuclear fuel. *Radiochim. Acta*, Vol. 100, 699-713.
- METZ, V., GONZALEZ-ROBLES, E., AND KIENZLER, B. 2014. Characterization of UOX fuel segments irradiated in the Gösigen pressurized water reactor, 2nd Annual Workshop Proceedings, 7th EC FP – FIRST-Nuclides.
- MOOG, H. C., BOK, F., MARQUARDT, C. M., AND BRENDLER, V. 2015. Disposal of nuclear waste in host rock formations featuring high-saline solutions – implementation of a thermodynamic reference database (THEREDA). *Appl. Geochem.*, Vol. 55, 72-84.
- MULLICA, D. F., SAPPENFIELD, E. L., AND GROSSIE, D. A. 1986. Crystal Structure of Neodymium and Gadolinium Dihydroxy-nitrate, $\text{Ln}(\text{OH})_2\text{NO}_3$. *J. Solid State Chem.*, Vol. 63, 231-236.

NECK, V., FANGHÄNEL, T., AND KIM, J. I. 1998. Aquatische Chemie und thermodynamische Modellierung von trivalenten Actiniden. *Forschungszentrum Karlsruhe*, Report FZKA 6110.

NECK, V., ALTMAIER, M., RABUNG, T., LÜTZENKIRCHEN, J., AND FANGHÄNEL, T. 2009. Thermodynamics of trivalent actinides and neodymium in NaCl, MgCl₂, and CaCl₂ solutions: Solubility, hydrolysis, and ternary Ca-M(III)-OH complexes. *Pure Appl. Chem.*, Vol. 81, 1555-1568.

NEEB, K. H. 1997. *The radiochemistry of nuclear power plants with light water reactors* (Berlin: de Gruyter).

NICKELS, J. E., FINEMAN, M. A., AND WALLACE, W. E. 1949. X-Ray Diffraction Studies of Sodium Chloride-Sodium Bromide Solid Solutions. *J. Phys. Chem.*, Vol. 53, 625-628.

NUGENT, L. J., BAYBARZ, R. D., AND BARNETT, J. L. 1969. Electron-transfer spectra and 2-3 oxidation potentials of some lanthanide and actinide halides in solution. *J. Chem. Phys.*, Vol. 73, 1177-1178.

PAIVA, A. P. AND MALIK, P. 2004. Recent advances on the chemistry of solvent extraction applied to the reprocessing of spent nuclear fuels and radioactive wastes. *J. Radioanal. Nucl. Chem.*, Vol. 261, 485-496.

PEARSON, R. G. 1963. Hard and soft acids and bases. *J. Am. Chem. Soc.*, Vol. 85, 3533-3539.

PHILIP HILL, R. C. 2011. A Comparison of Hanford and Savannah River Site High-Level Wastes. *Washington River Protection Solutions*, WRPS-49044-FP.

PITZER, K. S. 1991. Ion interaction approach: Theory and data correlation. In *Activity coefficients in electrolyte solutions* (Pitzer KS, Ed.). CRC Press. Boca Raton.

PLYASUNOV, A., FANGHÄNEL, T., AND GRENTHE, I. 1998. Estimation of Pitzer Equation Parameters for Aqueous Complexes. A Case Study for Uranium at 298.15 K and 1 atm. *Acta Chem. Scand.*, Vol. 52, 250-260.

POINSSOT, C. AND GECKEIS, H. 2012. *Radionuclide behaviour in the natural environment: Science, implications and lessons for the nuclear industries* (Oxford (UK): Woodhead Publishing Limited).

RABINOWITSCH, E. AND BELFORD, R. L. 1964. *Spectroscopy and Photophysics of*

References

Uranyl Compounds (Oxford: Pergamon Press).

RABUNG, T., ALTMAIER, M., NECK, V., AND FANGHÄNEL, T. 2008. A TRLFS study of Cm(III) hydroxide complexes in alkaline CaCl₂ solutions. *Radiochim. Acta*, Vol. 96, 551-559.

RAND, M. H., FUGER, J., GRENTHE, I., NECK, V., AND RAI, D. 2008. *Chemical Thermodynamics Vol. 11. Chemical Thermodynamics of Thorium* (Paris: OECD Publications).

RAO, L. AND TIAN, G. 2011. The effect of temperature on the complexation of Cm(III) with nitrate in aqueous solutions. *Dalton Trans.*, Vol. 40, 914-918.

RAVEL, B. AND NEWVILLE, M. 2005. ATHENA and ARTEMIS: data analysis for X-ray absorption spectroscopy using IFEFFIT. *J. Synchrotron Radiat.*, Vol. 12, 537-541.

RODRIGUEZ-CARVAJAL, J. 1990. FULLPROF: A program for Rietveld refinement and pattern matching analysis. *Proceedings of the Satellite meeting on powder diffraction of the XV Congress of the IUCr. Toulouse, France.* p 127.

ROGERS, D. J., TAYLOR, N. J., AND TOOGOOD, G. E. 1983. Tetraaquatriniratoneodymium(III) Dihydrate, [Nd(NO₃)₃(H₂O)₄]•2H₂O. *Acta Cryst.*, Vol. 39, 939-941.

ROSENBERG, Y. O., METZ, V., AND GANOR, J. 2011. Co-precipitation of radium in high ionic strength systems: 1. Thermodynamic properties of Na-Ra-Cl-SO₄-H₂O system - Estimating Pitzer parameters for RaCl₂. *Geochim. Cosmochim. Acta*, Vol. 75, 5389-5402.

ROTHE, J., BUTORIN, S., DARDENNE, K., DENECKE, M. A., KIENZLER, B., LÖBLE, M., METZ, V., SEIBERT, A., STEPERT, M., VITOVA, T., WALTHER, C. AND GECKEIS, H. 2012. The INE-Beamline for actinide science at ANKA. *Rev. Sci. Instrum.*, Vol. 83, 043105.

RUDLING, P., STRASSER, A., AND GARZAROLLI, F. 2007. Welding of Zirconium Alloys. *A.N.T. International*.

SAKURAGI, T., TANABE, H., HIROSE, E., SAKASHITA, A., AND NISHIMURA, T. 2013. Estimation of Carbon 14 Inventory in Hull and End-Piece Wastes from Japanese Commercial Reprocessing Operation. *Proceedings of the ICEM2013. Brussels, Belgium*.

SCATCHARD, G. 1976. *Equilibrium in solutions: Surface and colloid chemistry* (Cambridge, Massachusetts: Harvard University Press).

SCHINDLER, P. W. 1967. Heterogeneous equilibria involving oxides, hydroxides carbonates, and hydroxide carbonates. *Advanc. Chem. Ser.*, Vol. 67, 196-221.

SCHUMANN, D., STOWASSER, T., VOLMERT, B., GÜNTHER-LEOPOLD, I., LINDER, H. P., AND WIELAND, E. 2014. Determination of the ^{14}C Content in Activated Steel Components from a Neutron Spallation Source and a Nuclear Power Plant. *Anal. Chem.*, Vol. 86, 5448-5454.

SIDKY, P. S. 1998. Iodine stress corrosion cracking of Zircaloy reactor cladding: iodine chemistry (a review). *J. Nucl. Mater.*, Vol. 256, 1-17.

SILVA, R. J., BIDOGLIO, G., RAND, M. H., ROBOUCH, P. B., WANNER, H., AND PUIGDOMENECH, I. 1995. *Chemical Thermodynamics Vol. 2, Chemical Thermodynamics of Americium* (Amsterdam: Elsevier, North Holland).

SILVA, R. J. AND NITSCHKE, H. 1995. Actinide environmental chemistry. *Radiochim. Acta*, Vol. 70-1, 377-396.

SINHA, S. P. AND FRESENIUS, Z. 1982. Determination of a Minute Amount of Europium as Anionic Carbonato-Complex by Spectrofluorometry. *Anal. Chem.*, Vol. 313, 238-239.

SKERENCAK, A., PANAK, P. J., HAUSER, W., NECK, V., KLENZE, R., LINDQVIST-REIS, P., AND FANGHÄNEL, T. 2009. TRLFS study on the complexation of Cm(III) with nitrate in the temperature range from 5 to 200 °C. *Radiochim. Acta*, Vol. 97, 385-393.

SMITH, H. D. AND BALDWIN, D. L. 1993. An investigation of thermal release of carbon-14 from PWR Zircaloy spent fuel cladding. *J. Nucl. Mater.*, Vol. 200, 128-137.

SORENSEN, S. AND LINDERSTROM-LANG, K. 1924. On the determination and value of π_0 in electrometric measurements of hydrogen ion concentrations. *Compt. Rend. du Lab.*, Vol. 15, 1-40.

STRATTON, R. W., BOTTA, F., HOFER, R., LEDERGERBER, G., INGOLD, F., OTT, C., REINDL, J., ZWICKY, H. U., BODMER, R., AND SCHLEMMER, F. 1991. A comparative irradiation test of UO_2 sphere-pac and pellet fuel in the Goesgen PWR. *Proceedings of the Int. Topical Meeting on LWR Fuel Performance "Fuel for the 90's"*. Avignon, France.

References

SWANTON, S. W., BASTON, G. M. N., AND SMART, N. S. 2014. Rates of steel corrosion and carbon-14 release from irradiated steels – state of the art review (D2.1). *CArbon-14 Source Term WP2 Deliverable D2.1*, CAST-D2.1.

TAKAHASHI, R., SASOH, M., YAMASHITA, Y., TANABE, H., AND SAKURAGI, T. 2013. Improvement of inventory and leaching rate measurements of C-14 in hull waste and separation of organic compounds for chemical species identification. *Proceedings of the Scientific basis for nuclear waste management XXXVII, Mater. Res. Soc. Symp. Proc. 1665, . Barcelona, Spain.* p 139-148.

TANABE, H., NISHIMURA, T., KANEKO, M., SAKURAGI, T., NASU, Y., AND ASANO, H. 2007. Characterization of hull waste in underground conditions. *Proceedings of the International Workshop on Mobile Fission and Activation Products in Nuclear Waste Disposal L'Hermitage, La Baule, France.*

TANANAIEV, I. G. 1991a. Solid-state transformation of neptunium(V) compounds in basic and carbonate media. *Sov. Radiochem.*, Vol. 33, 216-219.

TANANAIEV, I. G. 1991b. Preparation and characterization of neptunium(V) and americium(V) hydroxide compounds. *Sov. Radiochem.*, Vol. 33, 224-230.

THOENEN, T., HUMMEL, W., BERNER, U., AND CURTI, E. 2014. The PSI/NAGRA Chemical Thermodynamic DataBase 12/07. *Paul Scherrer Institut (PSI), PSI Bericht Nr. 14-04.*

TRUCHE, L., BERGER, G., ALBRECHT, A., AND DOMERGUE, L. 2013. Abiotic nitrate reduction induced by carbon steel and hydrogen: Implications for environmental processes in waste repositories. *Appl. Geochem.*, Vol. 28, 155-163.

VISWANATHAN, R. 2014. Fuel clad chemical interactions in fast reactor MOX fuels. *J. Nucl. Mater.*, Vol. 444, 101-111.

VITORGE, P. AND TRAN-THE, P. 1991. Solubility limits of radionuclides in interstitial water – Americium in cement. Task 3 – Characterisation of radioactive waste forms, Commission of the European Communities, Luxembourg. Report EUR 13664.

WEGEN, D. H., PAPAIOANNOU, D., NASYROW, R., RONDINELLA, V. V., AND GLATZ, J. P. 2012a. Non-Destructive Analysis of a PWR Fuel Segment with a Burn-Up of 50.4 GWd/t_{HM} – Part I: Visual examination and γ scanning. *Proceedings of the 1st Annual Workshop Proceedings of the Collaborative Project Fast/Instant Release of Safety Relevant Radionuclides from Spent Nuclear Fuel. Budapest, Hungary.* KIT Scientific Publishing, KIT SR 7639.

WEGEN, D. H., PAPAIOANNOU, D., NASYROW, R., RONDINELLA, V. V., AND GLATZ, J. P. 2012b. Non-Destructive Analysis of a PWR Fuel Segment with a Burn-Up of 50.4 GWd/t_{HM} – Part II: Defect Determination. *Proceedings of the 1st Annual Workshop Proceedings of the Collaborative Project Fast/Instant Release of Safety Relevant Radionuclides from Spent Nuclear Fuel. Budapest, Hungary.* KIT Scientific Publishing, KIT SR 7639.

WEGEN, D. H., PAPAIOANNOU, D., GREYTER, R., NASYROW, R., RONDINELLA, V. V., AND GLATZ, J. P. 2012c. Preparation of samples for IRF investigations and Post Irradiation examinations from 50.4 GWd/t_{HM} PWR fuel. *Proceedings of the 1st Annual Workshop Proceedings of the Collaborative Project Fast/Instant Release of Safety Relevant Radionuclides from Spent Nuclear Fuel. Budapest, Hungary.* KIT Scientific Publishing, KIT SR 7639.

WEISER, M., RABUNG, T., AND GECKEIS, H. 2011. Influence of organic buffer materials on trivalent metal ion speciation. *Proceedings of the 13th International Conference on the Chemistry and Migration Behaviour of Actinides and Fission Products in the Geosphere, MIGRATION '11. Beijing, China.* p 62-63.

WIMMER, H. AND KIM, J. I. 1992. Laser-induzierte optische Spektroskopie zur Speziation von f-Elementen in natürlichen aquatischen Systemen. *TU München*, Report RCM 00992.

WINSTON, H., MARSH, O. J., SUZUKI, C. K., AND TELK, C. L. 1963. Fluorescence of Europium Thenoyltrifluoroacetate I. Evaluation of laser threshold parameters. *J. Chem. Phys.*, Vol. 39, 267-270.

YAMADA, S., KANO, K., AND OGAWA, T. 1982. Time Discrimination in the Laser Fluorimetry and Ultratrace Determination of Europium(III) and Samarium(III) with 4,4,4-Trifluoro-1-(2-thienyl)-1,3-butanedione. *Anal. Chim. Acta*, Vol. 134.

YAMAGUCHI, T., TANUMA, S., YASUTOMI, I., NAKAYAMA, T., TANABE, H., KATSURAI, K., KAWAMURA, W., MAEDA, K., KITAO, H., AND SAIGUSA, M. 1999. A Study on Chemical Forms and Migration Behavior of Radionuclides in Hull Wastes. *Proceedings of the 7th International Conference on Environmental Remediation and Radioactive Waste Management - ICEM 1999. Nagoya, Japan.*

ZEHNDER, R. A., CLARK, D. L., SCOTT, B. L., DONOHOE, R. J., PALMER, P. D., RUNDE, W. H., AND HOBART, D. E. 2010. Investigation of the Structural Properties of an Extended Series of Lanthanide Bis-hydroxychlorides Ln(OH)₂Cl (Ln = Nd-Lu, except Pm and Sm). *Inorg. Chem.*, Vol. 49, 4781-4790.